



**HAL**  
open science

# Quantum optics of 1D atoms with application to spin-photon interfaces

Bogdan V Reznichenko

► **To cite this version:**

Bogdan V Reznichenko. Quantum optics of 1D atoms with application to spin-photon interfaces. Quantum Physics [quant-ph]. Communauté Université Grenoble Alpes, 2018. English. NNT: . tel-02128668v1

**HAL Id: tel-02128668**

**<https://hal.science/tel-02128668v1>**

Submitted on 14 May 2019 (v1), last revised 15 Jul 2019 (v2)

**HAL** is a multi-disciplinary open access archive for the deposit and dissemination of scientific research documents, whether they are published or not. The documents may come from teaching and research institutions in France or abroad, or from public or private research centers.

L'archive ouverte pluridisciplinaire **HAL**, est destinée au dépôt et à la diffusion de documents scientifiques de niveau recherche, publiés ou non, émanant des établissements d'enseignement et de recherche français ou étrangers, des laboratoires publics ou privés.

## THÈSE

Pour obtenir le grade de

### **DOCTEUR DE LA COMMUNAUTÉ UNIVERSITÉ GRENOBLE ALPES**

Spécialité : Physique Théorique

Arrêté ministériel : 25 mai 2016

Présentée par

**Bogdan REZNYCHENKO**

Thèse dirigée par **Alexia AUFFEVES**, CNRS

préparée au sein du **Laboratoire Institut Néel**  
dans l'**École Doctorale Physique**

**Optique quantique des atomes  
unidimensionnels, avec application aux  
interfaces spinphoton**

**Quantum optics of 1D atoms with application  
to spin-photon interfaces**

Thèse soutenue publiquement le **13 décembre 2018**,  
devant le jury composé de :

**Monsieur DARIO GERACE**

PROFESSEUR ASSOCIE, UNIVERSITE DE PAVIE - ITALIE, Rapporteur

**Madame VALIA VOLIOTIS**

PROFESSEUR, SORBONNE UNIVERSITES - PARIS, Rapporteur

**Monsieur LOÏC LANCO**

MAITRE DE CONFERENCES, UNIVERSITE PARIS-SACLAY,  
Examineur

**Monsieur SERGEY SKIPETROV**

DIRECTEUR DE RECHERCHE, CNRS DELEGATION ALPES, Président





---

## Abstract

Quantum phenomena give rise to new and revolutionary possibilities in the fields of computation and cryptography. The problems that are unsolvable with classical means are expected to be solved by quantum computers, and communication becomes absolutely secure, if it is encoded in a state of a quantum system. A large effort has been recently paid to research of deterministic transfer of information between photons and atoms, acting as flying and stationary quantum bits respectively. The interaction between these two components is enhanced, if they are put in a unidimensional medium, realizing a so called “1D atom”. The study of this specific optical medium and its applications to quantum technologies constitutes the objective of this thesis.

First, we explore the light-matter interface realized as a 1D atom, with a semiconductor quantum dot in a micropillar cavity as an example. We study the coherent control of this system with light pulses in order to find an optimal way to control its state, varying the power, shape and duration of a pulse and statistics of the state of light field. We also study the impact of the 1D atom on the state of the reflected field as a function of parameters of the experimental device, describing the filtering of single photon Fock state from incident pulse.

We continue with the study of the quantum state of the scattered light field, focusing on its purity. This is required to faithfully transmit the superposition state of one stationary qubit to another using light as a flying quantum bit. We develop a method to experimentally characterize the purity, and apply it to experimental data, showing that the state of art technology allows to create high-purity superpositions.

Finally, we focus on the readout of a stationary qubit based on a single spin in a unidimensional environment. We study how to efficiently use polarized light for this purpose, showing that it is possible to readout the spin state, by detection of only one photon. We explore different deviations from this optimal regime. We also study the decoherence of the spin state due to interaction with the light field and the back-action of the measurement, showing that it is possible to freeze the spin state due to the quantum Zeno effect, which allows the preparation of the qubit, based on it, in an arbitrary superposition state. This opens perspectives towards efficient realization of stationary quantum bits based on single spins embedded in unidimensional electromagnetic environment.

---

## Résumé

Les phénomènes quantiques ouvrent des possibilités nouvelles et révolutionnaires dans les domaines du calcul et de la cryptographie. Il est attendu, que des problèmes impossibles à résoudre avec des moyens classiques, peuvent être résolus par des ordinateurs quantiques, et la communication devient absolument sécurisée si elle est encodée dans un état de système quantique – un bit quantique. Un effort important a récemment été consacré à la recherche sur le transfert déterministe d'information entre photons et atomes, fonctionnant comme des bits quantiques volants et stationnaires respectivement. L'interaction entre ces deux composants est augmentée s'ils sont placés dans un milieu optique unidimensionnel, réalisant un système appelée "un atome 1D". L'étude de ce milieu optique et de ses applications aux technologies quantiques constitue l'objectif de cette thèse.

Tout d'abord, nous explorons l'interface lumière-matière réalisée comme un atome 1D, en prenant une boîte quantique semiconductrice dans un micropilier comme exemple. Nous étudions le contrôle cohérent de ce système avec des impulsions lumineuses afin de trouver un moyen optimal de contrôler son état, en faisant varier la puissance, la forme et la durée d'une impulsion, ainsi que la statistique de l'état quantique du champ lumineux. Nous étudions également l'impact de l'atome 1D sur l'état du champ réfléchi en fonction des paramètres du système expérimental.

Nous poursuivons avec l'étude de l'état quantique du champ lumineux réfléchi, en nous concentrant sur sa pureté. C'est important pour transmettre fidèlement l'état superposition d'un bit stationnaire à un autre par la lumière, qui agit comme un bit quantique volant. Nous développons une méthode de caractérisation expérimentale de la pureté et l'appliquons à des données expérimentales, démontrant ainsi que la technologie moderne permet de créer des superpositions de haute pureté.

Enfin, nous nous concentrons sur la lecture d'un qubit stationnaire basé sur un spin dans un environnement unidimensionnel. Nous étudions comment la lumière polarisée peut être utilisée pour cela, en montrant qu'il est possible de lire l'état de spin en détectant qu'un seul photon. Nous explorons différents écarts de ce régime optimal. Nous étudions également la décohérence de l'état de spin due à l'interaction avec le champ lumineux, et back-action de la mesure, montrant que l'état de spin peut être "gelé". C'est une manifestation de l'effet Zeno quantique, qui permet la préparation du qubit dans un état arbitraire. Cela ouvre des perspectives pour la réalisation efficace de bits quantiques stationnaires basés sur des spins uniques incorporés dans un environnement électromagnétique unidimensionnel.



# Contents

<b>Introduction</b>	<b>9</b>
<b>1 Giant optical nonlinearity in 1D atoms</b>	<b>13</b>
1.1 Introduction . . . . .	13
1.1.1 Single photons as flying qubits . . . . .	13
1.1.2 Unidimensional atom . . . . .	13
1.1.3 Model of a TLS in a cavity . . . . .	14
1.1.4 Steady state giant nonlinearity signatures . . . . .	18
1.1.5 Outline of the chapter . . . . .	20
1.2 Experimental system . . . . .	21
1.2.1 Semiconductor quantum dot . . . . .	21
1.2.2 Modelling of a QD in a cavity . . . . .	22
1.2.3 Characterizing a QD-cavity system . . . . .	24
1.2.4 Cross-polarized detection . . . . .	25
1.2.5 Role of a theoretician . . . . .	26
1.3 Efficient qubit excitation with few photons . . . . .	26
1.3.1 Pulse length and shape . . . . .	29
1.3.2 Influence of photon statistics . . . . .	30
1.4 Controlling light with single atoms . . . . .	32
1.4.1 Giant nonlinearity and reflectivity . . . . .	32
1.4.2 Giant nonlinearity and autocorrelation function . . . . .	34
1.4.3 Temporal profile of the reflected light . . . . .	35
1.4.4 Proportion of the single Fock state . . . . .	37
1.4.5 Multiphoton components suppression . . . . .	39
1.5 Summary . . . . .	40
<b>2 Characterizing coherent superpositions of photon Fock states</b>	<b>42</b>
2.1 Introduction . . . . .	42
2.1.1 Motivation . . . . .	42
2.1.2 Experimental signatures . . . . .	44
2.2 Analytical study . . . . .	45
2.2.1 Time-independent density matrix of the emitted field . . . . .	45
2.2.2 The numbers of photons in the detectors after the interferometer	46
2.2.3 Distinguishable photons . . . . .	51
2.2.4 The 2-photon correlation functions . . . . .	53

2.2.5	Summary of the section . . . . .	54
2.3	Simulations . . . . .	55
2.3.1	Idealized system . . . . .	55
2.3.2	Fock states occupation probabilities . . . . .	56
2.3.3	Excitation of area below $\pi$ . . . . .	58
2.3.4	The $2\pi$ excitation . . . . .	59
2.4	Summary . . . . .	60
<b>3</b>	<b>Spin-photon interface as a quantum meter</b>	<b>61</b>
3.1	Introduction . . . . .	61
3.1.1	Strong and weak measurements . . . . .	61
3.1.2	Spin-dependent polarization rotation . . . . .	64
3.1.3	System under study . . . . .	65
3.1.4	Outline of the chapter . . . . .	67
3.2	Bloch equations for the spin . . . . .	67
3.2.1	Model of the system . . . . .	67
3.2.2	Dynamics of the populations . . . . .	69
3.2.3	Coherences between different spin states . . . . .	69
3.2.4	Behaviour in the magnetic field . . . . .	72
3.3	Light polarization as a quantum meter . . . . .	74
3.3.1	Semi-classical model . . . . .	74
3.3.2	Quantum meter . . . . .	75
3.3.3	Influence of the parameters . . . . .	76
3.4	Quantum trajectories . . . . .	80
3.4.1	Quantum Jumps . . . . .	82
3.4.2	Quantum state diffusion . . . . .	86
3.5	The measurement imperfections . . . . .	88
3.5.1	Imperfect photodetectors . . . . .	88
3.5.2	Non-optimal measurement basis . . . . .	91
3.5.3	Partially distinguishable polarization states . . . . .	93
3.6	Summary . . . . .	95
<b>4</b>	<b>Conclusions and perspectives</b>	<b>96</b>





# Introduction

## Quantum bits and networks

Since the beginning of the XXth century our understanding of the fundamental principles of nature has drastically changed. The discovery of energy quantization by Planck [1, 2] and the reconsidering of the nature of both light and matter by Einstein and de Broglie [3, 4] together with the introduction of the uncertainty principle by Heisenberg [5] gave rise to new breakthroughs in science and affected technological progress. However, the XXth century science mostly used quantum mechanics to understand quantum systems, without ability to efficiently control them. The science of the new millennium is more and more advanced in creation of quantum systems and controlling their properties and states, leading to the so called second quantum revolution [6].

These advancements influence not only the academic research, but the information science and industry, creating a whole new field of quantum information, that opens new possibilities, unaccessible to the classical technologies - so called quantum supremacy or quantum advantage [7]. The birth of this new field started with a suggestion, that behaviour of quantum systems can be simulated with a device, processing information according to the laws of quantum mechanics [8, 9]. Thus, it is possible to simulate a complex and uncontrollable quantum system, constructing a simpler and controllable one [10]. Manipulation of information stored on quantum states led to development of new architecture of computers, based on quantum state superpositions, that can potentially outperform the classical ones [11]. Quantum communication, focused on transmitting information encoded on quantum states [12] opens new possibilities for information exchange, the most famous examples being the cryptographic protocols, unconditionally safe from intruders [13]. Quantum metrology allows to reach beyond the classical limits of precision using the quantum coherence [14].

Classical information is encoded in bits, the fundamental units that can be in a one of the two states, labelled as '0' and '1'. Quantum information uses such fundamental property of quantum systems, as a coherent superposition: any quantum state is a linear combination of other quantum states. This leads to the ability of physical systems to be in such a "combined" state. Therefore, if a set of two quantum states acts as classical '0' and '1', a quantum bit, or a qubit, can be in a coherent superposition of these states.

Realization of quantum technologies requires organizing qubits into a quantum

network [15]. It has to contain two types of qubits: one for storing information (stationary qubits) and another - for transmitting it (flying qubits). In order to successfully implement quantum algorithms, such a network must satisfy the criteria, formulated by David di Vincenzo in [16].

## 1D atom as a unit of a quantum network

Such a network can be realized in different physical systems. There are already promising results with trapped ions [17] and superconducting circuits [18], where the number of qubits in a network exceeds 20, and photonic systems with the number of entangled photons close to 10 [19]. As different physical implementations of the qubits may perform better for some tasks than others, the quantum network based on hybrid systems may have better overall performance [20].

One of the most promising system to act as a flying qubit is a photon. However, it weakly interacts with environment, which is an advantage if its propagation is considered, but poses a problem for an interaction with an emitter. On the other hand, in order to provide the optimal interaction with another qubits, the radiation of the emitter should be in a well-defined spectral and spatial mode.

To achieve high coupling, one can couple a photon and an emitter in a unidimensional environment. This type of system is called a one-dimensional atom (1D atom), as it was first realized with a natural atom in a directional cavity [21, 22]. Nowadays the emitter can be not only a natural atom [23], but a many-atom system, such as a molecule [24], a Josephson junction [25, 26], an impurity in diamond [27] or a semiconductor quantum dot [28]. The one-dimensional medium can be realized as a cavity [29–32] or a single-mode wave guide [33, 34] or evanescently coupled fibres [35].

## Quantum dot in a cavity

One of the examples of an artificial atom, that can be used as an emitter in the 1D atom, is a semiconductor quantum dot (QD), which presents a semiconducting material embedded in another semiconducting material. The confinement provides quantization of energy levels [36]. The transition between the ground and the first excited state has different energy than the transition between the first and the second excited states: this allows to treat the QD as a two-level system, working with only the former of these transitions.

One of the di Vincenzo criteria demands, that the system performing as a stationary quantum bit, had decoherence times, much longer than the gate operation time [16]. An example of such a system is a single spin in a QD, that has coherence time, exceeding all the other characteristic times by several orders of magnitude [37]. Thus, this system presents a perfect candidate to perform as a unit of quantum memory, or a stationary quantum bit.

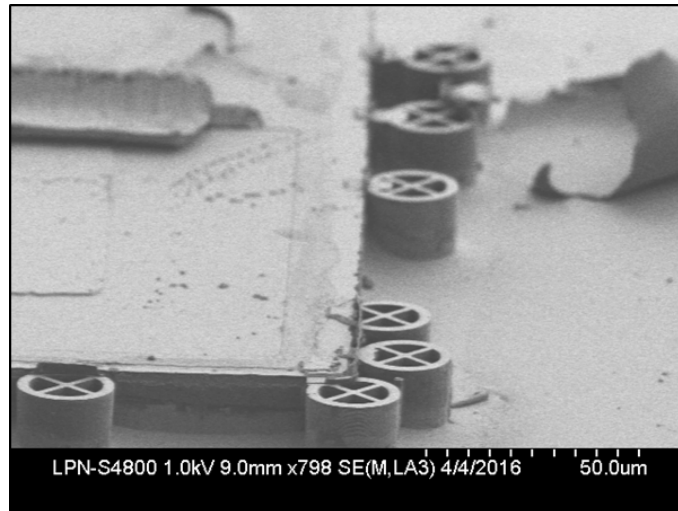


Figure 1: Experimental platform. Scanning Electron Microscope image of deterministically coupled quantum dot-micropillar samples, connected to an electrode. Picture from the Optic of Semiconductor nanoStructures Group of the Centre for Nanoscience and Nanotechnology (Marcoussis, France).

This thesis was performed in a close collaboration with the Optic of Semiconductor nanoStructures Group of the Centre for Nanoscience and Nanotechnology in Marcoussis. They are working with devices consisting of a QD embedded in a micropillar cavity, presenting a Bragg mirror: a sequence of layers with different refractive index. These devices are fabricated with in-situ optical lithography technique, developed in this group [38]. The picture of an example of such a device is presented in Fig. 1.

## Outline of the thesis

This thesis presents a theoretical study of 1D atoms as perspective quantum bits.

Chapter 1 is focused on the interaction between light and emitter in a 1D atom. We revisit the idea of 1D atom, introducing the mathematical model for its description and briefly presenting the experimental system used as a realization of a 1D atom. Afterwards we explore the properties of the incident light field that provide an efficient excitation of the emitter in 1D atom, thus opening ways for coherent control of its state. We study the impact of the duration of the pulse and the quantum state of the incident light on the efficiency of the excitation. Then we explore the impact of the parameters of the system on the state of the incident light, showing that it is possible to filter the single photon state out of the classical light field.

In Chapter 2 we more closely study the state of the light scattered by the emitter. The purity of the state presents our main interest in this chapter, as it is required to transfer information between quantum bits. We analyse the cases when the emitted light presents superpositions and mixtures of Fock states with up to 2 photons, and present a set-up allowing to estimate the purity of the emitted state by studying the interference pattern. We compare this results with experimental data, and show

that the state-of-art technology is capable of preparing high-purity superpositions of Fock states.

In Chapter 3 we focus on the readout of a state of a 1D atom based on a single spin in a wave guide. We briefly revisit the measurement theory and its application to the system under study. Then the average dynamics of the spin is studied with particular attention to the impact of the interaction with light, that acts as a measurement apparatus. We show that it leads to a decoherence in the spin orientation basis, which allows to freeze the dynamics of the spin in an external magnetic field. We then turn to study of the Faraday polarization rotation as a tool to measure the state of the spin. In what follows we study single trajectories of the 1D atom, showing that one photon can be enough to measure the state of the spin, and that the Zeno effect can be observed in this system independently of the incident light power. We conclude with exploration of the deviations from the ideal measurement conditions.

# Chapter 1

## Giant optical nonlinearity in 1D atoms

### 1.1 Introduction

#### 1.1.1 Single photons as flying qubits

Single photons are perfect carriers of information, because their interaction with an environment is very low. But the very same property makes it harder to create optical gates, that are based on the two-photon coalescence [39, 40]. The linear optical gates are probabilistic, which is an intrinsic limitation. Non-linearity of the interaction between a single atom and a single photon can be used to achieve deterministic performance of such operations [41].

Since a long time it has been a challenge to implement non-linear effects at the level of a single photon, so that one can influence the propagation of another one [42]. The best results are achieved in the presence of a medium with non-linear optical effects [43–45], leading to the implementation of deterministic gates. A two-level system (TLS) is a perfect example of such a medium: after it absorbs one photon, it does not interact with the second one.

#### 1.1.2 Unidimensional atom

The light-matter interface is a natural base for a quantum network, with single photons as flying qubits and stationary qubits based on natural atoms [46, 47] or ions [48] or many-atom “artificial atoms” such as semiconductor quantum dots [49, 50] and defects in diamonds [51].

In free space light-matter interaction is inefficient [52]. The emitted light is isotropic, i.e. evenly distributed between random directions in space. To enhance interaction between a single atom and a single mode of electromagnetic field, they are coupled in a one-dimensional (1D) environment. The first realization was performed by Kimble with a Cesium atom, coupled to a leaky directional cavity, and was called one-dimensional atom (1D atom) [21, 22].

In modern realizations, the 1D atoms can be based not only on natural atoms [23],

but also on systems consisting of multiple atoms, either natural, such as molecules [24], or artificial, including semiconductor quantum dots (QD) and Josephson junctions [25, 26]. The 1D environment can be a single-sided leaky cavity [29–32] or a single-mode photonic wave guide [33, 34] or fibres evanescently coupled to directional cavity modes [35].

Another significant difference brought by modification of the environment is that when put into an electromagnetic environment, the emitter changes its radiative properties. It was first suggested by Purcell [53], that the microwave resonator enhances the spontaneous emission from nuclear magnetic transitions. The possibility of the inhibition of the spontaneous emission was noted by Kleppner [54]. Both effects were observed experimentally in the 80s [55, 56], laying the foundation of Cavity Quantum Electrodynamics.

The experiments, studied in this chapter, were implemented by the group of Pascale Senellart in C2N, with QDs in micropillar cavities, and are presented in references [28, 40].

### 1.1.3 Model of a TLS in a cavity

Let us build a simple model of a 1D atom implemented as an emitter in a cavity. The total Hamiltonian of the system under study consists of the Hamiltonian of the TLS  $H_{TLS}$ , the single mode cavity Hamiltonian  $H_c$  and their interaction  $H_{int}$ :

$$H_s = H_c + H_{TLS} + H_{int} \quad (1.1)$$

The cavity is monomode, with the energy  $\hbar\omega_c$  and photon annihilation operator  $a$ , its hermitian conjugate being the creation operator  $a^\dagger$ , giving the total photon number operator as  $a^\dagger a$ . The energy of the photons in the cavity, including the vacuum energy  $\hbar\omega_c/2$ , writes

$$H_c = \hbar\omega_c \left( a^\dagger a + \frac{1}{2} \right) \quad (1.2)$$

Let us consider the energy of vacuum as a reference point, and count the energy difference from this level:

$$H_c = \hbar\omega_c a^\dagger a \quad (1.3)$$

The eigenstates of this Hamiltonian are Fock states  $|n\rangle$ ,  $n$  being a non-negative integer. They denote the number of photons in a cavity.

The TLS has ground and excited energy levels  $|g\rangle$  and  $|e\rangle$ , the energy difference between them being  $\hbar\omega_{TLS}$ . Taking the energy of the ground state as reference, the Hamiltonian writes

$$H_{TLS} = \hbar\omega_{TLS} |e\rangle\langle e| \quad (1.4)$$

where the operator  $|e\rangle\langle e|$  describes the population of the excited level. This term can be represented with ladder operators  $\sigma = |g\rangle\langle e|$  and  $\sigma^\dagger$  that describe the relaxation and the excitation of the TLS respectively:

$$H_{TLS} = \hbar\omega_{TLS} \sigma^\dagger \sigma \quad (1.5)$$

The interaction term is given by the electric dipole interaction between the emitter and the electric field:  $H_i = -\mathbf{D} \cdot \mathbf{E}$ , where  $\mathbf{E} \sim (a^\dagger - a)$  is the electric field operator, and  $\mathbf{D} = (\mathbf{d}\sigma + \mathbf{d}^*\sigma^\dagger)$  is the dipole operator of the emitter, with the dipole moment  $\mathbf{d}$  defined by electron position operator  $\mathbf{r}$  as  $\mathbf{d} = e\langle g|\mathbf{r}|e\rangle$ .

Assuming that the TLS is fixed at maximum of the cavity field, we can write the interaction Hamiltonian as

$$H_{int} = i\hbar g (\sigma^\dagger a - a^\dagger \sigma) \quad (1.6)$$

where we introduced the coupling constant  $g \sim |\mathbf{d}|$  and used the Rotating Wave Approximation [57], valid for  $g \ll \omega_{TLS} \approx \omega_c$ . The two terms describe exchange of quanta between the TLS and the field.

The total Hamiltonian described with this components corresponds to Jaynes-Cummings model. Its eigenvalues are

$$E_0 = 0 \quad (1.7a)$$

$$E_{\pm,n} = n\omega_c + \frac{\omega_{TLS} - \omega_c}{2} \pm \sqrt{ng^2 + (\omega_{TLS} - \omega_c)^2} \quad (1.7b)$$

where  $n$  is the number of photons in the cavity, and such spectrum is called the Jaynes-Cumming ladder.

Let us consider a single photon in a cavity. As the dissipative processes were not introduced, the energy is conserved in the TLS-cavity system, and the state is oscillating between  $|g, 1\rangle$  and  $|e, 0\rangle$ :

$$|\psi(t)\rangle = \frac{1}{2} e^{i\frac{(E_+ + E_-)t}{2\hbar}} \left[ \cos\left(\frac{(E_+ - E_-)t}{2\hbar}\right) |e, 0\rangle + \sin\left(\frac{(E_+ - E_-)t}{2\hbar}\right) |g, 1\rangle \right] \quad (1.8)$$

This process is known as vacuum Rabi oscillation.

### Incoherent processes

The behaviour described by Jaynes-Cumming model is unitary. Real implementations of TLSs and cavities are subject to incoherent interactions with environment. There are three dissipative processes that we are considering here:

- the spontaneous emission from the TLS out of the cavity mode with rate  $\gamma$ ,
- the dephasing of the TLS with rate  $\gamma^*$ ,
- the loss of the cavity photons with rate  $\kappa$ .

The state of the system in presence of dissipative processes can't be represented by a pure state vector, and is described by a density matrix  $\rho$ . Its evolution is ruled by the Lindblad equation [57, 58]:

$$\dot{\rho} = \mathcal{L}[\rho] = -\frac{i}{\hbar} [\hat{H}_s, \rho] + D_{\gamma,\sigma}[\rho] + D_{\gamma^*,\sigma^\dagger\sigma}[\rho] + D_{\kappa,a}[\rho] \quad (1.9)$$



where the dissipation is introduced via operators

$$D_{\alpha,X}[\rho] = \alpha \left( X\rho X^\dagger - \frac{1}{2}(X^\dagger X\rho + \rho X^\dagger X) \right).$$

Let us also introduce the evolution operator  $U(t, t_0)$ , such that  $\rho = \rho(t) = U(t, t_0)\rho(t_0)U^\dagger(t, t_0)$  is a solution to the Eq. (1.9).

Depending on the coupling strength, we can separate the regimes of strong and weak coupling.

- Strong coupling regime  $g > \kappa, \gamma, \gamma^*$ . The evolution of the cavity and TLS populations is described by damped oscillations. The spectrum is described by two distinct peaks at the eigenenergies. The coherent energy exchange between the TLS and the cavity dominates over dissipative processes, and a photon emitted by the TLS into the cavity, can be re-absorbed back rather than being emitted into the environment.
- Weak coupling regime  $g < \kappa, \gamma, \gamma^*$ . The dynamics is described by exponential damping. The spectrum corresponds to the emission at TLS energy, the width of the peak being enhanced due to the Purcell effect, as explained in the next part.

In the following we are considering only the weak coupling regime.

### Purcell effect

In the weak coupling regime  $\kappa \ll g$  the Hamiltonian  $H_{int}$  can be simplified. As cavity decay has much faster rate than all the TLS-related processes, we can consider that it happens at an instant, and thus, at any time  $\dot{a} = 0$ .

For the sake of simplicity let us consider that the pure dephasing is negligible  $\gamma^* = 0$  and that the TLS and the cavity are in resonance  $\omega_c = \omega_{TLS}$ . The Hamiltonian in a frame, rotating at this frequency writes

$$H_{int} = i\hbar g (\sigma^\dagger a - a^\dagger \sigma) \quad (1.10)$$

Let us also introduce  $\sigma_z = [\sigma^\dagger, \sigma]$ .

Let us for the moment switch to the Heisenberg picture, where any arbitrary observable is time-dependent  $A(t)$ . The evolution of an expectation value in both pictures is the same:  $\text{Tr}[\dot{\rho}(t)A] = \text{Tr}[\rho\dot{A}(t)]$ . We multiply Eq. (1.9) by  $A$ , and using the cyclic property of the trace<sup>1</sup> we find the evolution of the system operators under the Hamiltonian (1.10):

$$\dot{a} = -\frac{\kappa}{2}a - g\sigma \quad (1.11a)$$

$$\dot{\sigma} = -\frac{\gamma}{2}\sigma - ga\sigma_z \quad (1.11b)$$

$$\dot{\sigma}_z = -\gamma(\sigma_z + 1) + 2g(\sigma^\dagger a + a^\dagger \sigma) \quad (1.11c)$$

---

<sup>1</sup>Here we reasonably assume that there can be only finite number of photons in the cavity, and we can truncate the Hilbert space we are working in, so that it has finite number of dimensions.

Here we omit the time dependence of the operators for brevity.

In the weak coupling regime  $\kappa \ll g$ , we can disregard the dynamics of the cavity modes. Following Section 13 of [59] we get:

$$a = -\frac{2g\sigma}{\kappa} \quad (1.12a)$$

$$\dot{\sigma} = -\frac{\gamma + \Gamma}{2}\sigma \quad (1.12b)$$

$$\dot{\sigma}_z = -(\gamma + \Gamma)(\sigma_z + 1) \quad (1.12c)$$

where we introduced the Purcell enhanced spontaneous emission rate  $\Gamma = \frac{4g^2}{\kappa}$ . Under this condition we can introduce the new Hamiltonian  $H'$  writing

$$H' = 0 \quad (1.13)$$

and the dissipation operator  $D_{\gamma+\Gamma,\sigma}[\rho]$ , that are equivalent to the Hamiltonian (1.10) and the dissipation operator  $D_{\gamma,\sigma}[\rho]$ . Thus, in the weak coupling regime the cavity enhances the spontaneous emission rate of the emitter, the phenomenon known as the Purcell effect.

Finally, we introduce the Purcell factor  $F_P = \Gamma/\gamma$  to describe the impact of the Purcell effect for a given system. Looking at the equations (1.12) we can see that the total decay rate of the TLS's excited state is  $T_1^{-1} = \Gamma + \gamma$ . For high Purcell factor  $F_P \rightarrow \infty$ , the decay rate of the emitted is defined mostly by emission into the cavity, and the emission into free space, that can be considered as losses, is negligible.

The above-described model is valid in the presence of the pure dephasing as well, which can be introduced by adding the dissipation operator  $D_{\gamma^*,\sigma_z}[\rho]$ . In the experimental set-up with a high Purcell factor one can achieve that the dephasing rate becomes negligible as well  $\Gamma \gg \gamma^*$ .

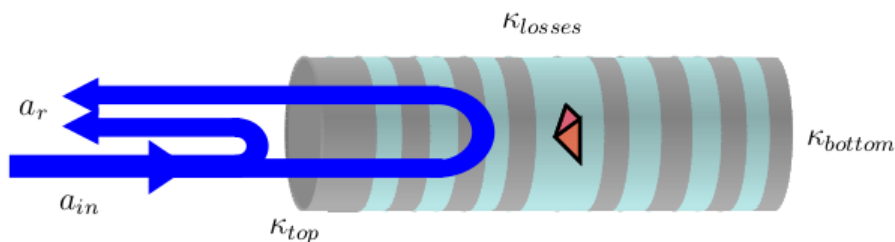


Figure 1.1: Micropillar cavity with relaxation rates from and interference between the light, reflected by the micropillar cavity, and re-emitted by the TLS. Figure reproduced from [60].

Embedding a TLS into a cavity that ensures strong Purcell effect allows to grant that the TLS interacts mostly with the cavity optical mode, being thus isolated from other dissipative processes. Moreover, the cavity can be designed as a 1D environment, ensuring the interaction with modes on its input and output. To

quantify this property, the total cavity relaxation rate can be divided into three contributions:

$$\kappa = \kappa_{top} + \kappa_{bottom} + \kappa_{losses},$$

describing the emission through the top mirror of the cavity, the bottom one and through the side walls respectively, as shown in Fig. 1.1. As in the following we deal with the interaction with the cavity only through the top mirror, we define the output coupling efficiency as

$$\eta = \frac{\kappa_{top}}{\kappa} \quad (1.14)$$

Another important quantity is the directionality  $\beta$ , that quantifies the amount of the photons, emitted into the cavity mode.

$$\beta = \frac{\Gamma}{\Gamma + \gamma} = \frac{F_p}{F_p + 1} \quad (1.15)$$

This quantity can be generalized to include pure dephasing and detuning [61]. High output coupling efficiency and directionality allow to collect all the photons emitted from the cavity as well as to efficiently excite the cavity mode.

### Incident and scattered light

The incident light interacts with the light in the cavity, coherently exchanging photons. We assume that it is in the coherent state, representing laser light. If the cavity is excited through the top mirror, the pump is represented by the additional term in the Hamiltonian, that in the Rotating Wave Approximation writes [28]:

$$H_p = i\hbar(\Omega^* e^{-i\omega_l t} a - \Omega e^{i\omega_l t} a^\dagger) \quad (1.16)$$

where  $\omega_l$  is laser frequency, and the Rabi frequency reads  $\Omega = \sqrt{\kappa\eta}a_{in}$ , where  $a_{in}$  is a complex number representing the incident field amplitude. If a pulsed laser is used to excite the cavity, the incident field amplitude is time-dependent  $a_{in} = a_{in}(t)$ .

The properties of the fields, reflected from and transmitted through the cavity are calculated within the input-output formalism [58]:

$$a_r = a_{in}\mathbb{1} + \sqrt{\kappa\eta}a \quad (1.17a)$$

$$a_t = \sqrt{\kappa(1-\eta)}a \quad (1.17b)$$

The operator of the reflected light includes the interference with the incident light, as illustrated in Fig. 1.1.

#### 1.1.4 Steady state giant nonlinearity signatures

A TLS can absorb or emit only a single photon at a time. Thus it presents a strongly nonlinear medium: being saturated by only one photon, it drastically changes the response to a second photon, an effect known as the giant optical nonlinearity [62]. Under a continuous-wave excitation the saturation is achieved for a laser power of

one incident photon per lifetime [62] and manifests itself in a change between highly transmissive to highly reflective regimes with change of the laser power.

For the case of continuous-wave excitation by a laser, emitting photons at average rate of  $\langle \dot{n} \rangle$ , the incident field amplitude is  $a_{in} = \sqrt{\langle \dot{n} \rangle} = \text{const}$ , and the reflectivity and transmittance write

$$R_{CW} = \frac{\text{Tr} [\rho_{ss} a_r^\dagger a_r]}{\langle \dot{n} \rangle} \quad (1.18a)$$

$$T_{CW} = \frac{\text{Tr} [\rho_{ss} a_t^\dagger a_t]}{\langle \dot{n} \rangle} \quad (1.18b)$$

where  $\rho_{ss} = \rho(t \rightarrow \infty)$  denotes a steady state solution, of Eq. (1.9), or, more simply,

$$\mathcal{L}[\rho_{ss}] = 0.$$

The solutions are shown in Figs. 1.2 and 1.3, where we assume that  $\kappa_{loss} = 0$ , hence  $R + T = 1$ , and that the cavity and the TLS are in resonance  $\omega_{TLS} = \omega_c = \omega$ .

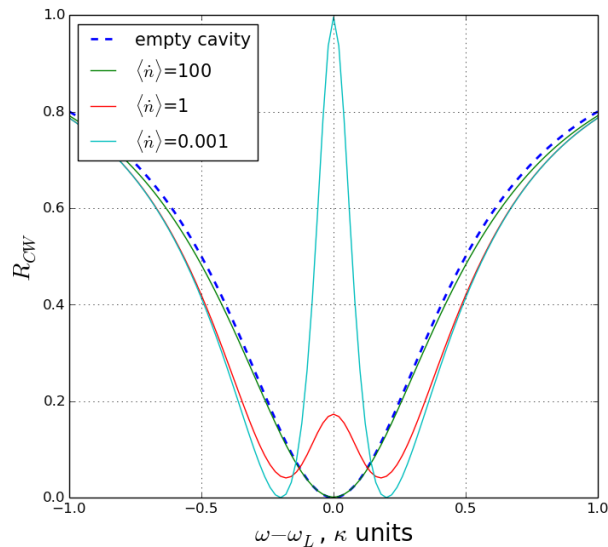


Figure 1.2: Simulated reflectivity of the TLS in a cavity as a function of laser frequency.  $\kappa = 5g$ ,  $\Gamma = 0.8g$ ,  $\eta = 0.5$ , photon intensities are given in  $g$  units.

Fig. 1.2 shows the spectrum of the reflected light for an empty cavity (dashed lines) and a TLS in a cavity (solid lines). For the empty cavity the light, that entered and was reflected from the bottom mirror, destructively interferes with light, that was reflected from a top mirror creating a dip of width  $\kappa$ :

$$R_{CW} = \left| 1 - \frac{\eta\kappa}{\kappa/2 + i(\omega - \omega_l)} \right|^2 \quad (1.19)$$

The minimal value of  $R_{CW}$  for an empty cavity is defined by the top and bottom mirror reflectivities:  $R_{CW}(0) = (1 - 2\eta)^2$ .

In a presence of a TLS, for the lowest pump power value, the transition is not saturated, and we can see the emission spectrum as a peak of width  $\Gamma$  in the middle

of the cavity spectrum, that becomes broader and lower if  $\gamma$  is increased:

$$R_{CW} = \left| 1 - \frac{\eta\kappa}{\kappa/2 + i \left( \omega_c - \omega_l + \frac{g^2}{\omega_l - \omega_{TLS} + i\gamma/2} \right)} \right|^2 \quad (1.20)$$

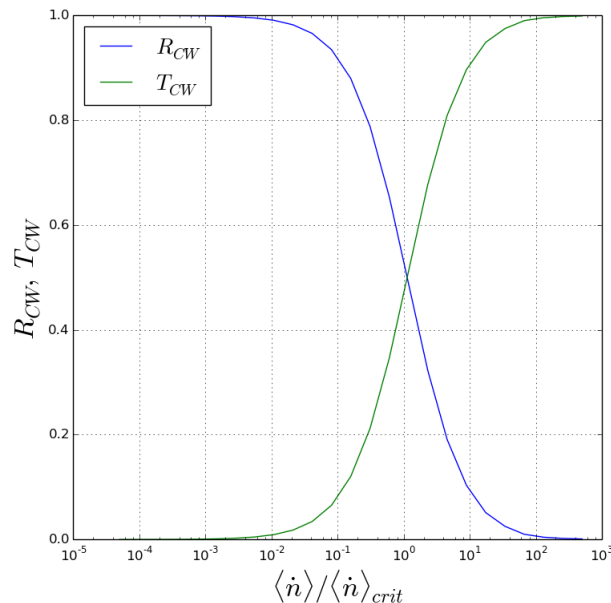


Figure 1.3: Simulated reflectivity of the TLS in a cavity at resonance as a function of laser intensity.  $\kappa = 5g$ ,  $\Gamma = 0.8g$ ,  $\eta = 0.5$ ,  $\langle \dot{n} \rangle_{crit} = \Gamma/4$ .

With the increase of the incident power, the TLS transition becomes saturated. As some photons do not interact with the TLS, the spectrum becomes similar to the empty cavity spectrum. Fig. 1.3 shows the power dependence of the reflectivity and transmittance of the TLS in the cavity at resonance, demonstrating the giant non-linearity (GNL) of the TLS saturation: the saturation happens at values of the incident power of order of one photon per lifetime. The intensity of light reflected from the TLS remains the same with increase of power after the saturation value, but its fraction in incident light becomes negligible.

### 1.1.5 Outline of the chapter

The chapter is organized as follows. In the Section 1.2 we describe the experimental system, consisting of the QD and the micropillar, and we develop a mathematical model to describe its behaviour. In the Section 1.3 we explore the ways to control the 1D atom with a coherent excitation containing few photons. We also describe experiments to characterize a QD-cavity device with the parameters of the model, and a method to detect the excitation of the QD. In the Section 1.4 we study the impact of the 1D atom on the state of statistics of the scattered light. And the brief conclusions are given in the Section 1.5.

## 1.2 Experimental system

### 1.2.1 Semiconductor quantum dot

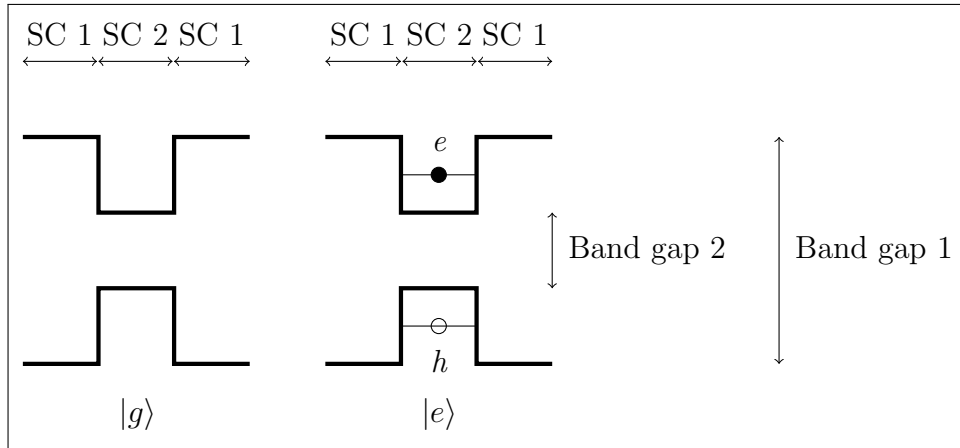


Figure 1.4: Scheme of the levels of a QD: the ground state  $|g\rangle$  corresponds to the full valence band and empty conduction band; the excited state  $|e\rangle$  corresponds to one electron moved from the valence band to the conduction band, thus creating an electron-hole pair.

A semiconductor quantum dot is a system, where electrons and holes are confined in three dimensions. Due to this property, the energy levels are discretized [36], that makes QD similar to a natural atom. The first experimental realizations were obtained in the 80s [63].

A sketch of a QD energy structure is shown at Fig. 1.4, where only one spacial direction is considered - along the horizontal axis, and the vertical axis shows the band separation. At the sketch the semiconductor SC 2 is embedded in another semiconductor SC 1, with different band gap. The left picture shows the ground state  $|g\rangle$ , when all the electrons are in the valence band. On the right one can see the first excited state  $|e\rangle$ , where an electron is moved to the conduction band, and a hole appeared in the valence band. Due to the limited space in all the three dimensions, both the electron and the hole can occupy only certain energy levels [36]. This transition can be caused by non-zero temperature or by an optical excitation, which can be either non-resonant or resonant. Resonance happens if the frequency of the electromagnetic oscillations of the incident light coincides with the difference between the energies of the  $|e\rangle$  and  $|g\rangle$  states  $\omega_q$ , that depends both on the discrete levels of the valence and conduction bands and on the Coulomb interaction between the electron and the hole [60]. In this thesis we shall call the electron-hole the exciton, which is not entirely correct, as they are held together not only by the Coulomb interaction, but mostly by the QD potential.

The excited state  $|e\rangle$  is unstable: due to the interaction with the electromagnetic environment, the electron returns to the valence band and recombines with the hole. A photon is emitted, with an energy, that corresponds to the energy difference

between the  $|e\rangle$  and  $|g\rangle$  states of the exciton  $\omega_q$  [64]. On average it happens at rate  $\gamma$ , similar to the spontaneous emission rate for atoms.

An exciton has also a finite coherence time, that is defined not only by the decay of the excited state  $\gamma$ , but includes the pure dephasing  $\gamma^*$ . It is caused by interaction with the environment that leads to the loss of the information about the phase of the quantum state. The two main identified sources of the pure dephasing are phonons, that vanish for the temperatures approaching to 0 K, and the fluctuations of charge carriers distribution and of nuclear spins of the semiconductor [65].

The exciton state consists of an electron with spin projection on the quantization axis  $S_e = \pm 1/2$  and a heavy hole with  $S_h = \pm 3/2$ . Therefore, there are four possible exciton states:

$$\begin{aligned} | + 2 \rangle &= | + 3/2, +1/2 \rangle \\ | + 1 \rangle &= | + 3/2, -1/2 \rangle \\ | - 1 \rangle &= | - 3/2, +1/2 \rangle \\ | - 2 \rangle &= | - 3/2, -1/2 \rangle \end{aligned}$$

The ground state  $|g\rangle$  has zero spin, and the photons can have  $S_l = \pm 1$  helicity. Thus, only transitions between  $|g\rangle$  and  $|\pm 1\rangle$  are allowed due to the conservation of the angular momentum. The degeneracy between  $| + 1 \rangle$  and  $| - 1 \rangle$  states is lifted due to the exchange interaction between electrons and between holes. The new eigenstates of the QD Hamiltonian are [66]

$$\begin{aligned} |X\rangle &= (| + 1 \rangle + | - 1 \rangle) / \sqrt{2}, \\ |Y\rangle &= (| + 1 \rangle - | - 1 \rangle) / \sqrt{2}. \end{aligned}$$

The energy difference between them is called the fine structure splitting. These states are coupled to the ground state  $|g\rangle$  by mutually orthogonal linear polarizations, and addressing one of them is possible by a choice of a pump polarization.

If an additional electron or hole is embedded into the QD, an excited state contains three particles, and is called a trion. We shall consider this case in the Chapter 3 of the thesis.

### 1.2.2 Modelling of a QD in a cavity

As was mentioned above, the exciton level is divided into two levels with different dipole moments, that we call  $|X\rangle$  and  $|Y\rangle$ . Let us present the model of the QD in a cavity adjusted to this case.

The schema of a QD in a cavity is in Fig. 1.5a. The QD is modelled as a three-level system with the ground state  $|G\rangle$  and two excited states  $|X\rangle$  and  $|Y\rangle$  corresponding to two excitonic linear polarizations. The energies of these states are  $\hbar\omega_X$  and  $\hbar\omega_Y = \hbar\omega_X + \hbar\Delta_{FSS}$  respectively, where  $\Delta_{FSS}$  is the fine structure splitting. The free Hamiltonian of the QD is thus

$$\hat{H}_{QD} = \hbar(\omega_X \sigma_X^\dagger \sigma_X + \omega_Y \sigma_Y^\dagger \sigma_Y) \quad (1.21)$$

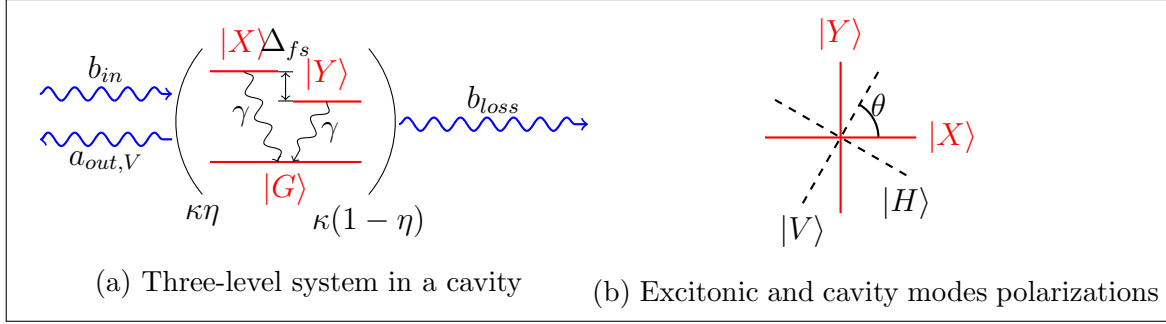


Figure 1.5: Scheme of the levels of a QD in a cavity

where  $\sigma_{X(Y)} = |G\rangle\langle X(Y)|$ .

The cavity is assumed to have 2 modes, that correspond to two linear polarizations,  $H$  and  $V$ . Because of the natural asymmetry of the cavity, they do not necessarily coincide with the dipole axes of the QD, and the angle between the  $X$  dipole of the QD and the  $H$  axis of the cavity is labelled  $\theta$ , as in Fig. 1.5b. The free Hamiltonian of the cavity modes writes

$$\hat{H}_c = \hbar(\omega_V a_V^\dagger a_V + \omega_H a_H^\dagger a_H) \quad (1.22)$$

where  $a_{H(V)}$  are the operators of annihilation of photons with energy  $\hbar\omega_{H(V)}$  in the corresponding modes.

The excitonic levels can be expressed in a basis, parallel to the  $H$  and  $V$  modes as

$$\begin{aligned} |V\rangle &= \cos(\theta)|X\rangle + \sin(\theta)|Y\rangle \\ |H\rangle &= -\sin(\theta)|X\rangle + \cos(\theta)|Y\rangle \end{aligned}$$

the Hamiltonian being

$$\hat{H}_{QD} = \hbar(\omega_V^{at} \sigma_V^\dagger \sigma_V + \omega_H^{at} \sigma_H^\dagger \sigma_H) + \Delta_{FSS} \cos(\theta) \sin(\theta) (\sigma_H^\dagger \sigma_V + \sigma_V^\dagger \sigma_H) \quad (1.23)$$

where  $\sigma_{H(V)} = |G\rangle\langle H(V)|$  and the frequencies are  $\omega_V^{at} = \omega_X \cos^2(\theta) + \omega_Y \sin^2(\theta)$  and  $\omega_H^{at} = \omega_X \sin^2(\theta) + \omega_Y \cos^2(\theta)$ .

The coupling between the QD and the field in the cavity is modelled with the Jaynes-Cummings Hamiltonian

$$\hat{H}_{int} = i\hbar g (a_V^\dagger \sigma_V + a_H^\dagger \sigma_H - \sigma_V^\dagger a_V - \sigma_H^\dagger a_H) \quad (1.24)$$

where  $g$  is the coupling strength.

Due to interaction with electromagnetic environment each exciton relaxes towards the ground state with the rate  $\gamma$ . The cavity modes are coupled to a continuum of modes outside, inducing a decay with rate  $\kappa$ .

The cavity is also pumped with a  $V$ -polarized laser at frequency  $\omega_l$ , represented by the classical field with a Rabi frequency  $\Omega(t)$ , that gives rise to the pump Hamiltonian

$$\hat{H}_p = i\hbar(\Omega^*(t)e^{-i\omega_l t} a_V - \Omega(t)e^{i\omega_l t} a_V^\dagger) \quad (1.25)$$



The Rabi frequency reads  $\Omega(t) = \sqrt{\kappa\eta}a_{in}$  and  $a_{in} = \sqrt{\langle n \rangle}\xi(t)$ , where  $\langle n \rangle$  is the number of incident photons and the temporal profile of the pulse  $\xi(t)$  is a normalized Gaussian function

$$\xi(t) = \left( \frac{8 \ln(2)}{\pi \tau_p^2} \right)^{1/4} \exp(-t^2/\tau_p^2 4 \ln(2)) \quad (1.26)$$

The full Hamiltonian of the system is thus

$$\hat{H}_s = \hat{H}_{\text{QD}} + \hat{H}_c + \hat{H}_i, \quad (1.27)$$

The Lindblad equation ruling the dynamics of the QD-cavity system with density matrix  $\rho$  writes

$$\dot{\rho} = \mathcal{L}[\rho] = -\frac{i}{\hbar} \left[ \hat{H}_s + \hat{H}_p, \rho \right] + D_{\gamma, \sigma_H}[\rho] + D_{\gamma, \sigma_V}[\rho] + D_{\kappa, a_H}[\rho] + D_{\kappa, a_V}[\rho] \quad (1.28)$$

where the dissipation is introduced via operators  $D_{\alpha, X}[\rho] = \alpha (X\rho X^\dagger - \frac{1}{2}(X^\dagger X\rho + \rho X^\dagger X))$ .

The properties of the reflected fields at the output of the cavity are calculated within the input-output formalism [58]. For the reflected field:

$$a_{out, H} = \sqrt{\kappa\eta}a_H \quad (1.29a)$$

$$a_{out, V} = a_{in} + \sqrt{\kappa\eta}a_V \quad (1.29b)$$

In the weak coupling regime for modelling of the data with high incident photon numbers we use the adiabatic elimination, explained in the Sect. 1.1.3, applying it to the  $V$  mode. The input-output relation in this case writes:

$$a_{out, V} = a_{in}(1 - 2\eta) - \sqrt{\Gamma\eta}\sigma_V \quad (1.30)$$

where  $\Gamma = 4g^2/\kappa$ .

### 1.2.3 Characterizing a QD-cavity system

To extract parameters describing a QD in a cavity within the model described above, an experiment pictured in Fig. 1.6 is performed. The laser of constant power and variable frequency excites the TLS through the top mirror of the cavity, and then reflected light is collected via a 50:50 beam-splitter, as in configuration (A), with the detection in the same polarization as the excitation. Thus a reflectivity spectrum is measured, and the experiment is repeated for different pump powers. The experimental data of a such experiment is shown in Fig. 1.7, with the mean number of photons calculated as  $\langle n \rangle = \frac{P_{in}}{\hbar\omega_l}$ .

When the QD is detuned from the cavity mode by application of an electric bias, the reflectivity of the empty cavity is measured, Fig. 1.7(a). It corresponds to the case of Eq. (1.19). The comparison with the experimental data reveals  $\kappa = (90 \pm 10)\mu\text{eV}$  and  $\eta = 0.64$ .

When the QD is in resonance with the laser and the cavity (Fig. 1.7(b)), we can find all the other parameters:  $\hbar\Delta_{FSS} = 3 \pm 1 \mu\text{eV}$ ,  $\hbar g = 19 \pm 0.2 \mu\text{eV}$ ,  $\hbar\gamma =$

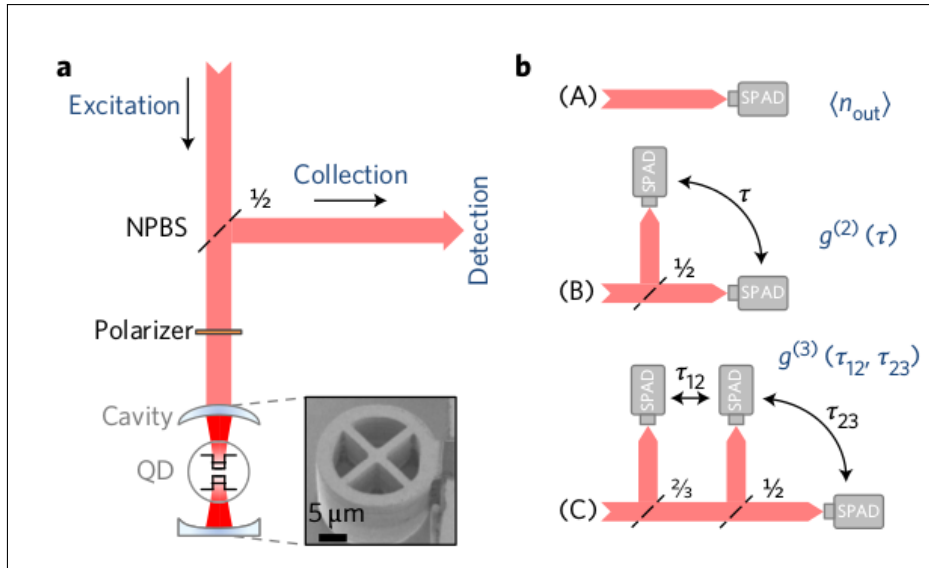


Figure 1.6: Scheme of the experiment. (a) Coherent photon wavepackets are sent to the QD-cavity device. A non-polarizing beam splitter (NPBS) redirects the reflected light. The device is shown in the inset. (b) The reflected light is analysed via one of the three configurations: (A) is used for the reflectivity measurement, (B) and (C) - for the autocorrelation functions of the second and third order respectively.

$0.55 \pm 0.1 \mu\text{eV}$ .  $\theta = 15 \pm 5^\circ$ . As described in the Sect. 1.1.4, for the low values of the pump power (red points) the QD transition is below saturation, and the reflectivity of the light at resonance reaches about  $R_{CW} = 0.9$ . Increase of the power (blue points) saturates the transition, thus lowering the response of the QD and the reflectivity. After the transition is saturated (black points), the reflectivity spectrum is the same as of the empty cavity, with the minimal reflectivity for the resonance frequency.

### 1.2.4 Cross-polarized detection

In a three-level system, to indirectly measure the excited state population one can use the detection in a polarization, orthogonal to the excitation polarization, so called cross-polarized detection.

In our case, we excite along the  $V$  cavity mode. The cavity transfers the excitation to the QD, exciting its  $|V\rangle$  state. The states  $|H\rangle$  and  $|V\rangle$  are not the natural states of the QD, as shown in Fig. 1.5b, and there are oscillations between them at the frequency, proportional to the finite fine structure splitting  $\Delta_{FSS}$ , due to the last term in the Hamiltonian Eq. (1.23). Thus, the state evolves as  $(|X\rangle + e^{i\Delta_{FSS}t/\hbar}|Y\rangle)/\sqrt{2}$  from  $|H\rangle = (|X\rangle + |Y\rangle)/\sqrt{2}$  to  $|V\rangle = (|X\rangle - |Y\rangle)/\sqrt{2}$  during a characteristic time  $\pi\hbar/\Delta_{FSS}$ . This state of the QD can decay, emitting  $H$  polarized photons.

The amount of light emitted in the  $H$  polarization, depends on the relation between the frequency of the  $|H\rangle$ - $|V\rangle$  oscillations, that depends on the fine structure splitting  $\Delta_{FSS}$  and the angle between  $X$  dipole and  $H$  polarization  $\theta$ , and the

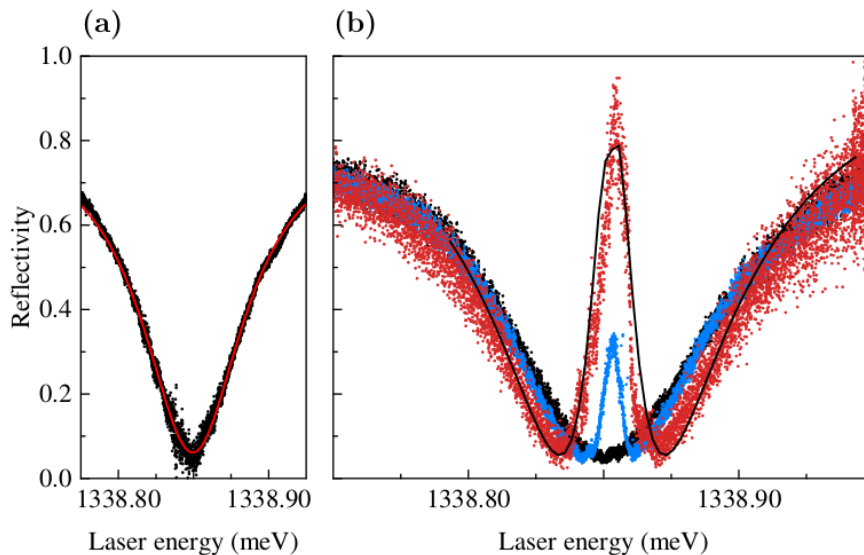


Figure 1.7: Experimental (dots) and simulated (lines) reflectivity of the device as a function of the incident laser energy, reproduced from [67] (a) Reflectivity spectrum of the empty cavity when the QD is detuned. (b) Reflectivity spectrum with the QD at resonance with the laser and the cavity mode, for incident powers of  $P_{in} = 14\text{pW}$  (red points),  $P_{in} = 0.84\text{nW}$  (red points) and  $P_{in} = 2\text{nW}$  (black points). The solid line shows the simulation for the lowest power.

spontaneous emission rate, that for the weak coupling regime is defined as  $\Gamma = 4g^2/\kappa$ . For  $\Delta_{FSS} \sin(2\theta) \ll \Gamma$ , no emission in  $V$  will be observed, as there will be no time for the excitation to be transferred from  $H$  to  $V$  mode.

### 1.2.5 Role of a theoretician

The following sections are based on work done in collaboration with experimentalists in C2N. My role as a theoretician in this work was focused on the modelling of the experiments within a formalism, described here, in order to analyse them and understand underlying physics. My task included characterization of the devices, but due to the possibility to simulate numerically any values of the parameters, we were not limited by characteristics of the devices, and had an ability to compare systems with different characteristics, exploring the impact of each of them. The simulations described in this thesis were performed in QuTiP Python framework [68].

## 1.3 Efficient qubit excitation with few photons

In this chapter we explore different factors that influence the efficient excitation of the QD.

The device used in the experiment that we consider as an example [28] (Fig. 1.8a) is a single QD, inserted into a cavity formed by GaAs/Al<sub>0.9</sub>Ga<sub>0.1</sub>As Bragg mirrors as described in [69]. The geometry of the device allows to tune the QD energy gap to the cavity modes energy by applying a bias.

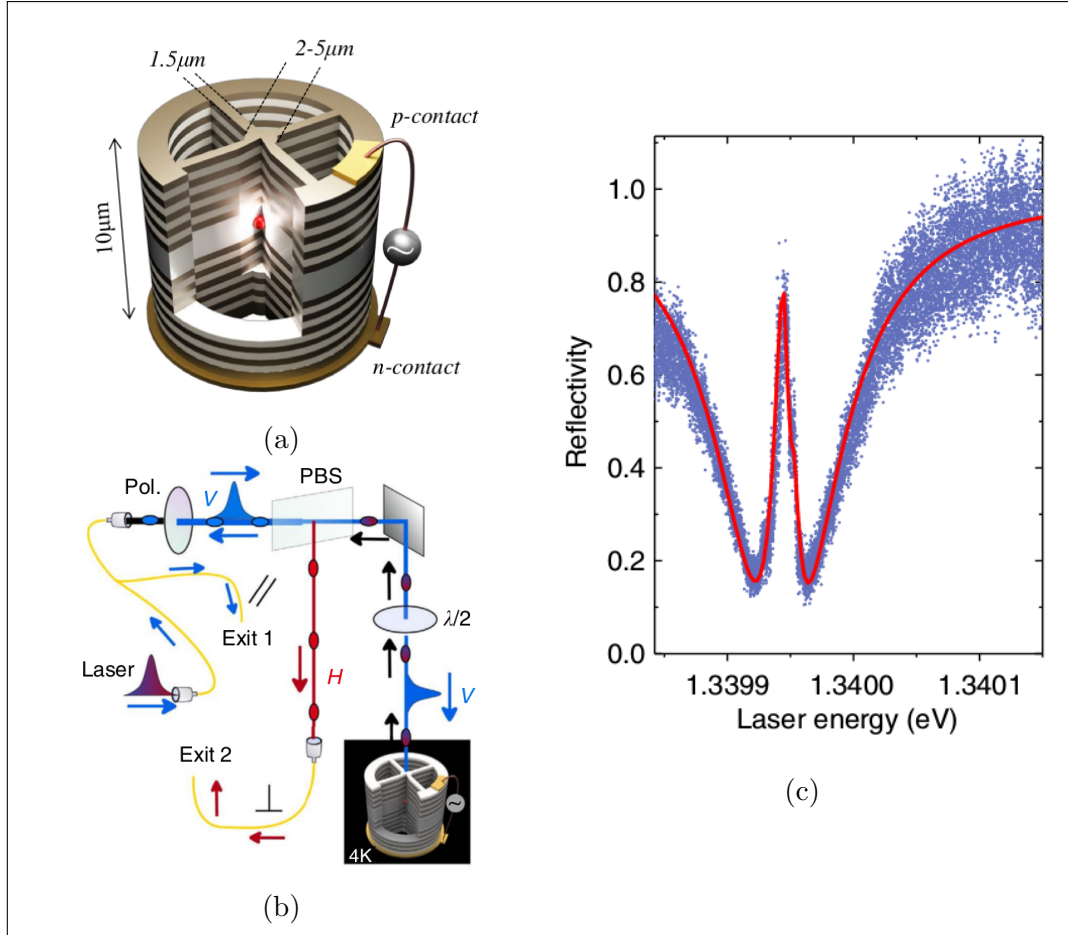


Figure 1.8: (a) The QD-micropillar device. (b) Sketch of the experimental setup. (c) Reflectivity measurement (blue) and simulation (red) for the incident power of approximately 50 pW. Reproduced from [28]. The device is characterized by the following parameters:  $\hbar\delta_V = 0$ ,  $\hbar\delta_H = -70 \mu\text{eV}$ ,  $\delta_X = -\Delta_{FSS}/2$ ,  $\delta_Y = \Delta_{FSS}/2$ ,  $\hbar\Delta_{FSS} = 15 \mu\text{eV}$ ,  $\hbar g = 21 \mu\text{eV}$ ,  $\hbar\kappa = 120 \mu\text{eV}$ ,  $\eta = 0.7$ ,  $\hbar\gamma = 0.3 \mu\text{eV}$ ,  $\theta = \pi/4$ .

To verify that the QD is in one of the excited states the cross-polarized detection scheme is used (Fig. 1.8b): the device is pumped by a pulsed laser that passes through a  $V$  polariser and excites the state  $|V\rangle$  of the QD, and the light emitted by the QD passes through the polarizing beam splitter, separating  $H$  and  $V$  polarizations.

The values of the parameters that describe the experimental device were retrieved from a set of independent experiments of the reflectivity under continuous-wave excitation, as described above. The corresponding curves are plotted in Fig. 1.8c.

Let us now focus on the coherent control of the exciton. When a two-level system is resonantly excited by a coherent field, the excited level population oscillates in time: the effect known as the classical Rabi oscillations. By tuning the excitation pulse so that the maximum population is found in the excited state by the end of the pulse, one can deterministically excite the two-level system: such pulse is called the  $\pi$ -pulse. In the same way it is possible to prepare the system in a given target state, thus performing coherent control. The same method can be applied to the

three-level system that we are considering.

The monitoring of the exciton population is performed, as described above, by cross-polarized detection. When the average power of the pulse is increased, the probability to find the QD in the excited state oscillates as a function of the square root of the incident power. It causes the oscillations in the cross-polarized emission intensity.

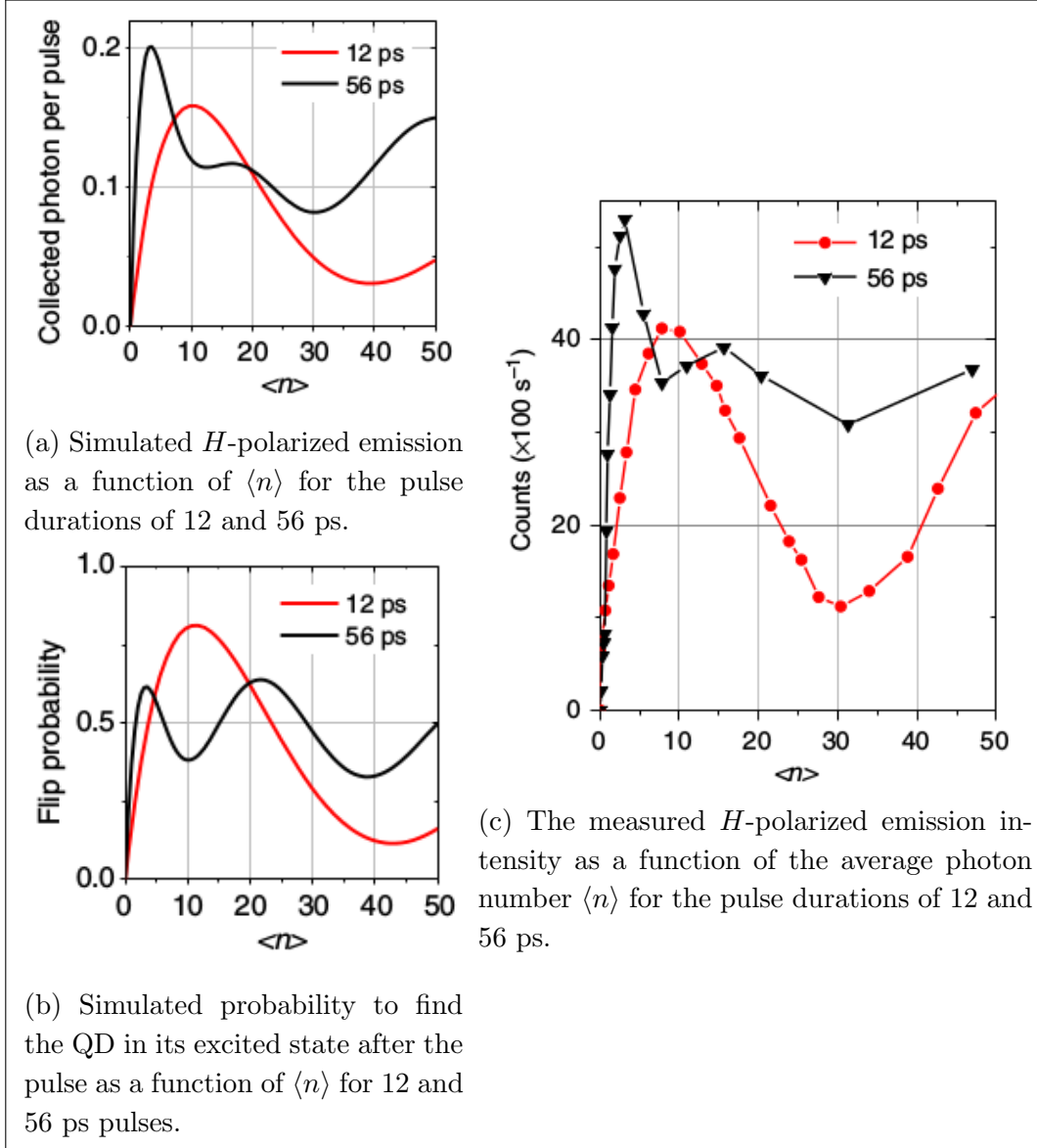


Figure 1.9: Coherent control of a QD excitation. The parameters are the same as in Fig. 1.8.

The simulation of the system with parameters that correspond to the experimental device for the emission intensity and the excitation probability is presented along with the experimental data in Fig. 1.9. The emission into  $H$ -polarized mode is defined as

$$N_H = \kappa\eta \int \text{Tr} \left[ \rho(t) a_H^\dagger a_H \right] dt \quad (1.31)$$

The excited states populations are calculated as

$$P_i(t) = \text{Tr} \left[ \rho(t) \sigma_i^\dagger \sigma_i \right], \quad i = H, V. \quad (1.32)$$

and the flip probability is defined as

$$P_{ex} = \max_t [P_H(t) + P_V(t)] \quad (1.33)$$

Figs. 1.9a and 1.9b present the emission into the  $H$  mode and the flip probability respectively as functions of the mean number of incident photons in the  $V$  polarized field  $\langle n \rangle$  for the two pulse durations. The behaviour of the curves is similar, with maxima and minima for the same pulse duration occurring for the same values of excitation power.

In the Fig 1.9c we present the experimental measurement of  $N_H$ . Both for 56 and 12 ps pulses the Rabi oscillations are clearly visible, with maxima reached for 3.8 and 8.6 photons respectively for each pulse duration.

Having simulated the dynamics of the system, we reproduce the behaviour of the  $N_H$  dependence. This allows us to assume that the excitation probability of the device behaves according to the calculated flip probability. In the next subsections we'll discuss more on this behaviour and dependence on various parameters.

### 1.3.1 Pulse length and shape

The dependence of the excitation probability on the pulse duration is shown in Fig. 1.10: short pulses have lower spectral overlap with the QD in the cavity, and hence are reflected without exciting the  $V$  mode, while for the longer pulses spontaneous emission plays more important role, hence both cases require more incident photons.

The temporal profile of the pulse is important as well. As was shown in [70], the most efficient excitation of a TLS is performed with a rising exponential pulse,  $\xi(t) = \Theta(t - t_0) \frac{1}{\sqrt{\tau_p}} \exp\left(\frac{t-t_0}{2\tau_p}\right)$ , where  $\Theta(t)$  represents the Heaviside step function. The optimal pulse duration in this case is inverted spontaneous emission rate  $\tau_p = (\Gamma + \gamma)^{-1}$ , so that the decay rate is compensated by the pump.

Fig. 1.10 depicts also the dependence of the excitation probability on the fine structure splitting  $\Delta_{FSS}$ . The higher values of this quantity provide faster oscillation between the  $|H\rangle$  and  $|V\rangle$  states of the QD. A three-level system with a value of  $\Delta_{FSS}$  much lower than all the other characteristic times is equivalent to a two-level system, and thus there is only one option for the relaxation of the exciton: into the cavity mode with the same polarization. But in the case of an infinitely high fine structure splitting, the excited state population is instantly distributed evenly over  $|H\rangle$  and  $|V\rangle$  states, both of them recombining with the same rates, which doubles the total relaxation rate of the exciton. In this case more photons needed to maximally excite the QD, and thus curves with higher values of  $\Delta_{FSS}$  correspond to higher values of the mean photon number in the pulse  $\langle n \rangle$  at the  $\pi$ -pulse.

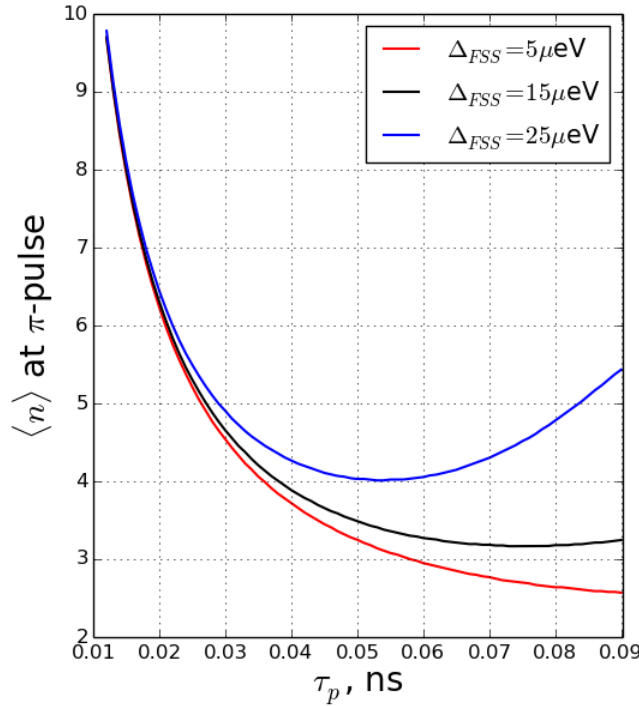


Figure 1.10: The number of incident photons required to maximally excite the QD as a function of pulse duration

### 1.3.2 Influence of photon statistics

The coherent excitation of the QD is harder to achieve with laser light of low mean photon numbers, because such a pulse is a coherent state and still can consist of vacuum with probability of  $P(0) = e^{-\langle n \rangle}$ . That's why the most efficient excitation can be performed with a Fock state, than with a coherent state. In this subsection we compare the excitation by a coherent pulse of  $\langle n \rangle = 1$  and the Fock state, introduced as a wave packet

$$|1_\xi\rangle = \int dt \xi(t) a_V^\dagger |0\rangle \quad (1.34)$$

The master equation (1.28) needs to be generalized for the case of a single photon wave packet, exciting the system [71]. The total Hamiltonian of the system (the QD in a cavity in our case) and the environment (the electromagnetic field) writes

$$H_{tot} = H_s + \int d\omega \hbar\omega b^\dagger(\omega)b(\omega) - ik \int d\omega \left( a_V^\dagger b(\omega) - a_V b^\dagger(\omega) \right) \quad (1.35)$$

where  $k = \sqrt{\kappa/\pi}$  is the coupling strength, and  $b(\omega)$  are the annihilation operators of the field at frequency  $\omega$ . Here we neglected the interaction of the  $H$  polarized cavity field with the environment, as it is not influenced by the way  $V$  mode is excited. The initial state of the system and environment is  $\rho_{tot}(t_0) = \rho(t_0) \otimes |1_\xi\rangle\langle 1_\xi|$ .

In the Heisenberg picture the evolution of any arbitrary system operator  $X(t)$  with initial state  $X(t_0) = X \otimes \mathbb{1}$ , is defined by an equation  $\dot{X}(t) = -\frac{i}{\hbar} [H_{tot}, X(t)]$ ,

that expands as

$$\begin{aligned} \dot{X}(t) = & -\frac{i}{\hbar} [H_s, X(t)] - [X(t), a_V^\dagger(t)] \left( \kappa a_V(t) + \sqrt{2\kappa} b_{in}(t) \right) + \\ & + \left( \kappa a_V^\dagger(t) + \sqrt{2\kappa} b_{in}^\dagger(t) \right) [X(t), a_V(t)] \end{aligned} \quad (1.36)$$

where  $b_{in}(t) = \int d\omega e^{-i\omega(t-t_0)} b(\omega) / \sqrt{2\pi}$ .

The mean value of the operator  $X(t)$  can be found as

$$\langle X(t) \rangle = \text{Tr}_{S+E} [X(t) \rho_{tot}(t_0)] = \text{Tr}_S [X \rho_s(t)] \quad (1.37)$$

where subscript  $S(E)$  under  $\text{Tr}$  means the system's (environment's) degrees of freedom.

Exploiting the identity  $\frac{d}{dt} \langle X(t) \rangle = \text{Tr}_S [X \dot{\rho}_s(t)]$  we retrieve the system of equations for the density matrix from the Bloch Equation (1.36):

$$\begin{aligned} \dot{\rho}_{11} &= \mathcal{L}'[\rho_{11}] + \Omega(t) \left( [\rho_{01}, a_V^\dagger] - [\rho_{01}^\dagger, a_V] \right) \\ \dot{\rho}_{01} &= \mathcal{L}'[\rho_{01}] - \Omega(t) [\rho_{00}, a_V] \\ \dot{\rho}_{00} &= \mathcal{L}'[\rho_{00}], \end{aligned} \quad (1.38)$$

where density matrices  $\rho_{mn}(t)$  are defined as traces over the incident photon numbers

$$\rho_{mn}(t) = \text{Tr}_{\text{ph}} \{ U(t, t_0) \rho_s(t_0) \otimes |m_\xi\rangle \langle n_\xi| U^\dagger(t, t_0) \} \quad (1.39)$$

$U(t, t_0)$  being the evolution operator corresponding to the total Hamiltonian  $H_{tot}$  from a time  $t_0$  prior to the interaction. Hence  $\rho_{11}$  is the density matrix of the system when a single photon is incoming. Initial conditions for these density matrices are  $\rho_{11}(0) = \rho_{00}(0) = \rho_S(0)$ ,  $\rho_{01}(0) = 0$  and  $\mathcal{L}'[\rho]$  is the Liouvillian that excludes the pump term  $\hat{H}_p$ :

$$\mathcal{L}'[\rho] = -\frac{i}{\hbar} [\hat{H}_s, \rho] + D_{\gamma, \sigma_H}[\rho] + D_{\gamma, \sigma_V}[\rho] + D_{\kappa, a_H}[\rho] + D_{\kappa, a_V}[\rho] \quad (1.40)$$

The result of a simulation with the experimental parameters from the previous subsection is presented in Fig. 1.11. The dashed line shows the incident pulse time dependence. The exciton population is shown in solid lines: red for the  $|1\rangle$  Fock state excitation and black for the excitation with a coherent state with  $\langle n \rangle = 1$ .

The most efficient performance of the single-photon Gaussian pulse is excitation of the QD up to 80% population of the excited level [70], that was calculated for the ideal two-level system with the optimal pulse length. As we are modelling the realistic system, that includes losses, this rate is lower: up to 55%. The coherent performs worse, exciting the QD only up to 38%, as it includes only 37% of probability to include a single-photon component, the other 37% being the vacuum, and the rest of the probabilities distributed between multi-photon components that are less efficient in exciting the QD [72]. The difference in interaction of different Fock states with a 1D atom can be exploited to influence various properties of the reflected and transferred fields, as shown in the next section.



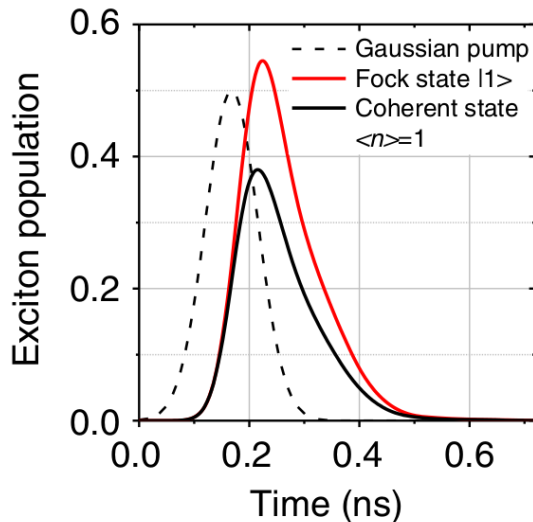


Figure 1.11: Simulated probability to find the QD in its excited state as a function of time for pulse duration of 56 ps. Dashed line: contour of the pulse in arbitrary units. Black: excitation with a coherent pulse of  $\langle n \rangle = 1$ . Red: excitation with a single photon Fock state.

## 1.4 Controlling light with single atoms

The Giant Nonlinearity of the 1D atom provides a perfect medium for two-photon interaction. After absorbing one photon the 1D atom does not interact with the second one. Thus the propagation of one photon is affected by another one: it affects not only reflectivity, changing the direction of the scattered light, but also the statistics of the reflected and transmitted fields, that exhibit anti-bunching and bunching respectively [73].

In this section we consider the pulsed excitation in the  $V$  polarization mode, and collection of the reflected light in the same polarization, as in the scheme of the experiment in Fig 1.6. The experimental system used as an illustration is the same, that was presented in Fig. 1.7.

To be used as a quantum gate, the device must interact with the photons with given temporal profile. In the following, we consider the device probed by the pulsed laser excitations with given pulse duration of  $\tau_p = 125\text{ps}$  and mean number of photons  $\langle n \rangle = \frac{P_{in}}{f\hbar\omega_l}$ , where  $f$  is the repetition rate of the laser.

### 1.4.1 Giant nonlinearity and reflectivity

The reflected photons are collected in the same polarization as the incident ones, and the reflectivity is calculated as

$$R' = \frac{\int \text{Tr} \left[ \rho(t) a_{out,V}^\dagger a_{out,V} \right] dt}{\langle n \rangle} \quad (1.41)$$

and measured as in Fig.1.6, configuration (A).

The dependence of the reflectivity  $R$  on the incident pump power is plotted in Fig. 1.12a with the red dashed line. In general it follows the behaviour, shown in Fig. 1.2 for the continuous-wave excitation: the reflectivity is high for the low-power excitation, and changes its value around  $\langle n \rangle \approx \Gamma\tau_p \approx 3$  to the lower value due to the QD saturation.

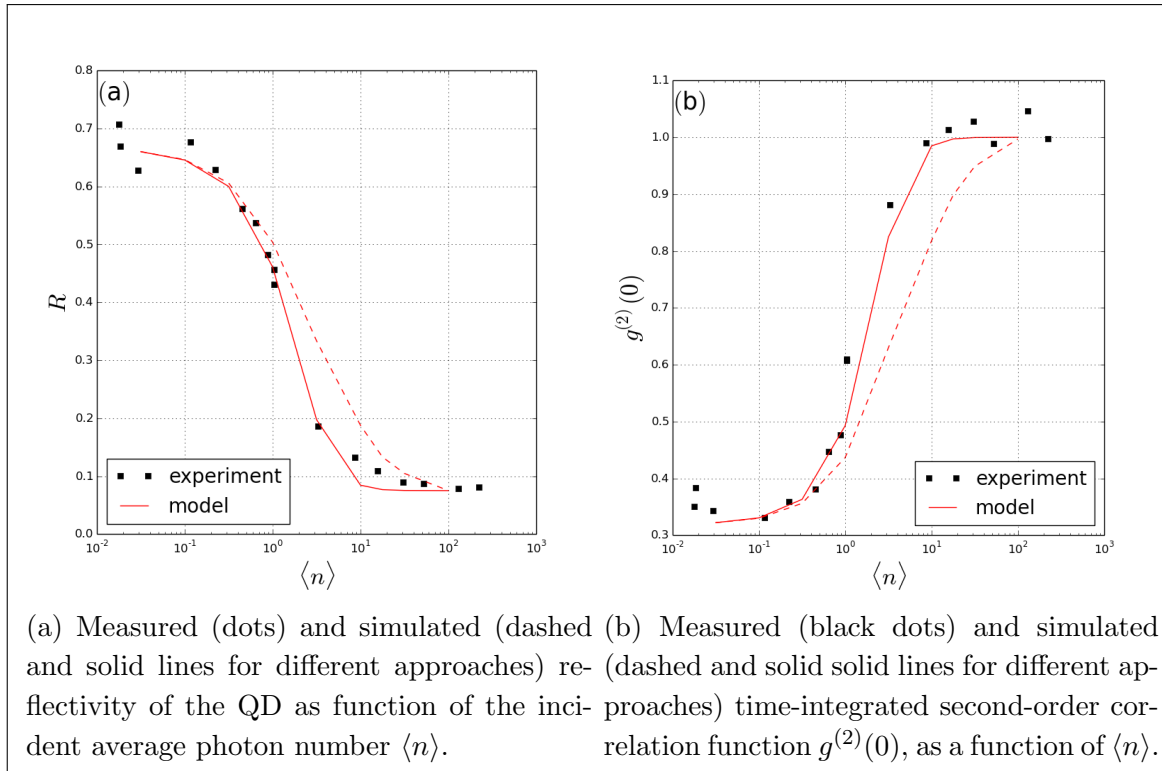


Figure 1.12: Single photon nonlinearity and second-order correlation measurements. The system is characterized by the following set of parameters:  $\kappa = (90 \pm 10)\mu\text{eV}$ ,  $\eta = 0.64 \pm 0.02$ ,  $\hbar\Delta_{FSS} = 3 \pm 1 \mu\text{eV}$ ,  $\hbar g = 19 \pm 0.2 \mu\text{eV}$ ,  $\hbar\gamma = 0.55 \pm 0.1 \mu\text{eV}$ ,  $\theta = 15 \pm 5^\circ$ .

There is a discrepancy between the experimental data, shown with black squares, and the simulated values of  $R$ , obtained with the parameters, extracted from the continuous wave measurements of Fig. 1.7: the transition between the saturated and non-saturated regimes in experimental data is slightly steeper, than predicted by the simulation. There can be several explanations for this phenomenon: the input coupling efficiency of the micropillar is changed during the experiment due to a possible mechanical instability of the set-up, or the incident pulse profile deviates from the Gaussian shape  $\xi(t)$ , used in the simulation, or there is a power-dependent tunnelling of an electron from a QD.

The effect of the first hypothesis can not be as strong as the deviation: the coupling efficiency would need to change its value by more than 50%, to produce such a change. Similarly for the pulse shape: as long as it remains symmetric with respect to the maximal value of the pulse intensity, its effect on the QD excitation remains the same [70], and the pulse used in the set-up was symmetric. The power-dependent tunnelling, however, allows to explain the difference and to reproduce the

experimental data.

The effect describes the case when the electron escapes the QD, that is in excited state, thus shifting the resonance frequency and reducing the interaction of the QD with the light in the cavity. This effect makes the nonlinearity sharper. Probability that the electron is still in the QD as a function of the mean number of photons in the incident pulse is modelled phenomenologically, with only one free parameter:

$$p_X = \frac{1}{1 + (\langle n \rangle / N_0)^2}.$$

From the experimental data we derive  $N_0 = 3$ , and

$$R = R' p_X + R_{min}(1 - p_X) \quad (1.42)$$

where  $R_{min}$  is a reflectivity of an empty cavity. The corrected result is shown in Fig. 1.12a with a red solid line.

## 1.4.2 Giant nonlinearity and autocorrelation function

We expect that for the low incident powers, the light, reflected from a QD, will consist mostly of single photons [73]. The signature of this antibunching would be low values of the second order autocorrelation function  $g^{(2)}(0)$ . To calculate it the following approach was used:

$$g^{(2)'}(0) = \frac{\int dt \int d\tau G^{(2)}(t, t + \tau)}{\left\{ \int \text{Tr} \left[ \rho(t) a_{out,V}^\dagger a_{out,V} \right] dt \right\}^2} \quad (1.43)$$

where

$$G^{(2)}(t_1, t_2) = \langle a_{out,V}^\dagger(t_1) a_{out,V}^\dagger(t_2) a_{out,V}(t_2) a_{out,V}(t_1) \rangle \quad (1.44)$$

The two-time correlations are calculated according to the Quantum regression theorem, e.g.  $\langle a^\dagger(t) a^\dagger(t+\tau) a(t+\tau) a(t) \rangle$  is calculated as an expectation value of  $a^\dagger a$  on the effective density matrix  $\tilde{\rho}(t+\tau) = U(t, t+\tau) \rho(t) a^\dagger U^\dagger(t, t+\tau)$  where  $U(t_1, t_2)$  is an evolution operator and  $\rho(t) = U(t_0, t) \rho(t_0) U^\dagger(t_0, t)$  is the density matrix of the system at time  $t$ , i.e.  $\langle a^\dagger(t) a^\dagger(t+\tau) a(t+\tau) a(t) \rangle = \text{Tr} \left[ (U(t, t+\tau) \rho(t) a^\dagger U^\dagger(t, t+\tau)) a^\dagger a \right]$ . The effect of escaping electron is considered for the autocorrelation function as

$$g^{(2)}(0) = g^{(2)'}(0) p_X + 1(1 - p_X) \quad (1.45)$$

where 1 is used as a value for the light that did not interact with the QD and remained classical.

The measurement of the  $g^{(2)}(0)$  was performed by dividing the reflected light and measuring coincidences between clicks in two detectors, as shown in Fig. 1.6, configuration (B).

The behaviour of the  $g^{(2)}(0)$  function as a function of the number of incident photons  $\langle n \rangle$  is presented in Fig. 1.12b. For the higher incident laser powers the QD

becomes saturated and the photon blockade effect disappears, as most of the light that reaches the detector did not interact with the QD and has the same Poissonian statistics of the initial laser coherent state, that corresponds to  $g^{(2)}(0) = 1$ .

As expected, the values for the low powers  $\langle n \rangle < 1$  include a large fraction of antibunched light:  $g^{(2)}(0) \approx 0.35$ . This is a signature of the photon blockade: after the first photon is absorbed, the transition is saturated and the QD-cavity device acts like an empty cavity, transmitting the rest of the photons and reflecting back the photon that was absorbed.

The autocorrelation function of the reflected light  $g^{(2)}(0)$  is defined by the parameters of the QD, the cavity and the incident light. The high-power value is not influenced, as it is always close to 1, due to the dominance of the classical coherent field. Figure 1.13 shows the dependence on the pulse duration  $\tau_p$ . Very short pulses are spectrally wide, so they are reflected by the cavity, which means that light remains classical, and during too long pulses there will be multiple photon emissions that increases the  $g^{(2)}(0)$ . The parameters that increase the losses from the QD, such as  $\gamma$ ,  $\gamma^*$  and  $\Delta_{FSS}$ , increase  $g^{(2)}(0)$ , as the relative proportion of the single-photon component in the reflected light decreases. The cavity lifetime  $\kappa$  also decreases the  $g^{(2)}(0)$ , as its increase decreases the emission into the cavity mode  $\Gamma = 4g^2/\kappa$ . For the same reason,  $g$  decreases the low-power value of  $g^{(2)}(0)$ , as with stronger coupling, more photons interact with the QD. The change in  $g$  and  $\kappa$  also effects the steepness of the transition between the low-power and high-power regimes.

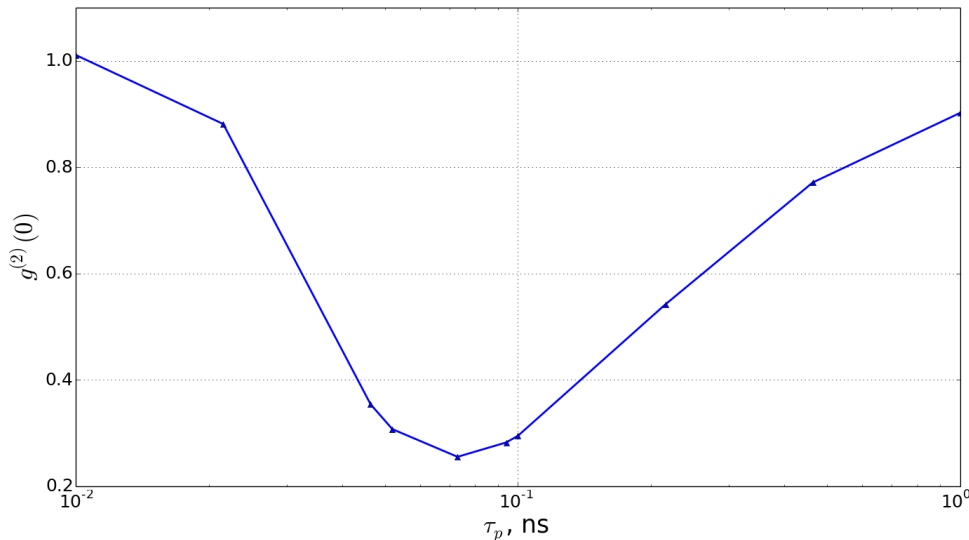


Figure 1.13: Low power  $g^{(2)}(0)$  dependence on  $\tau_p$ . Horizontal axis is in logarithmic scale.

### 1.4.3 Temporal profile of the reflected light

Let us now focus on the temporal profile of the light reflected from the device. The experimental data and the simulation are presented in Fig. 1.14, where the black

line and dots represent the case of an empty cavity, and the red colour signifies the QD on resonance with the cavity. The experiment was performed with a 55 ps pulse. The simulated data was calculated as

$$f \text{Tr} \left[ \rho(t) a_{out,V}^\dagger a_{out,V} \right]$$

where  $f = 0.082$  pulses/ns is the repetition rate.

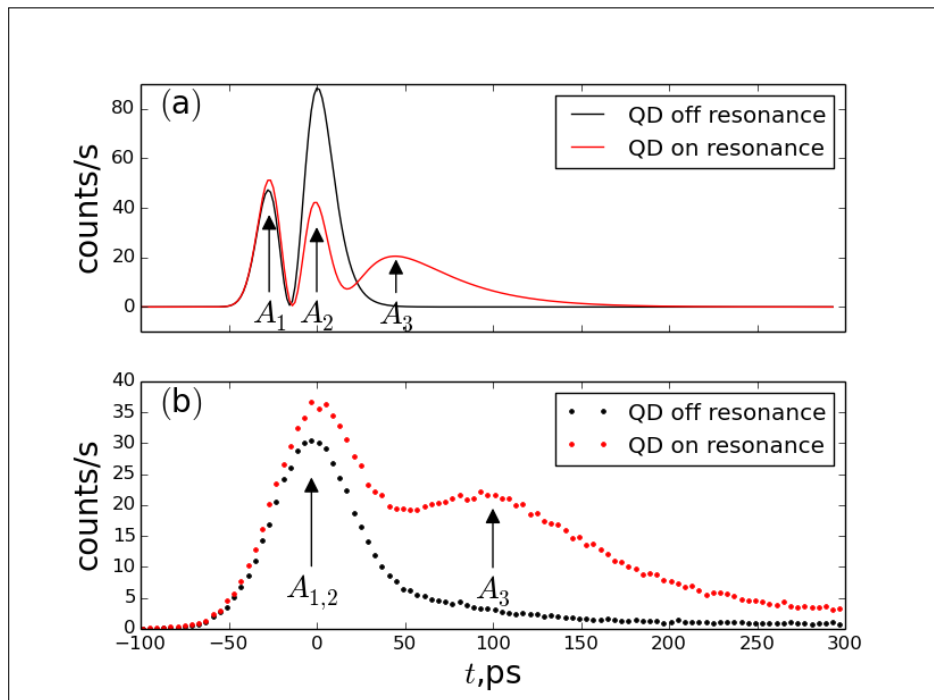


Figure 1.14: Simulated (a) and measured (b) temporal profile of the reflected wavepacket. Black lines and points represent the case of an empty cavity, the red one - the case of the excitation with a QD on resonance. The grey line shows the incident pulse in arbitrary units. The measurement is performed for a system, different from the previously described, and with the laser pulse of 55 ps, while the simulation - for a 20 ps pulse.

The case of the QD being off resonance corresponds to the case of an empty cavity. The temporal profile is composed of two contributions. The first peak  $A_1$  corresponds to the light reflected from the top mirror of the cavity without interacting with it. The second peak  $A_2$  appears because of the light that excited the cavity and was emitted from it, and it exhibits the decay time of the cavity photons. These two contributions can not be distinguished for the experimental data due to the finite temporal resolution of the detectors.

For the case of the QD in the resonance with the cavity, for low excitation power we observe the third peak  $A_3$ , that corresponds to the light absorbed and re-emitted by the QD. Time, needed for the re-emission is called Wigner time delay, and is determined by the light-matter coupling [74]. When the QD is brought in resonance with the cavity, only the intensity of the peak  $A_2$  decreases, as it is the light that entered the cavity, that is partially absorbed by the QD. If the power of the incident

pulse is augmented, the third peak gets saturated, and the first two continue to increase linearly. Eventually the fraction of light that is re-emitted from the QD becomes negligible, and the temporal profile corresponds to the one of the empty cavity.

#### 1.4.4 Proportion of the single Fock state

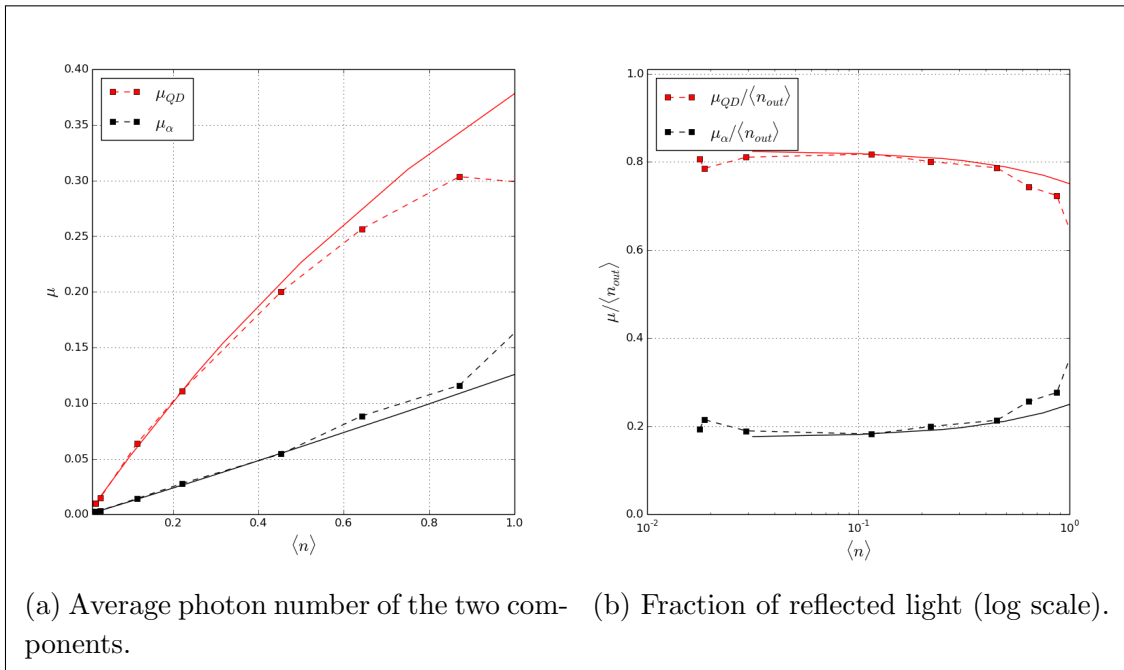


Figure 1.15: Fractions of the coherent and single-photon components in the reflected light as a function of the incident power  $\langle n \rangle$ . Solid lines represent simulation, while the squares - the measured values. Single-photon component is given in red, and coherent light in black.

For the low incident powers we can interpret the antibunching of the reflected field as a signature that the device behaves like a single Fock state filter: the device that transforms a coherent pulse into a pulse that consists of a single photon and vacuum.

The reflected field consists of the laser light, reflected from the cavity, and the light, re-emitted by the QD. However, the coherent interference between these components happens only in the temporal overlap between them, which, as can be seen from Fig. 1.14, is negligible. Thus, the totality of the reflected light can be considered as a mixture of the coherent light reflected by the cavity and the single-photon component, emitted by the QD. This assumption lets us separate light into two components with different statistical properties and find their proportions using the measurements of the autocorrelation function  $g^{(2)}(0)$ .

For this purpose we use the formalism of the probability generating functions [75], which are probability distributions of a discrete random variable  $X$ , expressed as

power series:

$$G(X; s) = \sum_{k=0}^{k=\infty} s^k P(X = k) \quad (1.46)$$

where  $P(X = k)$  is a probability for the random variable  $X$  to be equal to the value  $k$ . It can be shown that the generating function of a distribution of two independent variables is given by a product of two generating functions:

$$G(X, Y; s) = G(X; s)G(Y; s) \quad (1.47)$$

In our case the random variable represents the average number of photons in the reflected field  $\langle n_{out} \rangle$ . It consists of two contributions:  $\mu_{QD}$  which is average the number of photons re-emitted by the QD, and  $\mu_\alpha$ , the average number of photons coming from the laser. This latter field is described by a Poissonian distribution, hence

$$G_\alpha(s) = \sum_{k=0}^{k=\infty} s^k e^{-\mu_\alpha} \frac{\mu_\alpha^k}{k!} = e^{-\mu_\alpha(1-s)} \quad (1.48)$$

The field, emitted from the QD consists only of single photons and vacuum components, so

$$G_{QD}(s) = P(n = 0) + sP(n = 1) = (1 - \mu_{QD}) + s\mu_{QD} \quad (1.49)$$

where we used that  $P(n = 0) + P(n = 1) = 1$  and  $P(n = 1) = \mu_{QD}$ . This assumption is valid only for low incident photon numbers, so we restrict ourselves to  $\langle n \rangle < 1$ .

The generating function of the mixture of the two components is, according to Eq. (1.47):

$$G_{total}(s) = G_{QD}(s)G_\alpha(s) = [(1 - \mu_{QD}) + s\mu_{QD}] e^{-\mu_\alpha(1-s)} \quad (1.50)$$

The equations to find  $\mu_{QD}$  and  $\mu_\alpha$  are obtained from the measured values of the total number of reflected photons and of the autocorrelation function  $g^{(2)}(0)$ , that can be expressed through the second derivative of the total probability generating function [75]:

$$\langle n_{out} \rangle = \mu_{QD} + \mu_\alpha = R\langle n \rangle \quad (1.51a)$$

$$g^{(2)}(0) = \frac{G''_{total}(s)}{\langle n_{out} \rangle^2} = 2\mu_{QD}\mu_\alpha + \mu_\alpha^2 \quad (1.51b)$$

The values of  $\mu_{QD}$  and  $\mu_\alpha$  and their ratio to the total number of reflected photons found from these equations are shown in Fig. 1.15 with red and black colours respectively. The number of photons in the coherent light  $\mu_\alpha$  raises linearly with the incident laser power, while the average number of single photons  $\mu_{QD}$  reaches saturation as  $\langle n \rangle$  approaches the value of 1.

Applying this technique to the data of the [40], we calculate that  $\mu_{QD}/\langle n_{out} \rangle \approx 0.8$  for the incident powers that do not saturate the QD, as is plotted in Fig. 1.15b. It means that quantum light dominates the composition. That high fraction of single photon component in reflected light is a signature that the device acts as single photon Fock state filter.

### 1.4.5 Multiphoton components suppression

Another way to look at the statistics of the reflected field is to directly find the occupation probabilities  $P(k)$  of the reflected light. It can be accessed with measurements of the autocorrelation functions  $g^{(m \leq n)}$ . However, we assume that for the incident powers below saturation all the multiphoton components  $P(k \geq 4)$  are negligible. Thus,  $P(k)$  can be found from the set of equations:

$$\sum_{k=0}^3 P(k) = 1 \quad (1.52a)$$

$$\sum_{k=1}^3 k P(k) = \langle n_{out} \rangle \quad (1.52b)$$

$$\sum_{k=2}^3 k(k-1) P(k) = g^{(2)}(0) \langle n_{out} \rangle^2 \quad (1.52c)$$

$$6P(3) = g^{(3)}(0,0) \langle n_{out} \rangle^3 \quad (1.52d)$$

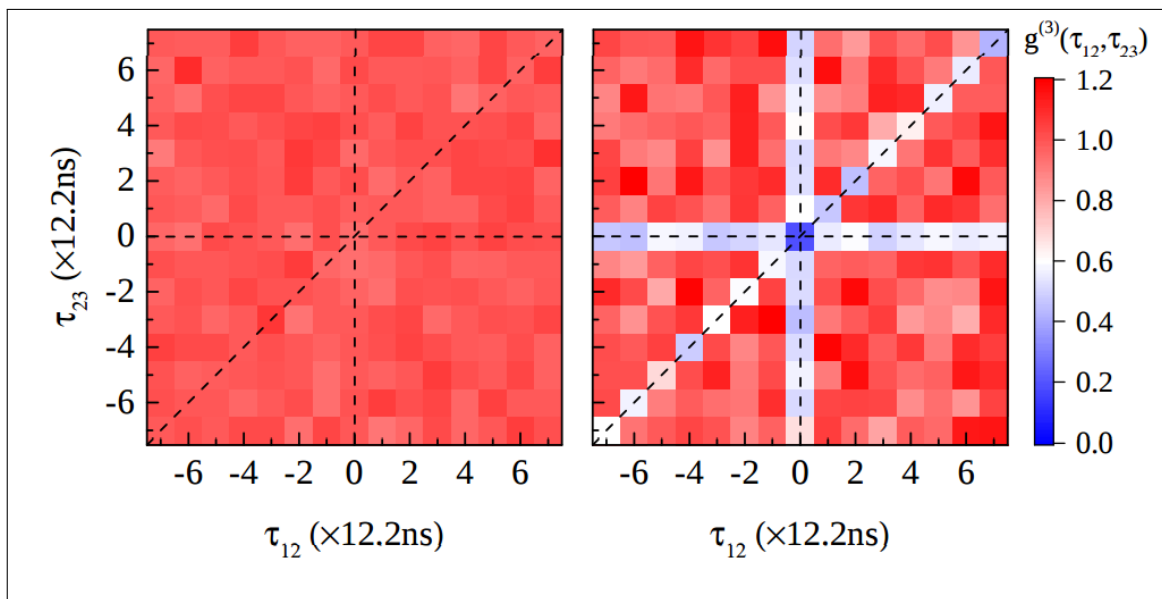


Figure 1.16: Histogram of the  $g^{(3)}(\tau_{12}, \tau_{23})$ , obtained by integration over 5ns over each peak, reproduced from [67] Left panel: incident field. Right panel: reflected field for  $\langle n \rangle = 0.6 \pm 1$

The third-order autocorrelation function  $g^{(3)}(0,0)$  is measured by splitting the reflected light and channelling it into three detectors, see Fig. 1.6, configuration (C). The three-photon coincidences are recorded as functions of two time delays:  $\tau_{12}$  between detectors 1 and 2 and  $\tau_{23}$  between detectors 2 and 3. The resulting plots are given in Fig 1.16 for the incident light (left) and the reflected light for incident light of  $\langle n \rangle = 0.6 \pm 1$ . The central square corresponds to  $g^{(3)}(0,0)$ .

The occupation probability distribution  $P(k)$  for the incident light, the reflected light are presented in Fig. 1.17. The Poissonian distribution for the average output



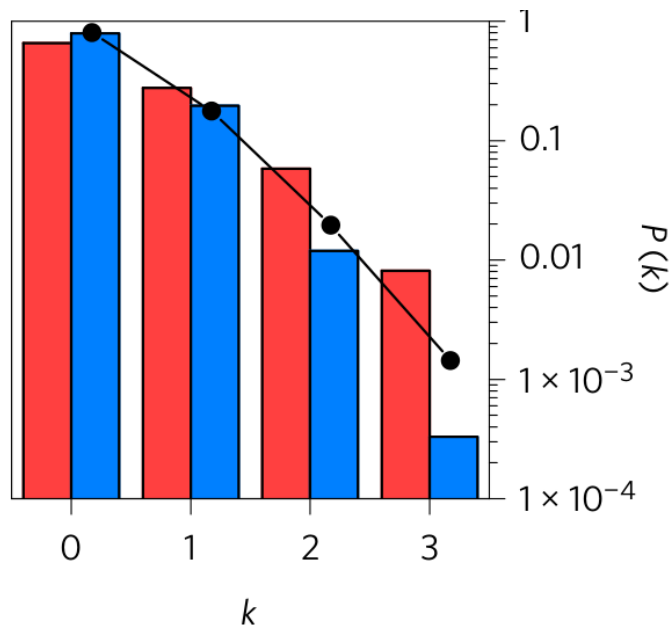


Figure 1.17: Probability distribution  $P(k)$  for the incident field (red) and the reflected field (blue). The black dots show the Poisson distribution for the average output photon number  $\langle n_{out} \rangle$ . Reproduced from [67].

photon number  $\langle n_{out} \rangle$  is shown with black dots for comparison: the measured output field deviated strongly from this distribution. The comparison of the reflected field statistics with the one for the input field shows that the vacuum component is slightly increased:  $P_{out}(0)/P_{in}(0) = 1.2$ . There is a decrease in one photon component  $P_{out}(1)/P_{in}(1) = 0.7$ , that is comparable with the measured  $\eta = 0.64$ : part of the single photons of the input field escaped through the bottom mirror and walls of the micropillar cavity. On the other hand, there is a notable decrease in the multiphoton components:  $P_{out}(2)/P_{in}(2) = 0.2$  and  $P_{out}(3)/P_{in}(3) = 0.04$ .

These results show that the device implements suppression of the multiphoton components, thus filtering single photons and converting incident classical coherent light into a highly non-classical state, consisting mostly of vacuum and single photon Fock states.

## 1.5 Summary

In this chapter we described the non-linear behaviour of a 1D atom, taking a QD in a cavity as an example and exploring effect of the device parameters on the possibility to coherently control it with light pulses, and to verify that the system reaches the excited state by monitoring the polarization, orthogonal to the excitation polarization. The efficiency of the excitation can be controlled by tuning the excitation pulse power, shape, length and statistics. We have also shown that there are modern QD-cavity devices, capable of exhibiting behaviour of ideal 1D atoms. Namely, the high contrast of reflectivity with a low threshold value.

On the other hand, the properties of the scattered light depend on the system.

We show, how its statistics is changed, discussing the influence of the device's parameters and the properties of the excitation pulse. In the next Chapter we continue this study, focusing on the purity of the scattered light state.

An apparatus considered here can perform as a path-encoding gate: in a two-pulse set-up the response of the QD on the second pulse will be drastically changed in a presence of the first pulse. Implementation of such a gate would require access to the transmitted field, that was not the case for the devices used in the chapter. With a similar system, based on a QD, doped with an electron or hole, a deterministic gate can be obtained via realization of polarization encoding [76–78]. We focus on this kind of system in the third Chapter of this thesis.

# Chapter 2

## Characterizing coherent superpositions of photon Fock states

### 2.1 Introduction

#### 2.1.1 Motivation

The most important difference between a classical bit and a quantum one lies in the ability of the latter to be in a superposition state. It is crucial to be able to transfer the state between the qubits: one of the basic requirements for the efficient quantum computation is an ability to faithfully interconvert stationary and flying qubits into each other [16].

If a two-level system (TLS) is used as a stationary qubit, photons may be used to transfer its state. In this case single-photon states are the optimal candidates for the role of quantum bits [15], and the superposition of the ground and excited states of the TLS can be transferred to another TLS by a superposition of the vacuum and the single-photon state of the light field. In the state of art, the single- and N-photon states have been widely studied as possible components of quantum networks [79, 80], gates [39, 81] and computers [41, 82]. But the vacuum component was mostly considered to be a problem rather as a resource, that can be used for encoding quantum information in the photon number basis. The superposition states so far have been obtained by complex engineering of quantum states [83–85].

As was mentioned in the previous chapter, in the state of the art a pulse containing a single photon is not enough to efficiently excite a TLS. On the other hand, it was demonstrated that a TLS is capable of emitting two-photon states [86]. For these reasons, in the following we also include into consideration quantum states with up to two-photon component.

An impressive progress has been recently made in creation of sources of on-demand indistinguishable single photons [31, 69, 87–89]. The fact that the light is in a single-photon Fock state can be demonstrated via the measurement of the autocorrelation function of the emitted light. The measurements of the interference

on a beam-splitter, as in the Hong-Ou-Mandel (HOM) experiment [90], allow to check the indistinguishability of the photons [91–93].

To map the state of one TLS into the state of another one, the emitted light must have high purity, i.e. to be in a coherent superposition, and not in a mixture of the Fock states. For example, if the state of the TLS that we want to transfer, is  $\alpha|e\rangle + \beta|g\rangle$ , it is preferable for the light to be in the state  $\alpha|1\rangle + \beta|0\rangle$  instead of a mixed state  $|\alpha|^2|1\rangle\langle 1| + |\beta|^2|0\rangle\langle 0|$ , that has lost its coherence. That's why, as the next step in emitted light characterization, we would like to find or estimate the purity of the quantum state  $\rho_f$  of emitted light field, that is defined as  $P = \text{Tr} [\rho_f^2]$ .

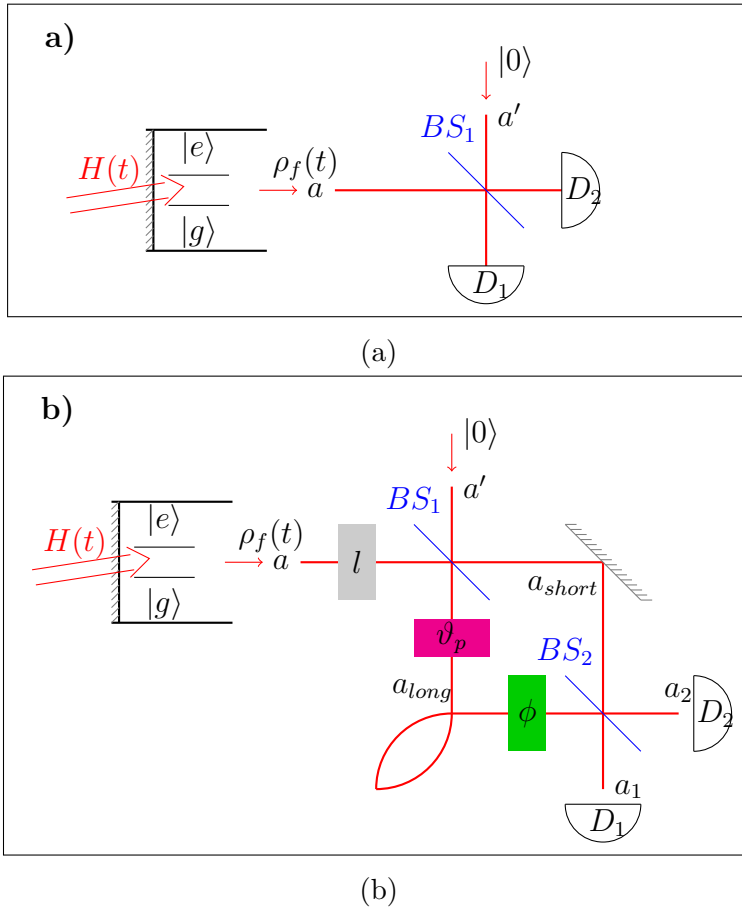


Figure 2.1: Scheme of the TLS with the Mach-Zehnder interferometer. The TLS in a 1d wave guide with a mirror (left part of the Scheme) is coherently excited with a laser pulse. The light emitted in state  $\rho_f(t)$  in mode  $a$  passes from upper left to lower right. The grey rectangle  $l$  represents losses in transmission, the magenta rectangle  $\vartheta_p$  represents rotation of the polarization, and the green one  $\phi$  - the phase shift in one of the branches. The blue lines  $BS_{1,2}$  are the beam-splitters, and the semicircles  $D_{1,2}$  are the detectors.

a) The set-up to measure the autocorrelation function  $G^{(2)}$  and the number of emitted photons  $N_{out}$ .

b) The set-up to measure the autocorrelation function  $G_{HOM}^{(2)}$  and the numbers of photons  $N_{1,2}$ .

### 2.1.2 Experimental signatures

For this purpose we are using an experimental set-up, that is usually exploited to probe the indistinguishability of photons, that is tightly connected to the purity of single-photon states. This set-up is schematically pictured in Fig. 2.1, where the TLS is excited by a pulsed laser. The power and the duration of the pulse are chosen so that the pulse has area  $\theta$  and populates the excited level up to  $P_e = \sin^2(\theta/2)$ . The measured values are:

1. The number of photons, emitted by the TLS  $N_{out}$
2. The second order autocorrelation function of the emitted field  $G^{(2)}$
3. The difference between numbers of photons in two outputs of a beam-splitter in case of an interaction of a pulse of emitted light with itself  $N_1, N_2$
4. The number of the coincidences in the two outputs of the same detectors  $G_{HOM}^{(2)}$ .

The quantities  $N_{out}$  and  $g^{(2)}$  are measured immediately after the emitter, as shown in Fig. 2.1a. The light, emitted from the TLS into the propagating mode  $a$  passes through a beam-splitter. The number of photons, emitted from the TLS during the pulse  $N_{out} = \langle a^\dagger a \rangle$  is measured as a sum of the clicks in two detectors during the pulse. The second order autocorrelation function of the emitted field  $G^{(2)} = \langle a^\dagger a^\dagger a a \rangle$  is measured as a number of coincidence between them. These two quantities allow to calculate the occupations of the Fock states, under the assumption that there are no more than two photons in the emitted light, that is generally valid for short pulses [86].

The quantities  $N_1, N_2$  and  $g_{HOM}^{(2)}$  are measured via the Mach-Zehnder interferometer [94–96], as depicted in Fig. 2.1b. The sequence of pulses is sent to the TLS, the time interval between them being longer than all the characteristic times of the TLS. The scattered light passes through the beam-splitter  $BS_1$ , getting out of it in a superposition of two spatial modes. One of them travels through the short branch of the interferometer and another one through the long branch. The lengths of the two branches is equal to the time between pulses multiplied by the speed of light: the light from the first pulse in the 'long' spatial mode interferes at the beam-splitter  $BS_2$  with the light in the 'short' mode from the second pulse. On the way through the interferometer light may accumulate phase difference  $\phi$  between the photons in the two branches (shown in green), as well as the difference in polarization angles  $\vartheta_p$  (in magenta). Then the numbers of photons in each detector  $N_{1,2} = \langle a_{1,2}^\dagger a_{1,2} \rangle$ , and the number  $G_{HOM}^{(2)} = \langle a_1^\dagger a_2^\dagger a_2 a_1 \rangle$  of coincidences are measured. As we shall see, these quantities give access to the non-diagonal elements of the density matrix of emitted light  $\rho_f$ , thus allowing to quantify the purity of the superposition state.

The chapter is organized as follows. The analytical calculations of the aforementioned observables within a simple 'ad hoc' model of light are presented in the Section 2.2. The simulation of the emission process, and the comparison with experimental data is given in the Section 2.3.

## 2.2 Analytical study

In this section we provide a simple description of the light field in a guide in order to find connection between the state of the field and the measured values of the observables, mentioned in the introduction. We are ignoring the physics of the emission process.

### 2.2.1 Time-independent density matrix of the emitted field

To describe the properties of the emitted light, we need to introduce the time-independent density matrix  $\rho_f$ . To represent annihilation of a photon at time  $t$ , let us introduce the operator  $a(t)$ , such that

$$[a(t), a^\dagger(t')] = \mathbb{1}\delta(t - t') \quad (2.1)$$

At different times there is a different probability of creation of a photon, and then of a second one, and so on. Let us represent this probability by an amplitude  $f_n(t_1, \dots, t_n)$ .

Now one can define time-independent Fock states as a superposition [97]

$$|n_f\rangle = \int \cdots \int_{-T}^T dt_1 \dots dt_n f_n(t_1, \dots, t_n) a^\dagger(t_1) \dots a^\dagger(t_n) |0\rangle \quad (2.2)$$

where  $T \rightarrow \infty$  is an integration time, that is much longer than all the characteristic times of the system. If there are multiple pulses, the distance between them being  $\Delta\tau$ , it is convenient to choose  $T = \Delta\tau/2$ . Multiple temporal modes are thus treated as a single mode.

The normalization of  $f_n$  is defined by the condition  $\langle n_f | m_f \rangle = \delta_{nm}$ :

$$\int \cdots \int_{-T}^T dt_1 \dots dt_n f_n(t_1, \dots, t_n) \sum_P f_n^*(t_{i_1}, \dots, t_{i_n}) = 1 \quad (2.3)$$

where the sum is over all the permutations of the indices. The number  $n$  in the state  $|n_f\rangle$  represents the number of clicks, registered by a time-resolving detector, integrated over time:  $n = \int dt \langle n_f | a^\dagger(t) a(t) | n_f \rangle$ .

The operator  $a^\dagger(t)$  can be expressed as a sum of the creation operators that represent creation of a photon in any moment but with a given frequency  $\omega$ :  $a^\dagger(t) = \sum_\omega e^{i\omega t} a^\dagger(\omega)$ . The same  $n$  would be obtained by integration of the number of clicks, registered by a frequency-resolving detector over the range of frequencies. Introducing the operator  $a^\dagger(\omega)$ , that creates a photon with frequency  $\omega$ , we express the same state:

$$|n_f\rangle = \int \cdots \int_\Omega d\omega_1 \dots d\omega_n \tilde{f}_n(\omega_1, \dots, \omega_n) a^\dagger(\omega_1) \dots a^\dagger(\omega_n) |0\rangle \quad (2.4)$$

where  $\tilde{f}_n$  is a Fourier transform of  $f_n$  over all the times.

If all the photons in  $|n_f\rangle$  are temporally uncorrelated, the  $f_n$  function is factorized:

$$f_n(t_1, \dots, t_n) = \frac{\prod_{i=1}^n f(t_i)}{\sqrt{n!}} \quad (2.5)$$

where  $f = f_1$ .

Then, a time-independent creation operator in the mode, defined by the temporal profile  $f(t)$ , can be introduced as

$$a^\dagger = \int_{-T}^T dt f(t) a^\dagger(t) = \int_{\Omega} d\omega \tilde{f}(\omega) a^\dagger(\omega) \quad (2.6)$$

and Eq. (2.2) can be expressed as

$$|n_f\rangle = \frac{(a^\dagger)^n}{\sqrt{n!}} |0\rangle \quad (2.7)$$

In what follows, we study the state of the field, with the following ansatz:

$$\rho_f = \sum_{n,m=0} \rho_{nm} |n_f\rangle \langle m_f| \quad (2.8)$$

and investigate how to characterize its purity  $\text{Tr}[\rho_f^2]$  using the observables  $N_{out}$ ,  $g^{(2)}$ ,  $N_1$ ,  $N_2$ ,  $g_{HOM}^{(2)}$ .

### 2.2.2 The numbers of photons in the detectors after the interferometer

The interference between two identical pulses of light, emitted from the same source can be observed in a set-up of the Fig. 2.1b. The equivalent way to represent the set-up is presented in Fig. 2.2. It focuses around the  $BS_2$ , where the two pulses of light field, in states  $\rho_f$  and  $\rho'_f$  respectively, Eq. (2.8), arrive at the inputs of the beam-splitter, after they have accumulated a phase difference  $\phi$ . We here assume that the temporal profile of the two pulses coincide, and the matrix elements of the two matrices are connected as

$$\rho'_{nm} = \rho_{nm} e^{i\phi(n-m)}$$

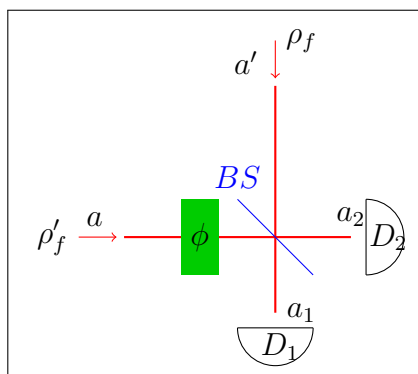


Figure 2.2: Scheme of the HOM experiment. The light moves along the red lines from top left to bottom right. The beam splitter is depicted in blue, phase shift is in green and the detectors are in black.

In this subsection we are focusing on the numbers of photons at the detectors at the output ports of the beam splitter, labelled as 1 and 2 in Fig. 2.2. They are calculated as

$$N_{1,2} = \langle a_{1,2}^\dagger a_{1,2} \rangle = \text{Tr}\{a_{1,2}^\dagger a_{1,2} (\rho_f \otimes \rho'_f)\} \quad (2.9)$$

where

$$a_{1,2} = \frac{a \pm a'}{\sqrt{2}} \quad (2.10)$$

The visibility of the interference fringes is defined as the difference between the normalized counts at the detectors

$$n_i = \frac{N_i}{\sum_{j=1}^2 N_j}, \quad i = 1, 2 \quad (2.11)$$

where  $N_i$  represents number of counts in the first of the second detector. The visibility is

$$V = \max_{\phi} [n_1(\phi) - n_2(\phi)] \quad (2.12)$$

In the most general case, the visibility between the single click rates in two detectors at the output of the beam splitter (labelled as 1 and 2) writes

$$V = \frac{|\sum_{n=1} \sqrt{n} \rho_{n,n-1}|^2}{\sum_{n=1} n P_n} \quad (2.13)$$

where  $P_n = \rho_{nn}$  are the diagonal elements of the density matrix  $\rho_f$ .

In what follows we are going to consider several examples of the incident state  $\rho_f$ .

### Example: single photon

In this example, the initial state contains exactly 1 photon:

$$\rho_f = |1\rangle\langle 1|, \quad \rho'_f = |1'\rangle\langle 1'|$$

where the number states represent the states  $|n_f\rangle$  as in Eq. (2.2) in the modes  $a$  and  $a'$ . The subscript  $f$  for the Fock states is omitted for the brevity, as we assume that the density matrices of the two pulses have the same temporal profile  $f$ .

It corresponds to the ordinary HOM effect [90]: two indistinguishable photons arrive at the beam splitter and get out of it in the superposition of photon pairs:

$$|1, 1'\rangle \rightarrow \frac{|2_1, 0_2\rangle - |0_1, 2_2\rangle}{\sqrt{2}}$$

the subscripts indicating the corresponding modes ( $a_1, a_2$ ). In the following, these indices will be omitted.

As the single photons have no defined phase, the phase, acquired by the pulse, consisting of a single photon, will not change the expression above: there will appear a common prefactor  $e^{i\phi}$ , that does not affect the expectation values of the measured observables. Though the photons bunch, on average the photon pairs go to the two detectors with equal probability, hence, the distribution of clicks between detectors 1 and 2 will be symmetrical:

$$N_1 = N_2, \quad V = 0$$



### Case of 1 photon + vacuum

If the initial state is in a coherent superposition of 0-photon and 1-photon states, there appears an asymmetry in clicks distribution, that depends on the phase difference  $\phi$  between 0- and 1-photon components. We assume here that the states of light at the inputs of the beam splitter are pure:

$$\begin{aligned} |\psi\rangle &= \sqrt{P_0}|0\rangle + \sqrt{P_1}e^{i\phi_1}|1\rangle \\ |\psi\rangle &= \sqrt{P_0}|0\rangle + \sqrt{P_1}e^{i(\phi_1+\phi)}|1\rangle, \end{aligned}$$

where  $\phi_1$  is the initial phase between 0- and 1-photon components.

The beam splitter transforms the initial state into the state with phase-dependent distribution of the clicks between the detectors 1 and 2:

$$\begin{aligned} |\psi, \psi'\rangle &\rightarrow \\ P_0|0, 0\rangle + \sqrt{2P_0P_1}e^{i\phi_1}e^{i\phi/2} &\left[ |1, 0\rangle \cos \frac{\phi}{2} + i|0, 1\rangle \sin \frac{\phi}{2} \right] \\ &+ \frac{P_1e^{i(2\phi_1+\phi)}}{\sqrt{2}} (|2, 0\rangle - |0, 2\rangle) \end{aligned}$$

The phase difference  $\phi$ , accumulated on the way through the interferometer before the second beam splitter, is added to the phase between the 0- and 1-photon components.

The maximal difference in clicks between the two detectors depends on the coherence between the vacuum and the single-photon components. If the state of light is a mixed state, according to the Eqs. (2.9)-(2.12),

$$V = \frac{|\rho_{01}|^2}{P_1} \quad (2.14)$$

Thus, the measurement of the visibility of the interference fringes gives us information on the coherence between 0 and 1 photons.

For a pure state,  $|\rho_{01}|^2 = P_0P_1$ ,

$$V = P_0$$

One can relate  $P_n$  to the excited state population of an ideal TLS in a guide, pumped by a short laser pulse of area  $\theta$ . The number of emitted photons corresponds to the excited state population of the TLS:  $P_1 = \sin^2(\frac{\theta}{2})$  and  $P_0 = \cos^2(\frac{\theta}{2})$ . Then, for a pure state we have

$$V = P_0 = \cos^2\left(\frac{\theta}{2}\right) \quad (2.15)$$

Otherwise, if the state of light is initially mixed, one can introduce a parameter  $\lambda$ , that quantities diminishing of the purity as  $|\rho_{01}|^2 = \lambda(\theta)^2 P_0P_1$ . The dependence of the visibility on the pulse area  $\theta \leq \pi$  for different purities of the emitted light is shown in Fig. 2.3.

For the state, including only vacuum and single-photon components the purity writes  $P = 1 - 2(P_0P_1 - |\rho_{01}|^2)$ . The measurement of  $N_1$  and  $N_2$  allows us to find it from a single experiment: the average total number of registered photons  $N_1 + N_2$  is equal to  $P_1$ , and the visibility of the oscillations  $V$  reveals the value of  $|\rho_{01}|^2$ .

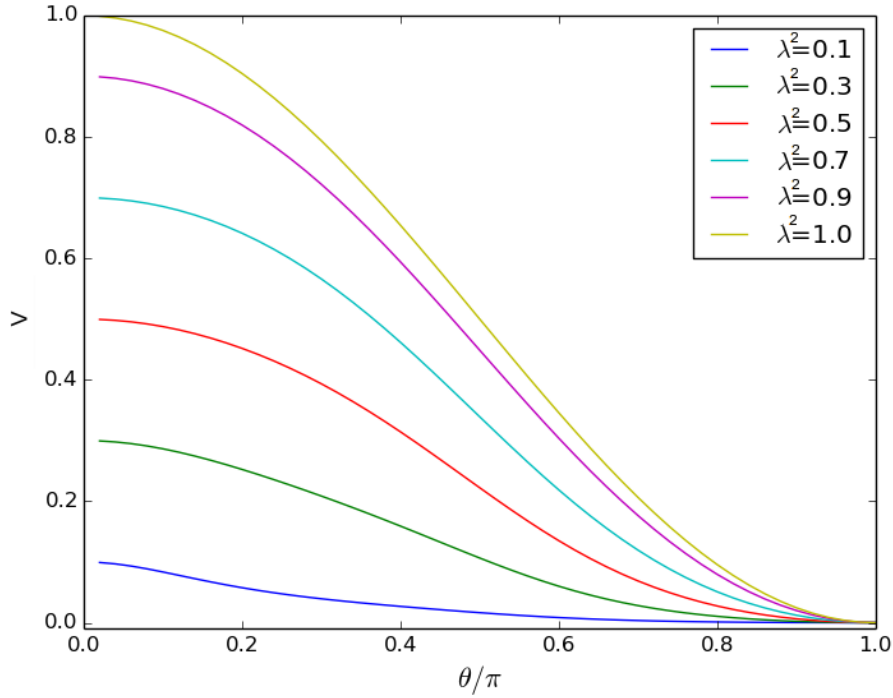


Figure 2.3: Visibility of the interference fringes as a function of the incident pulse area for a mixed initial state with  $\rho_{01} = \sqrt{P_0 P_1} \lambda$ , where  $\lambda = \text{const.}$

### Case of 2 photons + vacuum

The initial state contains a superposition of 0- and 2-photon states,  $P_1 = 0$ ,  $\rho_{i=1,j} = \rho_{i,j=1} = 0$ .

The states of light in the inputs of the beam splitter are assumed to be pure:  $|\psi\rangle = \sqrt{P_0}|0\rangle + \sqrt{P_2}e^{i\phi_2}|2\rangle$  and  $|\psi'\rangle = \sqrt{P_0}|0\rangle + \sqrt{P_2}e^{i(\phi_2+\phi)}|2\rangle$ . The beam splitter transformation is

$$\begin{aligned}
 & |\psi, \psi'\rangle \rightarrow \\
 & P_0|0,0\rangle + \sqrt{P_0 P_2} e^{i\phi_2} e^{i\phi/2} \left[ (|2,0\rangle + |0,2\rangle) \cos^2 \frac{\phi}{2} + \sqrt{2} \sin^2 \frac{\phi}{2} |1,1\rangle \right] \\
 & + \frac{P_2 e^{i(2\phi_2+\phi)}}{2} \left[ \sqrt{\frac{3}{2}} (|4,0\rangle + |0,4\rangle) - |2,2\rangle \right]
 \end{aligned}$$

This expression is symmetrical under a transformation that exchanges the first and the second mode, so on average, the same number of photon will be detected in each detector whatever the phase  $\phi$ :

$$V = 0.$$

In this case we still can find both of the density matrices' diagonal elements from the average photon number measurement, but to access the non-diagonal element  $\rho_{02}$  one needs to measure the two-photon correlations as will be explained below.

### Case of vacuum + one- and two-photon states

Let us now consider the general case when the initial state of the emitted light is described by a density matrix (2.8), including up to 2-photon states. It corresponds to the light, emitted by a TLS, that was excited by a short pulse of any area  $\theta$ , as will be demonstrated in the following section.

The visibility, according to the Eq. (2.13), in this case writes

$$V = \frac{|\rho_{01}|^2 + 2\sqrt{2}\text{Re}(\rho_{01}\rho_{12}^*) + 2|\rho_{12}|^2}{P_1 + 2P_2} \quad (2.16)$$

where Re means the real part.

The quadratic combination of the coherences between the  $|n\rangle$  and  $|n+1\rangle$  states  $\rho_{n,n+1}$  in the numerator of Eq. 2.16 is not the same as in the expression for the purity, thus we can't calculate the purity directly from the visibility measurement. However, its value can be estimated from a comparison of  $V$  with the value of  $V$  for the pure state.

According to the Eqs. 2.11, 2.12, 2.13, in order to find this combination of the coherences from the measurement of the visibility, we must know the total number of photons in the field  $N_1 + N_2$ . The visibility and the total numbers of photons are measured in different set-ups, Fig. 2.1b and Fig. 2.1a correspondingly. The distance between the emitter and the detectors differs between the set-ups. As the losses on the way depend on the distance, and the light pulses travel different distance in the two set-ups, the rate of the losses will differ as well. It is hence important to show that this difference does not affect the measurement, and though the states of light at the detectors are not identical between the two set-ups, the measurements in the both of them reveal the information on the same state of light.

### Influence of the losses on the way on the visibility

Let us consider losses on the way between the emitter and the interferometer. At the Fig. 2.1b they are shown by a grey rectangle. We consider a case of losses that can be modelled as a beam-splitter with transmittance  $t$  and reflectance  $r$ .

We assume the emitted light to be in a pure state and to include up to 2 photons:  $|\psi\rangle = C_0|0\rangle + C_1|1\rangle + C_2|2\rangle$ , where  $|C_i|^2 = P_i$ . The part of light that went to the  $t$  mode is considered lost, and the density matrix is traced over this degree of freedom.

The resulting density matrix of the light state after the losses, modelled by a beam-splitter, will be:

$$\rho' = \begin{pmatrix} P_0 + P_1|t|^2 + P_2|t|^4 & C_0C_1^*r^* + \sqrt{2}C_1C_2^*r^*|t|^2 & C_0C_2^*(r^*)^2 \\ C_0^*C_1r + \sqrt{2}C_1^*C_2r|t|^2 & P_1|r|^2 + 2P_2|r|^2|t|^2 & C_1C_2^*|r|^2r^* \\ C_0^*C_2r^2 & C_1^*C_2|r|^2r & P_2|r|^4 \end{pmatrix} \quad (2.17)$$

By substituting this density matrix into (2.16), one may retrieve the expression for the pure state: it means that the losses do not change the visibility, as was shown experimentally by the C2N team, see Fig. 2.4.

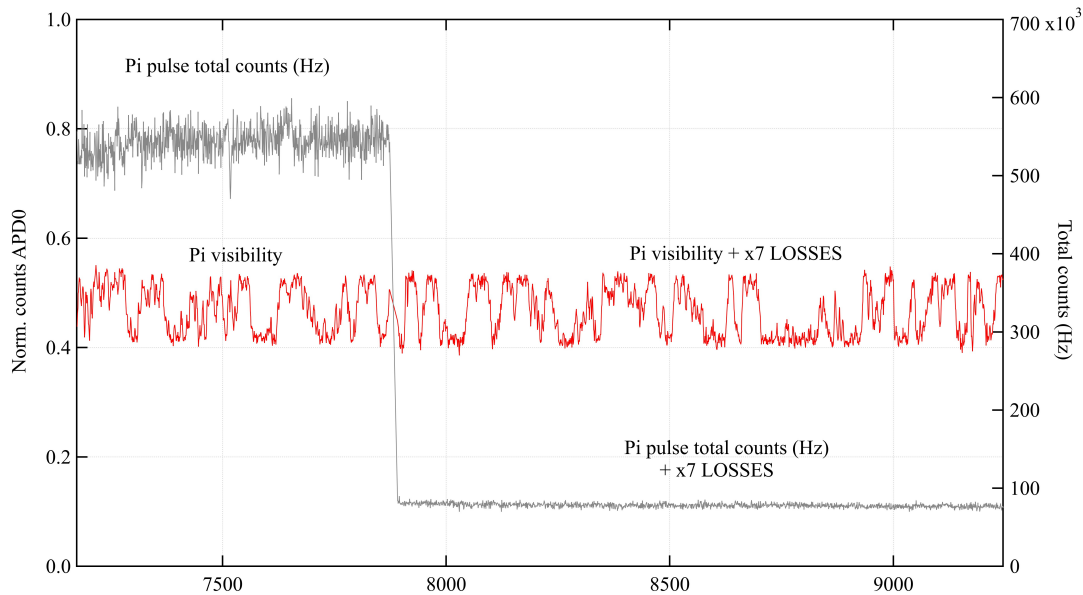


Figure 2.4: Normalized counts ( $n_i$  in notation of the chapter) in one of the detectors (red, left scale) and laser power (black, right scale) as a function of time. The step corresponds to the introduction of the losses. The visibility remains the same: the upper and lower bounds of the red curve do not change.

### 2.2.3 Distinguishable photons

The mismatching of modes, in which the subsequent light pulses are emitted by a TLS, reduces the effect of the photon interference [97]. In this subsection we would like to focus on two particular cases of this mode mismatch, namely the difference in the polarization of light in subsequent pulses and the reduced overlap between the temporal profiles of their wave-packets.

#### Different polarizations

Let us introduce the wave-plate that rotates the polarization of the light in the 'long' branch of the interferometer by the angle  $\vartheta_p$ . At the Fig. 2.1b it is marked in magenta.

In the auxiliary set-up of Fig. 2.2 this will correspond to changes in the polarization of light in the  $a$  mode. In this case the annihilation operator  $a$ , that is assumed to annihilate a horizontally polarized photon, is replaced by the operators corresponding to the horizontal and vertical polarizations:

$$a \rightarrow a_h \cos \vartheta_p + a_v \sin \vartheta_p \quad (2.18)$$

The mode  $a'$  is assumed to be horizontally polarized, so it interferes only with  $a_h$ .

The modes after the second beam-splitter are represented by operators

$$\begin{aligned} a_{1,h} &= \frac{a_h + a'}{\sqrt{2}} & a_{2,h} &= \frac{a_h - a'}{\sqrt{2}} \\ a_{1,v} &= \frac{a_v}{\sqrt{2}} & a_{2,v} &= \frac{a_v}{\sqrt{2}} \end{aligned} \quad (2.19)$$

We assume that the detectors do not resolve the polarizations, and detect in both of them. The numbers of detected photons are found as expectation values on the density matrix, defined with Eqs. (2.7), (2.8) and (2.18):

$$N_{1(2)} = \langle a_{1(2),h}^\dagger a_{1(2),h} + a_{1(2),v}^\dagger a_{1(2),v} \rangle.$$

The visibility found from this equation is proportional to the amount of the light in the mode  $a$ , that is polarized as the light in the mode  $a'$ :

$$V = V \Big|_{\vartheta_p=0} |\cos \vartheta_p| \quad (2.20)$$

The orthogonally polarized pulses of light will not interfere and there will be no fringes to be visible, and the light with the same polarizations will produce the maximally visible fringes.

### Different shapes of wave-packets

Describing the state of the field in the beginning of this section, we assumed that all the photons that take part in the interference, have the same temporal profile, which is not always the case, even for the light, emitted by the same emitter [92,93].

A more general description would be to replace the factorization (2.5) by

$$f_n(t_1, \dots, t_n) = \frac{\prod_{i=1}^n f^{(i)}(t_i)}{\sqrt{n!}} \quad (2.21)$$

where the functions  $f^{(i)}$  may differ between each other. The state of light, described by  $|n_f\rangle$ , Eq. (2.2), with  $f_n$  from Eq. (2.21) is a coherent superposition of wave packets, that may not fully overlap.

Let us concentrate on the case of light that includes up to one photon, that was considered in the example 2.2.2. In this case the photon in mode  $a$  was emitted with temporal profile  $f(t)$ , and the photon in the mode  $a'$  - with a different profile, let us call it  $g(t)$ .

$$\begin{aligned} |1_f\rangle &= \int_{-T}^T dt f(t) a^\dagger(t) |0\rangle \\ |1_g\rangle &= \int_{-T}^T dt g(t) (a'(t))^\dagger |0\rangle \end{aligned}$$

The state of light in this case is  $|\psi_f, \psi_g\rangle$ , with  $|\psi_f\rangle = \sqrt{P_0}|0\rangle + \sqrt{P_1}e^{i\phi_1}|1_f\rangle$  and  $|\psi_g\rangle = \sqrt{P_0}|0\rangle + \sqrt{P_1}e^{i(\phi_1+\phi)}|1_g\rangle$ .

Their temporal and spectral overlap is defined as

$$\mathcal{M} = \int dt f(t)g^*(t) = \int dt \langle 1_g | a^\dagger(t)a'(t) | 1_f \rangle \sim \int d\omega \tilde{f}(\omega)\tilde{g}^*(\omega) \quad (2.22)$$

where the tilde indicates the Fourier transform, and the overlap can reach complex values in  $|\mathcal{M}| \leq 1$ . It is more current in literature to use a real number  $M = |\mathcal{M}|^2$  to quantify the overlap [92, 93].

The numbers of photons in each detector are:

$$N_{1,2} = \int_{-T}^T dt \langle \psi_f, \psi_g | a_{1,2}^\dagger(t)a_{1,2}(t) | \psi_f, \psi_g \rangle \quad (2.23)$$

And the visibility becomes

$$V = V \Big|_{\mathcal{M}=1} \text{Re}(\mathcal{M}) \quad (2.24)$$

In a more general approach a single-photon state is presented not as a superposition, but as a mixture of different temporal modes:

$$\begin{aligned} \rho_{1,f} &= \int dt_1 dt_2 f(t_1, t_2) a^\dagger(t_1) |0\rangle \langle 0| a(t_2) \\ \rho_{1,g} &= \int dt_1 dt_2 g(t_1, t_2) a^\dagger(t_1) |0\rangle \langle 0| a(t_2) \end{aligned}$$

The overlap  $\mathcal{M}$  in Eq. (2.24) is then defined as

$$\mathcal{M} = \sqrt{\text{Tr}[\rho_{1,f}\rho_{1,g}]} \quad (2.25)$$

The visibility is thus reduced due to two factors: the loss of coherence in the photon number basis, and the imperfect indistinguishability of the photons. Therefore, to evaluate the purity of the state experimentally, one needs to measure the mean wave-packet overlap  $\mathcal{M}$  and make sure that the polarizations of the interfering fields coincide.

## 2.2.4 The 2-photon correlation functions

The visibility gives us access to the coherences between the  $|n\rangle$  and  $|n+1\rangle$  states. As even in the case of the short pulsed excitation it is possible for a TLS to emit two photons [86], we need another observable that would give us access to  $\rho_{20}$  and other coherences between  $|n\rangle$  and  $|n+2\rangle$  states. As will be shown below, this information can be obtained from the measurements of the coincidences between the clicks in the two detectors after the interferometer.

Again, the interference of two subsequent pulses, emitted by the same TLS can be investigated through the auxiliary set-up of Fig. 2.2, where two copies of the same state, but with different phases, interfere on a beam-splitter.

The number of coincidences and the second order autocorrelation function write

$$G_{HOM}^{(2)} = \gamma^2 \text{Tr}\{a_1^\dagger a_2^\dagger a_2 a_1 (\rho_f \otimes \rho'_f)\} \quad (2.26a)$$

$$g_{HOM}^{(2)} = \frac{G_{HOM}^{(2)}}{(\sum_i N_i)^2} \quad (2.26b)$$

where the light after the beam splitter is described by the operators

$$a_{1,2} = \frac{a \pm a'}{\sqrt{2}} \quad (2.27)$$

Substituting them into the expression for  $G_{HOM}^{(2)}$ , we obtain the general expression for the 2-photon correlation function after the beam splitter, if the initial state is represented as a time-independent density matrix  $\rho_f$ . It writes

$$G_{HOM}^{(2)} = \frac{1}{2} \left[ \sum_{n=2} n(n-1)P_n - \cos(2\phi) \left| \sum_{n=2} \sqrt{n(n-1)}\rho_{n,n-2} \right|^2 \right] \quad (2.28)$$

Let us introduce the number of the coincidences in the detectors after the emitter, that can be measured in a set-up in Fig. 2.1a:

$$G^{(2)} = \gamma^2 \text{Tr}\{a^\dagger a^\dagger a a \rho_f\} = \sum_{n=1} n(n-1)P_n \quad (2.29)$$

The link between the quantities before and after the interferometer is

$$G_{HOM}^{(2)} = \frac{G^{(2)}}{2} - \frac{\cos(2\phi) \left| \sum_{n=2} \sqrt{n(n-1)}\rho_{n,n-2} \right|^2}{2} \quad (2.30)$$

For the case, when there are no more than 2 photons in the emitted light, it simplifies to

$$G_{HOM}^{(2)} = P_2 - \cos(2\phi) |\rho_{02}|^2 \quad (2.31)$$

Thus, the measurement of the  $G_{HOM}^{(2)}$  function allows to access the value of  $|\rho_{02}|$ .

The autocorrelation function  $g_{HOM}^{(2)}$  does not change with the losses. This can be seen from substituting of the density matrix Eq. (2.17) into the last equation and the definition of the  $g_{HOM}^{(2)}$  Eq. (2.26b).

### 2.2.5 Summary of the section

In this section we considered the state of light, emitted by a TLS, described by an 'ad hoc' density matrix  $\rho_f$ , Eq. (2.8). The basis, used for this description, represents the superposition states of light, containing  $n$  photons in multiple temporal modes, Eq. (2.2). The light field is emitted in subsequent pulses, each described by a copy of the density matrix  $\rho_f$ . These pulses interact with each other in a Mach-Zehnder interferometer, Fig. 2.1b, and the detectors at the output of the set-up measure two quantities: 1) the visibility of the interference fringes  $V$  that is defined as a difference between the clicks in the detectors, normalized with a total number of detected photons, and 2) the coincidences between the clicks  $G_{HOM}^{(2)}$ .

The visibility of the interference fringes  $V$  gives us access to the coherences between states  $|n\rangle$  and  $|n+1\rangle$ . The coincidences after the beam splitter  $G_{HOM}^{(2)}$  or the correlation function between the light in two detectors  $g_{HOM}^{(2)}$  allow us to measure

the coherences between states  $|n\rangle$  and  $|n+2\rangle$ . The knowledge of these elements is required to estimate the purity of the state of the emitted light.

We also showed that both the visibility and the correlation function of the light in the interferometer remains constant in the presence of losses in the channels. This means that other set-ups, that have different losses, may be used to measure the number of photons in the pulse and the autocorrelation functions.

We also studied the effect on the visibility of the polarizations mismatch and the non-overlapping wave-packets, both being the cases of the distinguishable photons.

In what follows we would like to apply these results to the light, emitted by a TLS with the connection to the dynamics of the emitter.

## 2.3 Simulations

In this section we are simulating the dynamics of the emission of a semiconductor quantum dot in a directional micropillar cavity in order to describe an experiment by the C2N group in Marcoussis, and to understand better the underlying physics.

The experimental system was presented in Fig. 1.6 of the previous chapter. It consists of a semiconductor quantum dot, embedded into a micropillar cavity. It is excited by a pulsed laser, and the reflected light passes through a polarizing beam-splitter. The polarization, orthogonal to the excited laser, is collected, and passes through one of the set-ups, shown in Fig. 2.1.

Simulating the emission, we will be able to find the diagonal elements of the electromagnetic field density matrix. In the following, we construct a state with diagonal elements in the form  $|\rho_{nm}| = \lambda\sqrt{P_n P_m}$ , and by comparing it with the experimental data via fitting  $\lambda$ , we will be able to evaluate the purity of the emitted light state.

### 2.3.1 Idealized system

The emitter is modelled as a TLS with excited and ground levels  $|e\rangle$  and  $|g\rangle$ , placed in a wave guide and excited with repeated pulses of a laser, resonant with the energy difference between the TLS levels, through another channel, so that the input and the output pulses do not interfere. The emission is directed into the guide, as in Fig. 2.5.

The state of the TLS is described by a density matrix  $\rho_q(t) = \sum_{i,j=\{e,g\}} \rho_{q,ij}(t)|i\rangle\langle j|$ , and the evolution is governed by the Lindblad equation [58]:

$$\dot{\rho} = -\frac{i}{\hbar} [H, \rho] + D_{\gamma, \sigma}[\rho] + D_{\gamma^*, \sigma_z}[\rho] \quad (2.32)$$

where  $\sigma = |g\rangle\langle e|$  is a lowering operator,  $\sigma_z = [\sigma^\dagger, \sigma]$ ,  $\gamma$  and  $\gamma^*$  are spontaneous emission and pure dephasing rates, and

$$D_{\alpha, A}[\rho] = \frac{\alpha}{2} (2A\rho A^\dagger - A^\dagger A\rho - \rho A^\dagger A) \quad (2.33)$$



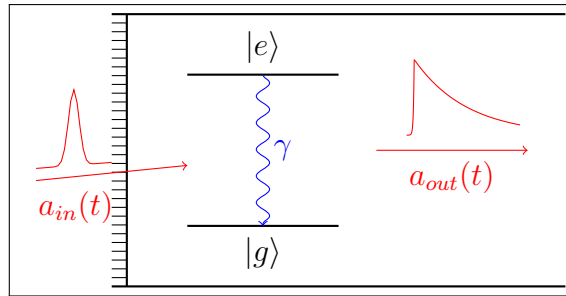


Figure 2.5: A TLS, excited with repeated pulsed excitations with light emitted into the propagating mode.

where we assume  $\hbar = 1$ . The unitary part of the evolution of the TLS is described by the Hamiltonian in the frame, rotating at the frequency  $\omega_q$

$$H(t) = i\sqrt{\beta\gamma N_{in}}\xi(t) (\sigma - \sigma^\dagger) \quad (2.34)$$

where  $\beta$  is a proportion of the photons emitted towards the detector,  $N_{in}$  is a number of incident photons, that is defined by the pulse area and  $\xi(t)$  is a Gaussian temporal profile with full width at half maximum  $\tau$ :

$$\xi(t) = \left(\frac{4 \ln(2)}{\pi\tau^2}\right)^{1/4} \exp(-t^2/\tau^2 8 \ln(2)).$$

We will focus on the case of short pulses  $\tau \ll \gamma^{-1}$ , unless specified otherwise. The excitation area is defined as

$$\theta = \sqrt{\beta\gamma N_{in}} \int dt \xi(t).$$

The impact of the electromagnetic environment on the TLS is modelled through non-unitary terms in the Eq. (2.32). The observables describing the field, radiated by the TLS, are found from the density matrix of the TLS  $\rho_q(t)$  and the input-output relation [58]

$$a_{out} = \sqrt{\gamma}\sigma \quad (2.35)$$

### 2.3.2 Fock states occupation probabilities

Building on this premises, let us find the probabilities  $P_n$  that there are  $n$  photons in the electromagnetic field, emitted during a pulse. For this purpose we need to define the mean number of photons in the pulse of emitted light and its autocorrelation functions. The set-up to measure these properties of the emitted light is shown in Fig. 2.1a.

$$N_{out} = \gamma \int_0^\infty dt \text{Tr}\{\sigma^\dagger \sigma \rho_q(t)\} \quad (2.36a)$$

$$G^{(2)} = \gamma^2 \iint dt d\tau \text{Tr}\{\sigma^\dagger \sigma \mathcal{L}_{t,t+\tau}[\sigma \rho_q(t) \sigma^\dagger]\} \quad (2.36b)$$

$$G^{(3)} = \gamma^3 \iiint dt d\tau d\tau' \text{Tr}\left\{\sigma^\dagger \sigma \mathcal{L}_{t+\tau,t+\tau+\tau'}\left[\sigma \mathcal{L}_{t,t+\tau}[\sigma \rho_q(t) \sigma^\dagger]\sigma^\dagger\right]\right\} \quad (2.36c)$$

Here  $\mathcal{L}_{t,t+\tau}[\rho(t)]$  is an evolution operator between times  $t$  and  $t + \tau$  with an initial state  $\rho(t)$ , it represents the solution of the Eq. (2.32).

The definitions of the above quantities can be used to find the occupation probabilities of different Fock states. As will be shown below, in the case of a short pulse it is sufficient to account up to two photons. Here we give the value for  $P_3$  only to show that it is negligible.

$$P_3 = \frac{G^{(3)}}{6} \quad (2.37a)$$

$$P_2 = \frac{G^{(2)} - G^{(3)}}{2} \quad (2.37b)$$

$$P_1 = N_{out} - G^{(2)} + \frac{G^{(3)}}{2} \quad (2.37c)$$

$$P_0 = 1 - P_3 - P_2 - P_1 \quad (2.37d)$$

As we are assuming that the state of light is pure, the non-diagonal elements of the density matrix Eq. (2.8) are defined as  $\rho_{nm} = \sqrt{P_n P_m}$ .

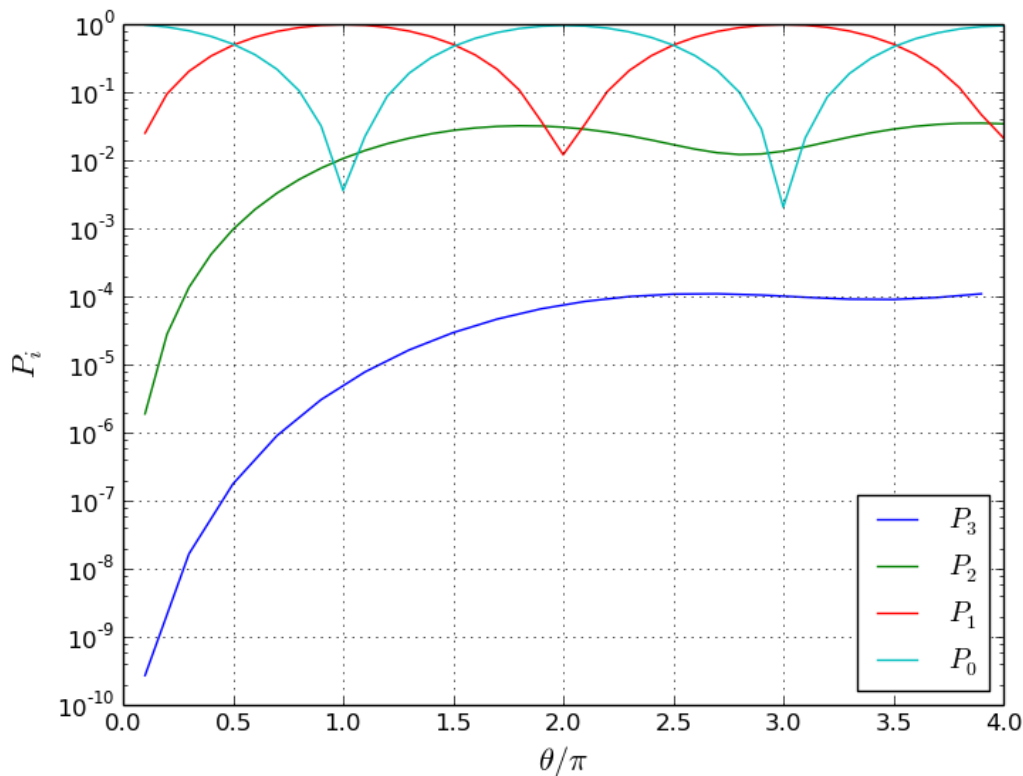


Figure 2.6: Probabilities  $P_i$  that the reflected pulse contains  $i$  photons. Simulation for the ideal parameters ( $\beta = 1$ ,  $\gamma^* = 0$ ).

The diagonal elements of the density matrix of the emitted light  $P_n$  as functions of the excitation area  $\theta$  are presented in Fig. 2.6. For the low power excitation, the vacuum component is dominant, and with the grows of power it decreases, and the single-photon component increases, reaching maximum for the  $\pi$ -pulse, and

then decreasing due to the QD saturation and exhibiting Rabi oscillations. Similar behaviour is shown by the two- and three-photon components, however they reach lower values due to the short duration of pulse and low probability to emit multiple photons, re-exciting after the first emission.

### 2.3.3 Excitation of area below $\pi$

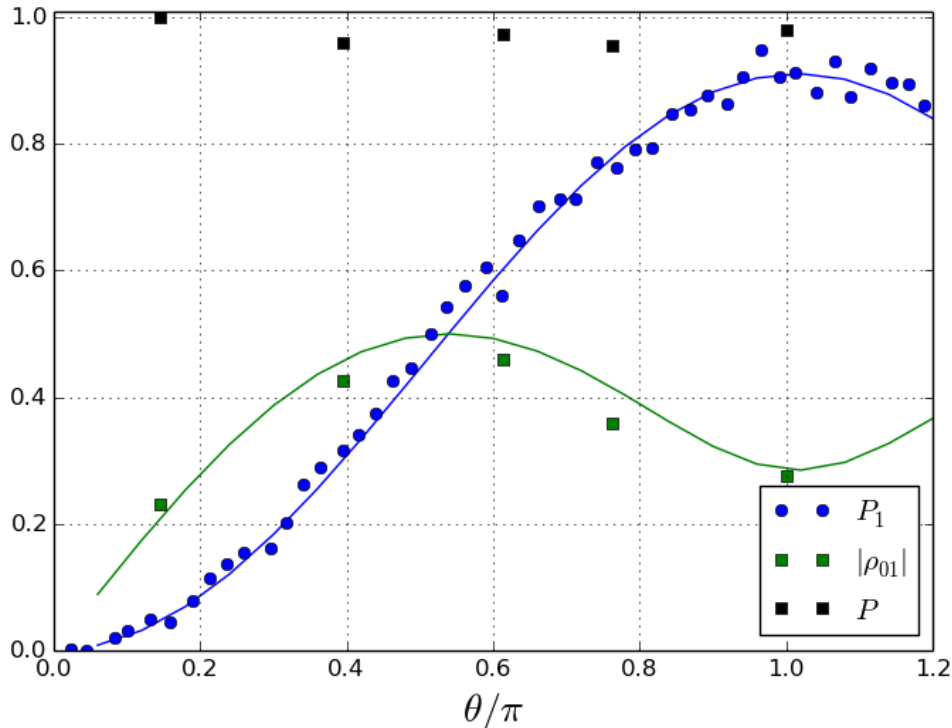


Figure 2.7: The elements of the density matrix of the emitted light, retrieved from the experiment. The blue and the green lines (points) show the simulated (measured)  $P_1$  and  $|\rho_{01}|$ , and the black squares show the purity  $P$  deduces from the measurements. The simulation parameters are  $\gamma^{-1} = 160$  ps,  $\gamma^* = 0.03\gamma$ ,  $\tau = 30$  ps,  $\beta = 0.95$ . The experimental value of the wave packet overlap  $M = 0.9$ .

Under the excitation of areas  $\theta \leq \pi$ , the emitted light consists mostly of vacuum and single-photon components. Even though for an ideal system of the Fig. 2.6  $P_2 > P_0$ , for the experimental system, due to the pure dephasing and non-perfect  $\beta$ , the two-photon component is reduced up to  $0.1P_0$  and can be ignored. Therefore, the emitted light is much similar to the case of subsect. 2.2.2.

The behaviour of the density matrix element of the emitted light is shown in Fig. 2.7. The blue line shows the QD probability to emit a single photon  $P_1$ , and the green line shows the calculated quantity  $\sqrt{P_1 P_0}$ , representing the value of the  $\rho_{01}$  for a pure state. The point show the values of these quantities, extracted from the experiments, and the black squares on top depict the purity of the state  $P$ , that has quite high values, with the average of  $P = 0.968 \pm 0.008$  for this device.

The high purity of the emitted state shows that the coherently driven TLS emits a coherent superposition of the vacuum and the single-photon states. This means that the coherence of the initial driving laser is transferred to the emitted light state.

### 2.3.4 The $2\pi$ excitation

At the  $2\pi$  pulse the TLS is excited and then returned to the ground state during a pulse, coherently exchanging energy with the drive. If the pulse is not infinitely short, there is a non-zero probability of the TLS spontaneously emitting photons. If one photon is emitted during the pulse, the TLS can be re-excited to emit the second one [86]. For the ideal case of Fig. 2.6,  $P_2 > P_1$ . This means that we can't neglect the 2-photon component for this case. Therefore, let us now turn to the simulations of the second-order correlation function of the light.

The two-photon autocorrelation function of the light before the interferometer  $g^{(2)}$  writes

$$g^{(2)} = \frac{G^{(2)}}{N_{out}^2} \quad (2.38)$$

where  $G^{(2)}$  and  $N_{out}$  were defined in the Eq. (2.36).

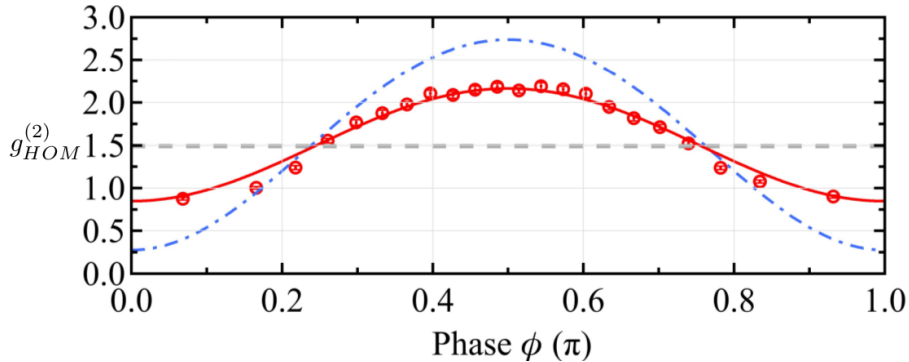


Figure 2.8: Normalized coincidences  $g_{HOM}^{(2)}$  as a function of the phase  $\phi$ , measured in the C2N group. The dashed blue (grey) line: the theoretical prediction for the pure (maximally mixed) state. The red line: the theoretical prediction for the state, described with parameters  $P_0 = 0.838$ ,  $P_1 = 0.051$ ,  $P_2 = 0.111$ ,  $\lambda = 0.734$ . The red dots present the measured data.

The correlation function of the field at the output of the interferometer  $g_{HOM}^{(2)}$ , is calculated according to the Eqs. (2.26b) and (2.28). For the 2-photon cases it writes

$$g_{HOM}^{(2)} = \frac{P_2 - \cos(2\phi) |\rho_{20}|^2}{(P_1 + 2P_2)^2} \quad (2.39)$$

It has the

In the presence of the two-photon component we can't find the purity directly from the measured values. To solve this problem, we assume that all the coherences  $\rho_{nm}$  are reduced the same way, so that

$$|\rho_{nm}| = \lambda \sqrt{P_n P_m} \quad \forall n \neq m \quad (2.40)$$

This  $\lambda$  includes not only the purity in the photon-number basis, but the reduced overlap between the wave-packets.

With this assumption, we have four equations to find  $P_{0,1,2}$  and an upper bound on  $\lambda$ :

$$V \leq \lambda^2 P_1 \frac{(P_0 + 2\sqrt{2P_0P_2} + 2P_2)}{P_1 + 2P_2}$$

$$g_{HOM}^{(2)} = \frac{P_2 [1 - \cos(2\phi)\lambda^2 P_0]}{(P_1 + 2P_2)^2}$$

$$g^{(2)} = \frac{2P_2}{(P_1 + 2P_2)^2}$$

$$P_0 + P_1 + P_2 = 1$$

The “ $\leq$ ” sign in the first of these equations appears because the Eq. (2.16) involves taking the real part of a complex number, that is bounded by its absolute value.

The behaviour of the  $g_{HOM}^{(2)}$  as a function of the phase accumulated in the interferometer is shown in Fig. 2.8, where the lines show the theoretical prediction, and the dots - the experiment.

## 2.4 Summary

In this chapter we studied the properties of the electromagnetic field emitted by an ideal TLS in a guide in a superposition of Fock states. We explored the emitted light within an ‘ad hoc’ model of a time-independent state, that is not entangled to emitter. We found two observables that allow to access the coherences between the  $|n\rangle$  state and  $|n+1\rangle$  and  $|n+2\rangle$  states. We also shown that these observables do not change their values in the presence of losses and investigated the influence of the non-indistinguishability of the photons.

In the second part we applied the model to the experimental data, obtained by the C2N team, that shows that the state of art technology allows to create high-purity superpositions of number states, with the ability to control the distribution.

This work is to be continued by building a more complete theoretical model, that is able to predict the values of the non-diagonal density matrix elements, the pure dephasing and the reduced overlap between temporal profiles of the pulses.

# Chapter 3

## Spin-photon interface as a quantum meter

### 3.1 Introduction

Single solid-state spins are among the most promising candidates on the role of building blocks of quantum networks. One of the reasons behind this is that coherence time of electron and hole spins is several orders of magnitude longer, than all the other characteristic times [37, 98–100], that is one of the criteria to fulfil for a system to be used as a stationary qubit [16]. A massive effort has been recently devoted to developing quantum operations with single spins, implemented in donor impurities in diamonds [27] or in silicon [101], magnetic impurities [102], single donor spins [103] and doped semiconductor quantum dots [104–106] and to realizing spin-photon interfaces [107, 108].

A stationary quantum bit can be realized by encoding a quantum state in the state of a single spin, that can be optically addressed. Hence, one of the important milestones on the road to the spin-based quantum computing is the ability to measure the spin state [16].

#### 3.1.1 Strong and weak measurements

Traditionally, quantum mechanical measurements can be ultimately understood with the projective measurements. Let us consider the situation, shown in Fig. 3.1: a quantum system  $\mathcal{S}$  interacts with a measuring apparatus  $\mathcal{M}$ . The observable  $M$  measured by  $\mathcal{M}$  has eigenstates  $\{|m_\mu\rangle\}_{1\leq\mu\leq d}$ , where  $d$  is the dimension of the Hilbert space of the system  $\mathcal{S}$  and writes

$$M = \sum_{\mu=1}^d m_\mu \pi_\mu,$$

where  $m_\mu$  is the measurement outcome and  $\pi_\mu = |m_\mu\rangle\langle m_\mu|$  are projection operators.

After the measurement  $\mathcal{S}$  is instantaneously projected onto the eigenstate  $|m_\mu\rangle$  that corresponds to the measurement outcome: if the state of the system before the

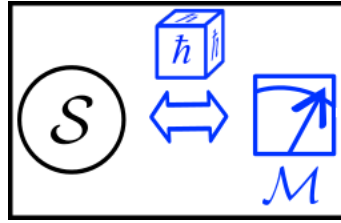


Figure 3.1: Strong measurement: a quantum system  $\mathcal{S}$  interacts with a measuring apparatus  $\mathcal{M}$ . The outcomes of measurements performed by  $\mathcal{M}$  (shown as dice with  $\hbar$ ), as well as its back-action, are stochastic. (Figure from [109])

measurement was  $|\Psi(t)\rangle$ , after it will be

$$|\Psi_\mu(t)\rangle = \frac{\pi_\mu |\Psi(t)\rangle}{\sqrt{P_\mu(t)}} = |m_\mu\rangle \quad (3.1)$$

where the probability of the outcome  $m_\mu$  is distributed according to the Born's rule  $P_\mu(t) = \langle \Psi(t) | \pi_\mu | \Psi(t) \rangle$  [110].

This approach can be extended on the time evolution. We assume here that there is a set of  $N$  measurements at time instants  $\{t_n\}_{1 \leq n \leq N}$ , each of them projects the system onto one of the eigenstates  $\{|m_\mu\rangle\}_{1 \leq \mu \leq d}$ , corresponding to the measured value of  $m_\mu$ . Between these times the system evolves according to the unitary Schrödinger Equation.

If the measurement outcomes are read, each of them has a random effect on the state of  $\mathcal{S}$ . In each realization of such an evolution  $\mathcal{S}$  follows a given stochastic trajectory  $\gamma$ , which is defined as a sequence of quantum states that correspond to the measurement outcomes  $\{m_\mu^\gamma(t_n)\}$  at times  $\{t_n\}_{1 \leq n \leq N}$ .

If the measurement outcomes are not read, the system is described by the density matrix

$$\bar{\rho}(t) = \sum_\mu P_\mu(t) |\Psi_\mu(t)\rangle \langle \Psi_\mu(t)| = \sum_\mu \pi_\mu |\Psi(t)\rangle \langle \Psi(t)| \pi_\mu = \sum_\mu P_\mu(t) |m_\mu^\gamma\rangle \langle m_\mu^\gamma| \quad (3.2)$$

which is the same as the average value over multiple trajectories. This matrix is diagonal in the basis of the measured observable eigenstates, which indicates a loss of coherence due to the measurement.

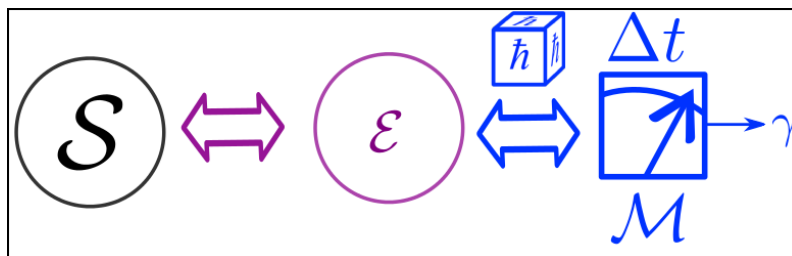


Figure 3.2: Weak measurement: a quantum system  $\mathcal{S}$  interacts with the environment  $\mathcal{E}$ , that is measured by the measurement apparatus  $\mathcal{M}$ . The outcomes of measurements allow to reconstruct the trajectory  $\gamma$  of  $\mathcal{S}$ . (Figure from [109])

This textbook situation allows us to understand generalized quantum measurements, pictured in Fig. 3.2: the system of interest  $\mathcal{S}$  weakly interacts with its environment  $\mathcal{E}$ , and the projective measurement is performed over  $\mathcal{E}$  [111]. Let the initial system state be  $|\psi\rangle$  and the state of the meter  $|\xi\rangle$ . The total state is then  $|\Psi\rangle = |\xi\rangle|\psi\rangle$ . After being coupled,  $\mathcal{S}$  and  $\mathcal{E}$  evolve under an operator  $U$ , the total state after the coupling writing  $|\Psi'\rangle = U|\xi\rangle|\psi\rangle$ . In general case this state can not be factorized.

As the measurement is performed only on  $\mathcal{E}$ , the projection operators act only in meter's Hilbert space:  $\Pi_\mu = \mathbb{1} \otimes \pi_\mu$ . The state of the system, after the outcome  $m_\mu$  was measured, writes

$$|\psi_\mu\rangle = \frac{\langle m_\mu|U|\xi\rangle|\psi\rangle}{\sqrt{P_\mu(t)}} = \frac{M_\mu|\psi\rangle}{\sqrt{P_\mu(t)}},$$

where the set of operators  $M_\mu = \langle m_\mu|U|\xi\rangle$ , that act in system's Hilbert space, is called the POVM, and the outcome probability writes  $P_\mu = \langle\psi|M_\mu^\dagger M_\mu|\psi\rangle$ . The conservation of probability creates a condition on the POVMs:

$$\sum_\mu M_\mu^\dagger M_\mu = \mathbb{1}.$$

Note, that  $|\psi_\mu\rangle$  are not necessarily orthogonal between each other, and in general case they do not form a basis.

The trajectory  $\gamma$  in this case is defined analogously to the previous one: a sequence of quantum states of  $\mathcal{S}$ , defined by the outcomes of the measurements over the meter  $\{m_\mu^\gamma(t_n)\}$  at times  $\{t_n\}_{1 \leq n \leq N}$  and the unitary evolution between these times.

If the measurement is unread, or in average over multiple trajectories, the state of the system is described by a density matrix

$$\bar{\rho}(t) = \sum_\mu M_\mu|\psi(t)\rangle\langle\psi(t)|M_\mu^\dagger = \sum_\mu P_\mu(t)|\psi_\mu(t)\rangle\langle\psi_\mu(t)| \quad (3.3)$$

Unlike the case of the strong measurements, in general case the coherences of the density matrix  $\bar{\rho}$  are not destroyed immediately after a measurement, as  $|\psi_\mu(t)\rangle$  may not be orthogonal between each other. Let's express the density matrix in a basis  $\{|\psi_k\rangle\}_{1 \leq k \leq d}$ , defined in the  $\mathcal{S}$  Hilbert space. After the coupling with the environment we can represent the joint state of  $\mathcal{S}$  and  $\mathcal{E}$  as a superposition  $U|\xi\rangle|\psi\rangle = \sum_k |\xi_k\rangle|\psi_k\rangle$ , where  $\{|\xi_k\rangle\}_{1 \leq k \leq d}$  do not necessarily form a basis. Thus,  $M_\mu|\psi\rangle = \sum_k \langle m_\mu|\xi_k\rangle|\psi_k\rangle$ , and the density matrix  $\bar{\rho}$ , expressed in a basis  $\{|\psi_k\rangle\}_{1 \leq k \leq d}$  writes

$$\bar{\rho} = \sum_{k,l} \langle \xi_l|\xi_k\rangle |\psi_k\rangle\langle\psi_l|.$$

The non-diagonal elements vanish only if the set  $\{|\xi_k\rangle\}_{1 \leq k \leq d}$  consists of orthogonal vectors.



### 3.1.2 Spin-dependent polarization rotation

Let us now illustrate this case with an example of a single electron or hole spin as a system  $\mathcal{S}$  and the polarized electromagnetic field as meter  $\mathcal{E}$ . The spin can have two possible projections on the quantization axis, and hence can be in one of the two states: up  $|\uparrow\rangle$  and down  $|\downarrow\rangle$ . The electromagnetic field is initially in a state  $|\psi\rangle$ . After an interaction with a spin in the state  $|\uparrow(\downarrow)\rangle$ , it is scattered in the polarization state  $|\psi_{\uparrow(\downarrow)}\rangle$  (we will describe the details of this process later):

$$\begin{aligned} |\psi\rangle|\uparrow\rangle &\rightarrow |\psi_{\uparrow}, \uparrow\rangle \\ |\psi\rangle|\downarrow\rangle &\rightarrow |\psi_{\downarrow}, \downarrow\rangle \end{aligned} \quad (3.4)$$

In an experiment this means that the polarization of the scattered light deviates from the incident light polarization. Hence the emitted light is a quantum meter  $\mathcal{M}$ : the correlation between the emitted light state and the state of the spin allows the spin state readout. Observation of scattered light in a polarization state  $|\psi_{\uparrow(\downarrow)}\rangle$  will indicate that the state of the spin is  $|\uparrow(\downarrow)\rangle$ . If these states of reflected light are orthogonal, the measurement satisfies the condition of quantum non-demolition [112], as the final state of the system is defined by the output of the measurement and the repeated measurement will give the same result:

$$|\psi\rangle|\uparrow\rangle \rightarrow |\psi_{\uparrow}, \uparrow\rangle \rightarrow \langle\psi_{\uparrow}|\psi_{\uparrow}, \uparrow\rangle = |\uparrow\rangle$$

and the probability to measure the 'wrong' state of light  $|\langle\psi_{\downarrow}|\psi_{\uparrow}, \uparrow\rangle|^2 = 0$ .

If the spin is initially in the superposition state of  $|\uparrow\rangle$  and  $|\downarrow\rangle$ ,

$$|\psi_{spin}\rangle = (C_{\uparrow}|\uparrow\rangle + C_{\downarrow}|\downarrow\rangle),$$

the interaction with the light creates an entangled state:

$$|\psi\rangle|\psi_{spin}\rangle \rightarrow |\Psi\rangle = C_{\uparrow}|\psi_{\uparrow}, \uparrow\rangle + C_{\downarrow}|\psi_{\downarrow}, \downarrow\rangle \quad (3.5)$$

We assume that the measured polarization of light is  $|\psi_{\uparrow}\rangle$ . The probability of such an event is

$$|\langle\psi_{\uparrow}|\Psi\rangle|^2 = |C_{\uparrow}|^2 + |\langle\psi_{\uparrow}|\psi_{\downarrow}\rangle|^2 |C_{\downarrow}|^2 \quad (3.6)$$

The total state of the system is projected onto the measured state:

$$\langle\psi_{\uparrow}|\Psi\rangle = C_{\uparrow}|\uparrow\rangle + \langle\psi_{\uparrow}|\psi_{\downarrow}\rangle C_{\downarrow}|\downarrow\rangle \quad (3.7)$$

In the general case this state is not the same as the initial one: this change of the state due to the measurement is called the back-action. The value of  $\langle\psi_{\uparrow}|\psi_{\downarrow}\rangle$  defines the strength of the measurement: if  $\langle\psi_{\uparrow}|\psi_{\downarrow}\rangle = 1$ , there is no impact on the spin's state, while if  $\langle\psi_{\uparrow}|\psi_{\downarrow}\rangle = 0$ , the measurement is projective.

Having stored the results of the measurement on the field, we can track the evolution of the spin, if the initial state is known. And knowing the back-action we can as well use the measurement to control the state of the spin.

### 3.1.3 System under study

One of the strategies to realize the spin readout is the spin-dependent rotation of polarization of light, incident on the spin [113–115], referred as Faraday rotation if transmitted light polarization is measured, and Kerr rotation for the reflected light. The polarization rotation can possibly reach any value [116]. In practice, the reported values of Faraday/Kerr rotation are  $3^\circ$  [117],  $6^\circ$  [116] and are reaching up to  $120^\circ$  [118].

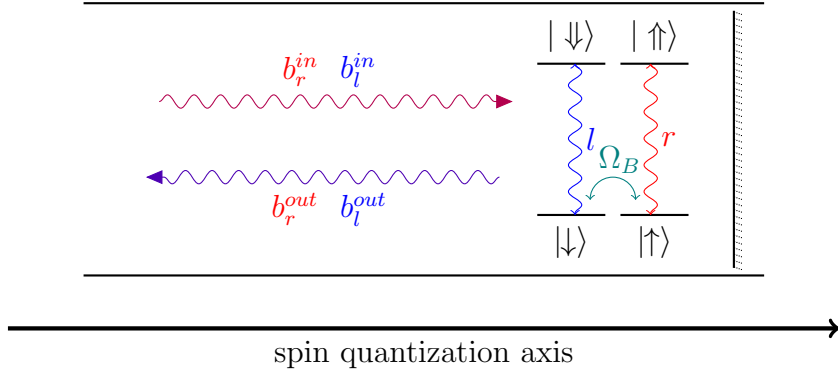


Figure 3.3: A 1D atom: a QD, doped with an electron, in an ideal wave-guide with a perfect mirror in a magnetic field.

In the chapter we will focus on a case of a spin of an electron doped in a semiconductor quantum dot (QD), coupled to a one-dimensional environment, divided by a perfect mirror (Fig. 3.3), that we label as 1D atom. The quantization of the projection of the spin (in the following we call it 'the spin state') is along this unidimensional environment: the 'up' states signify the spin projection along the incident light propagation, and 'down' - in the opposite direction.

The scheme of a QD excitation is presented in Fig. 3.4. The initial state of the QD is a state of the spin of a doped electron in a conduction band. For the sake of simplicity we assume that the state is 'up',  $|\uparrow\rangle$ , so the spin projection is  $S_e = 1/2$ . The incident polarized light in general case can be expressed in the basis of the two circular polarizations: the right with the helicity of  $S_l = +1$  and the left with the helicity of  $S_l = -1$ . If the right-polarized photon is absorbed by the QD, the electron-heavy hole pair is created [60].

The electron in this pair has the same energy as the initially embedded electron. Due to the Pauli principle, they can not be in the same state, so there must be difference in the only degree of freedom left: the projection of the spin onto the quantization axis. The new electron thus must have  $S_e = -1/2$ . The total orbital momentum of the two electrons is thus always zero.

The spin of a heavy hole is  $3/2$ , and the orbital momentum conservation allows only spin-up trion:

$$S_t = S_e + S_l = +1/2 + 1 = +3/2$$

For the same reason the spin-up trion can decay only into the spin-up electron and

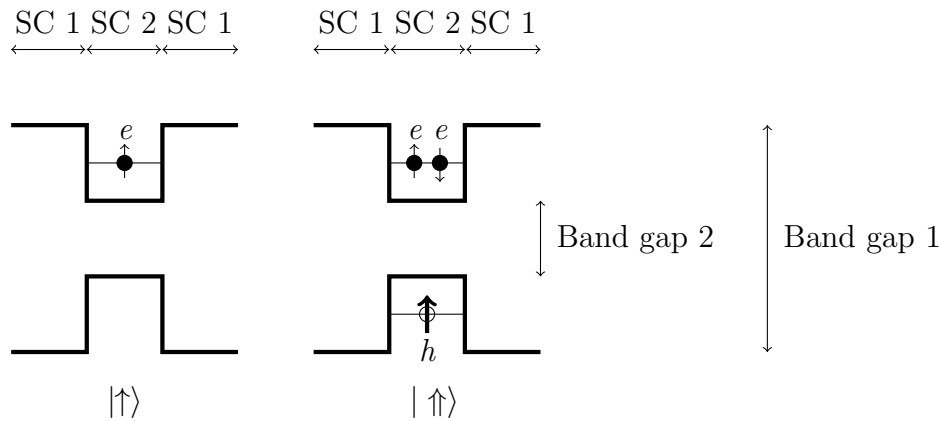


Figure 3.4: Scheme of the levels of QD, doped with an electron. For simplicity we assume that the electron is initialized with a spin-up state. Left plane: the ground state  $|\uparrow\rangle$  corresponds to the spin-up electron in the conduction band. Right plane: the excited state  $|\uparrow\uparrow\rangle$  corresponds to the creation of an electron-hole pair after absorption of a right circularly polarized photon, the resulting quasi-particle being the trion.

the right polarized photon. Similarly, for the initial spin-down electron:

$$S_t = S_e + S_l = -1/2 - 1 = -3/2$$

The same laws forbid interaction of the spin-up (spin-down) electron and the left (right) polarized light.

The electron-trion transition is saturated by a single photon, so the power of the incident light has an enormous impact on the efficiency of the light as a meter. Let us consider a simple case: the initial state of the spin is up, and the polarization of the incident light is circular right. It is equivalent to the case of a neutral two-level system. The light field, if its power is much lower than the saturation value, will be absorbed by the system and then re-emitted with the opposite phase:

$$|r\rangle|\uparrow\rangle \rightarrow -|r\rangle|\uparrow\rangle \quad (3.8)$$

If the spin is down, the right-polarized field will be reflected from the mirror, keeping the same phase. If the spin is in the superposition state of  $|\uparrow\rangle$  and  $|\downarrow\rangle$ , the reflected and re-emitted components will have different phases and destructively interfere, reducing the power of the right-polarized light. Now, if the incident light polarization has both right and left polarized components, the respective amount of each of them will be changed differently, thus rotating the polarization.

In total, there are four parameters that define the ability to measure the state of the electron spin in the QD:

- the strength of the light-matter coupling
- the amount of losses
- the power of the incident laser

- the set of measured polarizations

Here the first two characterize the system under study as a 1D atom, and the last two are characteristics of incident and reflected light as a meter.

The measurement allows not only to acquire information on the state of the spin, but also to prepare a given state through measurement back-action. To increase the number of possible spin states that can be prepared, we include into consideration the magnetic field, perpendicular to the unidimensional wave guide, the set-up known as the Voigt configuration [60]. The measurement prepares the spin (anti-)parallel with the guide, and then it precesses around the magnetic field axis [115, 119], until it reaches the state the experimentalist wants. Throughout the chapter we will use two regimes: with and without the magnetic field, indicating which case we are considering in each section.

### 3.1.4 Outline of the chapter

The objective of the chapter is to describe a measurement of the spin state with the light field and its back-action. The chapter is organized as follows. In the Section 3.2 we present the model of the system under study. The Bloch equations are solved to describe the dynamics of the spin in presence of the electromagnetic field, focusing on the coherences between the spin states. In the Section 3.3 we study the rotation of the polarization of light, in order to characterize it as a quantum meter. Both of these sections investigate the case of unread measurements, while the next ones represent the read measurements. In the Section 3.4 we study the back-action of the measurement on the spin, giving rise to quantum trajectories. In this section we are focusing on the case with the most optimal conditions for the spin state measurement, that allow to observe the freezing of the spin evolution due to Quantum Zeno effect. The Section 3.5 is dedicated to different imperfections of the set-up.

## 3.2 Bloch equations for the spin

### 3.2.1 Model of the system

The model of the system under study is shown in Fig. 3.3. The polarization of the incident laser light is represented in the basis of right ( $r$ ) and left ( $l$ ) circular polarizations with the amplitudes  $b_r^{in}$  and  $b_l^{in}$ . The same representation holds for the reflected light:  $b_r^{out}$  and  $b_l^{out}$  for the right and left circular polarizations respectively.

The QD can be in one of the four states: in the two ground states it contains only an electron, which can have two possible spin states along the cavity axis  $|\uparrow(\downarrow)\rangle$ . The excited state, a trion, consists of two electrons with different spin states and a heavy hole. The trion states are labelled as  $|\uparrow\downarrow(\downarrow)\rangle$ .

This natural separation of states with different spin states can be represented as

$$\rho := \left( \begin{array}{cc|cc} \rho_{\uparrow\uparrow} & \rho_{\uparrow\downarrow} & \rho_{\uparrow\uparrow} & \rho_{\uparrow\downarrow} \\ \rho_{\uparrow\downarrow} & \rho_{\uparrow\downarrow} & \rho_{\uparrow\downarrow} & \rho_{\uparrow\downarrow} \\ \hline \rho_{\downarrow\uparrow} & \rho_{\downarrow\uparrow} & \rho_{\downarrow\uparrow} & \rho_{\downarrow\uparrow} \\ \rho_{\downarrow\downarrow} & \rho_{\downarrow\downarrow} & \rho_{\downarrow\downarrow} & \rho_{\downarrow\downarrow} \end{array} \right) := \left( \begin{array}{c|c} \hat{\rho}_{rr} & \hat{\rho}_{rl} \\ \hline \hat{\rho}_{lr} & \hat{\rho}_{ll} \end{array} \right) \quad (3.9)$$

One can define the probability for the spin to be in the ‘‘up’’ (‘‘down’’) state, that interacts with right (left) polarized light  $P_{r(l)}$  as well as the spin polarization along the wave guide  $S_z$  expressed as their difference:

$$P_r = \rho_{\uparrow\uparrow} + \rho_{\downarrow\downarrow} \quad (3.10a)$$

$$P_l = \rho_{\downarrow\downarrow} + \rho_{\uparrow\uparrow} \quad (3.10b)$$

$$S_z = P_r - P_l \quad (3.10c)$$

Other figures of interest allow us to evaluate projections of the spin polarization on the other axes, expressed through the coherences between the two spin states:

$$S_x = 2 \operatorname{Re} (\rho_{\uparrow\downarrow} + \rho_{\downarrow\uparrow}) \quad (3.11a)$$

$$S_y = 2 \operatorname{Im} (\rho_{\uparrow\downarrow} + \rho_{\downarrow\uparrow}) \quad (3.11b)$$

The dynamics of the system is ruled by the master equation, where the unitary evolution is governed by the Hamiltonian  $H$ , and the spontaneous decay, induced by the interaction with the electromagnetic environment is represented by the operators

$$\sigma_r = |\uparrow\rangle\langle\uparrow|, \quad \sigma_l = |\downarrow\rangle\langle\downarrow| \quad (3.12)$$

The master equation, incorporating these components, writes

$$\frac{d}{dt}\rho = \mathcal{L}[\rho] = -i[H, \rho] + \gamma \sum_{j=r,l} \left( \sigma_j \rho \sigma_j^\dagger - \frac{1}{2} \sigma_j^\dagger \sigma_j \rho - \frac{1}{2} \rho \sigma_j^\dagger \sigma_j \right) \quad (3.13)$$

where  $\mathcal{L}$  is the Lindbladian and  $\hbar = 1$ .

In the following, for the sake of clarity and simplicity we neglect the pure dephasing of the trion states: it is a realistic assumption for semiconductor QDs in micropillar cavities [28, 40]. We also neglect both the decay and the decoherence of the spin, which is a valid assumption for most of the implementations [37, 98–100].

The total Hamiltonian in the frame, rotating at laser frequency  $\omega_l$ , is:

$$H = H_r + H_l \quad (3.14a)$$

$$H_j = (\omega_j - \omega_l) \sigma_j^\dagger \sigma_j + i\sqrt{\eta\gamma} \left( (b_j^{in})^* \sigma_j - \sigma_j^\dagger b_j^{in} \right), \quad j = \{r, l\} \quad (3.14b)$$

where  $\gamma$  is a decay rate of the trions,  $b_{r(l)}^{in}$  are the amplitudes of the incident light fields in each circular polarization and  $\eta$  represents the imperfections of the coupling between the QD and the field:  $\eta = 1$  means that all the incident photons can interact with the QD, and all the scattered photons will be directed towards the detectors. Decreasing of this parameter indicates emission out of the guide, and spatial non-matching between incident light and the QD. The drive assumed to be continuous and in resonance with the electron-trion transitions:  $\omega_r = \omega_l = \omega_l$ .

### 3.2.2 Dynamics of the populations

Let us now examine the dynamics of the spin, if there is no magnetic field. In this case the spin-up and spin-down subsystems are uncoupled, and behave like a separate two-level systems. The equations of motion can be separated into 4 groups as in (3.9):

$$\frac{d}{dt}\rho = \begin{pmatrix} \mathcal{L}[\hat{\rho}_{rr}] & \mathcal{L}[\hat{\rho}_{rl}] \\ \mathcal{L}[\hat{\rho}_{lr}] & \mathcal{L}[\hat{\rho}_{ll}] \end{pmatrix} \quad (3.15)$$

The spin polarization  $S_z$  is a “good quantum number”: it remains stable under interaction with light, guaranteeing the QND nature of the measurement as we show below.

More precisely, the diagonal sub-matrices of the matrix (3.9) are analogous to the description of two non-interacting two-level systems, each excited by a resonant laser. We can introduce Hilbert subspaces  $\mathcal{H}_\uparrow$  and  $\mathcal{H}_\downarrow$  for each of these two-level systems:  $|\uparrow\rangle, |\uparrow\rangle \in \mathcal{H}_\uparrow$  and  $|\downarrow\rangle, |\downarrow\rangle \in \mathcal{H}_\downarrow$ . The total space is a linear combination of  $\mathcal{H}_\uparrow$  and  $\mathcal{H}_\downarrow$ . The master equation (3.13) for the sub-matrices  $\hat{\rho}_{jj}$  can be represented in Bloch form as

$$\frac{d}{dt}\langle\sigma_j\rangle = -\frac{\gamma}{2}\langle\sigma_j\rangle + \sqrt{\eta\gamma}b_j^{in}\langle\sigma_j^z\rangle, \quad j = r, l \quad (3.16a)$$

$$\frac{d}{dt}\langle\sigma_j^z\rangle = -\gamma(P_j + \langle\sigma_j^z\rangle) - 2\sqrt{\eta\gamma}((b_j^{in})^*\langle\sigma_j\rangle + b_j^{in}\langle\sigma_j\rangle^*), \quad j = r, l \quad (3.16b)$$

where  $\sigma_r^z = |\uparrow\rangle\langle\uparrow| - |\downarrow\rangle\langle\downarrow|$  and  $\sigma_l^z = |\downarrow\rangle\langle\downarrow| - |\uparrow\rangle\langle\uparrow|$ , and  $P_{r(l)}$  is a probability to find a spin in the up(down) state, defined in (3.10). Both  $P_j$  are constants.

The solutions of the equations (3.16) are shown in Fig. 3.5 for the initial state  $(|\uparrow\rangle + |\downarrow\rangle)/\sqrt{2}$ , horizontally polarized light  $|b_r^{in}|^2 = |b_l^{in}|^2 = |b_l^{in}|^2$  and perfect light-matter coupling  $\eta = 1$ . The Fig. 3.5a shows that the subsystem in  $\mathcal{H}_\uparrow$  behaves the same way as a two-level system under continuous excitation, the only difference being that the values on the vertical axis are bound by  $\pm P_r$ . The total behaviour of the spin is presented in Fig. 3.5b. The spin polarization  $S_z$  does not change as there are no forces to rotate or flip the spin. The real part of the coherence between the spin states  $S_x$  is decaying due to the interaction with light, and in the next subsection we shall consider this decay in detail.

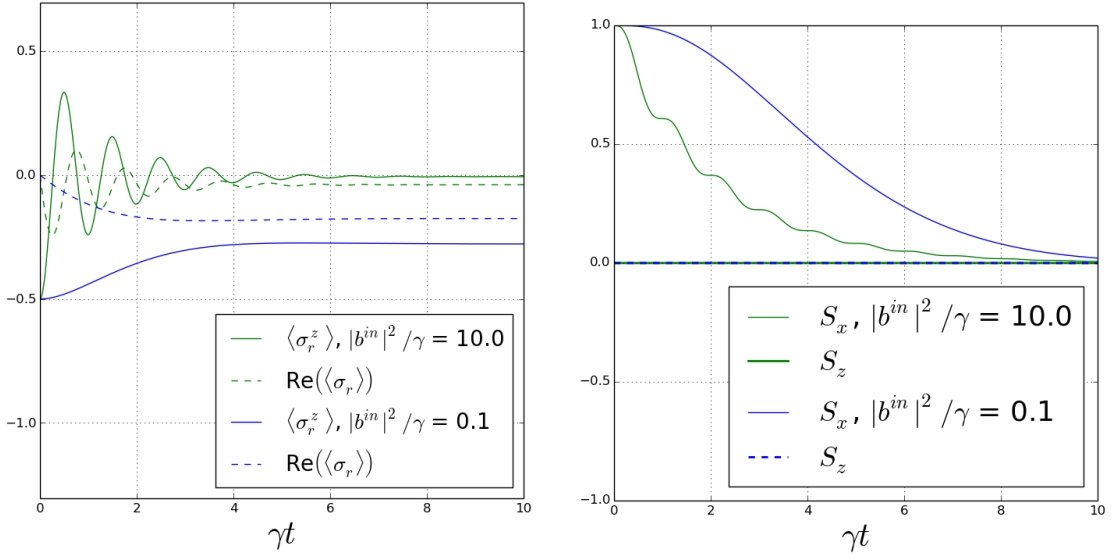
### 3.2.3 Coherences between different spin states

We now turn to the analysis of the dynamics of the coherences between the spin-up and the spin-down states, showing that the laser pumping induces loss of coherence between the spin states.

The non-diagonal sub-matrices of the spin density matrix (3.9) evolve according to

$$\frac{d}{dt}\rho_{\uparrow\downarrow} = \sqrt{\eta\gamma}(b_r^{in}\rho_{\uparrow\downarrow} + (b_l^{in})^*\rho_{\uparrow\downarrow}) \quad (3.17a)$$

$$\frac{d}{dt}\rho_{\uparrow\downarrow} = -\gamma\rho_{\uparrow\downarrow} - \sqrt{\eta\gamma}((b_r^{in})^*\rho_{\uparrow\downarrow} + b_l^{in}\rho_{\uparrow\downarrow}) \quad (3.17b)$$



(a) Evolution of the spin-up subsystem in the spin Hilbert space  $\mathcal{H}_\uparrow$ : damped Rabi oscillations for the high power and rise until saturation for low power. The spin-down subsystem behaves in exactly the same way. (b) Evolution of the spin. The spin polarization remains constant due to the absence of coupling between the spin states. The coherences between the spin states exponentially decrease due to the environment-induced dephasing, with higher dephasing rate for higher power.

Figure 3.5: The dynamics of the QD doped with an electron without magnetic field. The initial state is  $(|\uparrow\rangle + |\downarrow\rangle)/\sqrt{2}$ ,  $\eta = 1$ , the light polarization is horizontal:  $|b^{in}|^2 = |b_r^{in}|^2 = |b_l^{in}|^2$ .

$$\frac{d}{dt}\rho_{\uparrow\downarrow} = -\frac{\gamma}{2}\rho_{\uparrow\downarrow} - \sqrt{\eta\gamma}(-b_r^{in}\rho_{\uparrow\downarrow} + b_l^{in}\rho_{\uparrow\downarrow}) \quad (3.17c)$$

$$\frac{d}{dt}\rho_{\uparrow\downarrow} = -\frac{\gamma}{2}\rho_{\uparrow\downarrow} - \sqrt{\eta\gamma}((b_r^{in})^*\rho_{\uparrow\downarrow} - (b_l^{in})^*\rho_{\uparrow\downarrow}) \quad (3.17d)$$

This is a system of four ordinary first order linear differential equations. The solutions are linear combinations of complex exponentials:

$$\rho_{\alpha\beta} = \sum_{k=1}^4 c_k^{\alpha\beta} \exp(\lambda_k t); \alpha \in \{\uparrow, \uparrow\}, \beta \in \{\downarrow, \downarrow\} \quad (3.18a)$$

$$\lambda_{1,2,3,4} = -\frac{\gamma}{2} \pm \frac{1}{2}\sqrt{\frac{\gamma^2}{4} - 4\eta\gamma|b_r^{in}|^2} \pm \frac{1}{2}\sqrt{\frac{\gamma^2}{4} - 4\eta\gamma|b_l^{in}|^2} \quad (3.18b)$$

The solutions are shown in Fig. 3.5b.

Let us introduce the effective dephasing rate as the slowest decay rate of the coherences:

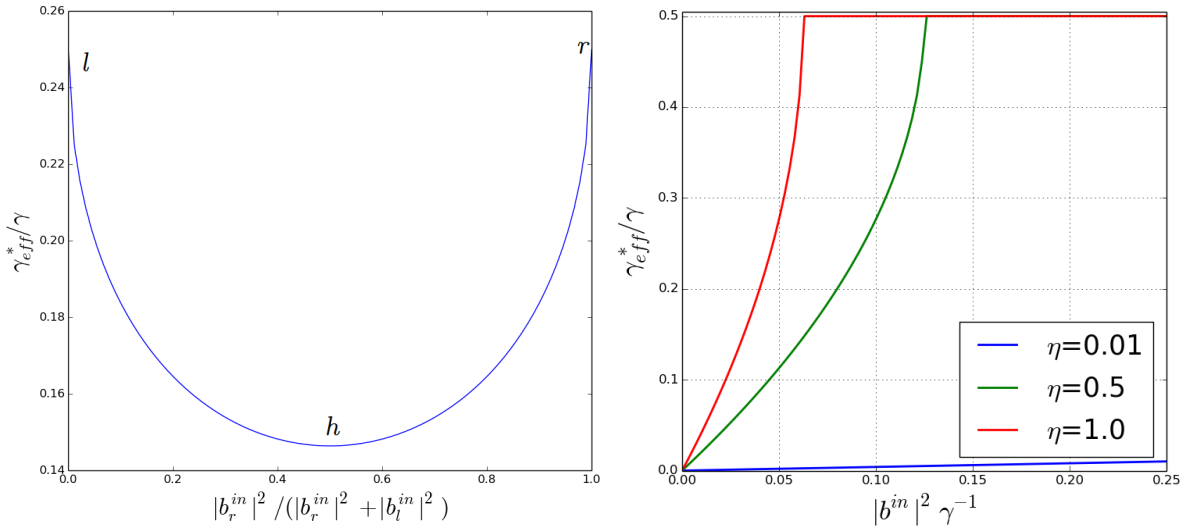
$$\gamma_{eff}^* = -\inf(\{\text{Re}(\lambda_k)\}) \quad (3.19)$$

The horizontally polarized pump,  $|b_l^{in}|^2 = |b_r^{in}|^2 = |b^{in}|^2$ , maximizes the effective

dephasing rate, as is shown in Fig. 3.6a. For this case:

$$\gamma_{eff}^* = \begin{cases} \gamma/2, & \text{if } 16\eta |b^{in}|^2 > \gamma \\ \gamma/2 \left( 1 - \sqrt{1 - 16\eta |b^{in}|^2 / \gamma} \right), & \text{otherwise} \end{cases} \quad (3.20)$$

This behaviour of  $\gamma_{eff}^*$  as the function of power is shown in Fig. 3.6b.



(a) Effective dephasing rate  $\gamma_{eff}^*$  as a function of polarization (expressed here as ratio of the  $r$  component of power of the horizontally polarized component) for  $\eta (|b_r^{in}|^2 + |b_l^{in}|^2) = \gamma/16$ . (b) Effective dephasing rate  $\gamma_{eff}^*$  as a function of power of the horizontally polarized pump.

Figure 3.6: Behavior of the effective dephasing rate  $\gamma_{eff}^*$ .

The difference in relaxation rates of spin coherences in Eq. (3.20) for different powers can be seen as a signature of two different mechanisms of light-matter interaction - two mechanisms of spin readout. For the high powers beyond saturation (the upper part of Eq. (3.20)) the system emits photons due to spontaneous emission. Such light has no phase, and hence it can not interfere with the incident field, this corresponds to incoherent scattering. The spontaneous emission rate is defined only by  $\gamma$ , and so is the effective dephasing in the high-power regime.

If the pump power is much lower than the spontaneous emission rate, the electron-trion transition is not saturated. The emitted light is coherent with the incident one and the effective dephasing rate is proportional to the incident power:

$$\gamma_{eff}^* \approx 2\eta \left( |b_r^{in}|^2 + |b_l^{in}|^2 \right), \text{ if } \eta |b_i^{in}|^2 \ll \gamma \quad (3.21)$$

The  $\gamma$  is not present in this equation because of the difference of the time scales: the decay happens almost instantaneously, so the only important rate is the rate at which the trion is excited.



### 3.2.4 Behaviour in the magnetic field

To illustrate the effective dephasing, let us consider the behaviour of the system in the magnetic field, orthogonal to the wave-guide axis. The Hamiltonian changes in the following way [120]:

$$H' = H + H_B \quad (3.22a)$$

$$H_B = \frac{\Omega_B}{2} (|\uparrow\rangle\langle\downarrow| + |\downarrow\rangle\langle\uparrow|) \quad (3.22b)$$

where only the electrons are affected by the field, and  $\Omega_B$  is the so-called Larmor frequency, proportional to the magnetic field magnitude and to the spin-dependent g-factor. Its value for heavy holes is much smaller than for electrons [121], so the interaction of trions with magnetic field can be neglected.

Now the subspaces  $\mathcal{H}_\uparrow$  and  $\mathcal{H}_\downarrow$  are coupled by the magnetic field, and the density matrix  $\rho$  can not be separated into independent matrices. The Bloch equations for the complete four-level system write:

$$\frac{d}{dt}\langle\sigma_r\rangle = -\frac{\gamma}{2}\langle\sigma_r\rangle + \sqrt{\eta\gamma}b_r^{in}\langle s_r^z\rangle + i\frac{\Omega_B}{2}\rho_{\downarrow\uparrow} \quad (3.23a)$$

$$\frac{d}{dt}\langle\sigma_l\rangle = -\frac{\gamma}{2}\langle\sigma_l\rangle + \sqrt{\eta\gamma}b_l^{in}\langle s_l^z\rangle + i\frac{\Omega_B}{2}\rho_{\uparrow\downarrow} \quad (3.23b)$$

$$\frac{d}{dt}\langle s_j^z\rangle = -\gamma(P_j + \langle s_j^z\rangle) - 2\sqrt{\eta\gamma}\left((b_j^{in})^*\langle\sigma_j\rangle + b_j^{in}\langle\sigma_j^\dagger\rangle\right) \pm i\frac{\Omega_B}{2}(\rho_{\downarrow\uparrow} - \rho_{\uparrow\downarrow}) \quad (3.23c)$$

$$\frac{d}{dt}\rho_{\uparrow\downarrow} = \sqrt{\eta\gamma}(b_r^{in}\rho_{\uparrow\downarrow} + (b_l^{in})^*\rho_{\uparrow\downarrow}) + i\frac{\Omega_B}{2}(\rho_{\downarrow\downarrow} - \rho_{\uparrow\uparrow}) \quad (3.23d)$$

$$\frac{d}{dt}\rho_{\uparrow\downarrow} = -\gamma\rho_{\uparrow\downarrow} - \sqrt{\eta\gamma}\left((b_r^{in})^*\rho_{\uparrow\downarrow} + b_l^{in}\rho_{\uparrow\downarrow}\right) \quad (3.23e)$$

$$\frac{d}{dt}\rho_{\uparrow\downarrow} = -\frac{\gamma}{2}\rho_{\uparrow\downarrow} - \sqrt{\eta\gamma}\left(-b_r^{in}\rho_{\uparrow\downarrow} + b_l^{in}\rho_{\uparrow\downarrow}\right) + i\frac{\Omega_B}{2}\langle\sigma_l\rangle \quad (3.23f)$$

$$\frac{d}{dt}\rho_{\uparrow\downarrow} = -\frac{\gamma}{2}\rho_{\uparrow\downarrow} - \sqrt{\eta\gamma}\left((b_r^{in})^*\rho_{\uparrow\downarrow} - (b_l^{in})^*\rho_{\uparrow\downarrow}\right) - i\frac{\Omega_B}{2}\langle\sigma_r^\dagger\rangle \quad (3.23g)$$

and the complex conjugated of the last four equations. The plus sign in Eq. (3.23c) corresponds to  $l$ .

#### Zeno effect

The solutions of the Eq. (3.23) are shown in Fig. 3.7 for different values of the pump power as the time dependence of the spin polarization:

$$S_z = P_r - P_l$$

The dark blue curve corresponds to the low pump power, and as the dephasing, described in the previous section, is also negligible in this case, this curve has maximal amplitude. The green curve corresponds to higher power, and shows how the amplitude of the oscillations decreases. For the red curve the pump makes the value of the effective dephasing high enough for the oscillations to disappear at all,

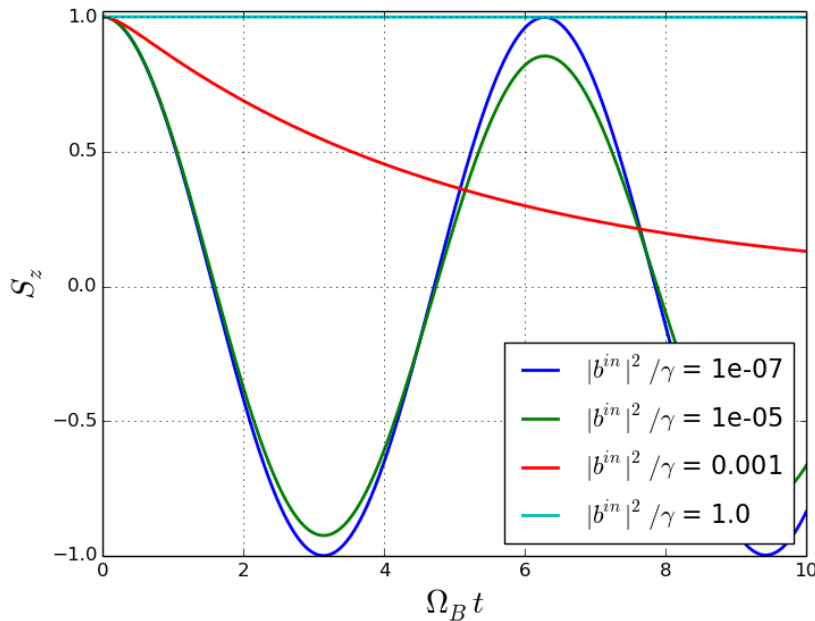


Figure 3.7: Spin oscillations in magnetic field of  $\Omega_B = 10^{-4}\gamma$ . Pump is horizontally polarized,  $\eta = 0.5$ . The initial state is  $|\uparrow\rangle$ .

but the magnetic field still can rotate spin, and the total state relaxes towards the statistical mixture of up and down states.

The cyan curve represents the case when the pump power is large enough to freeze the oscillations. Interestingly, the spin polarization  $S_z \rightarrow 0$ , but instead  $S_z(t) = 1 \forall t \ll |b^{in}|^{-2}$ , though it is reached with a dissipative process. It can be seen as an evidence of the Quantum Zeno effect (QZE): higher power of the pump ensures that the photons interact with the system more frequently. These events can be seen as measurements of the spin state (even if there is no detector, the environment i.e. the electromagnetic field is the one who measures). And if these measurements are frequent enough, the spin is frozen in its initial state. The condition to reach Zeno regime can be formulated as

$$\Omega_B \ll 16\eta|b^{in}|^2$$

In this section it was shown that if the system is pumped, it induces a relaxation of the coherences between spin-up and spin-down states. As will be explained below, it can be interpreted as an effect of the measurement of the spin by the electromagnetic field, and the coherent or incoherent nature of the light-matter interaction is reflected in the effective dephasing rate of this process. This effect can be used in the Zeno regime to freeze the precession of the spin in a magnetic field, which is a signature of a projective measurement. In the following section we'll characterize polarized light as a meter.

### 3.3 Light polarization as a quantum meter

#### 3.3.1 Semi-classical model

While the dynamics of the spin is well described by Eq. (3.13) and (3.14), we now focus on the properties of the light field. The scattered light is described with semiclassical input-output formalism [58], where the scattered field operators are constructed from two contributions: the field, reflected from the mirror and the field, scattered on the spin.

$$b_j^{out} = \mathbb{1}b_j^{in} + \sqrt{\eta\gamma}\sigma_j, \quad j = r, l \quad (3.24)$$

The dimension of the operator is a square root of number of photons per unit time.

Any polarization can be represented with these operators, for example, the operators for the horizontal and vertical  $\{h, v\}$  and antidiagonal and diagonal  $\{a, d\}$  write:

$$b_h^{out} = \frac{1}{\sqrt{2}}(b_r^{out} + b_l^{out}) \quad (3.25a)$$

$$b_v^{out} = \frac{i}{\sqrt{2}}(b_r^{out} - b_l^{out}) \quad (3.25b)$$

$$b_d^{out} = \frac{1}{\sqrt{2}}(b_h^{out} + b_v^{out}) \quad (3.25c)$$

$$b_a^{out} = \frac{1}{\sqrt{2}}(b_h^{out} - b_v^{out}) \quad (3.25d)$$

The observables we are interested in are the intensities of the light field, scattered by the QD per unit time in each of these polarizations:

$$I_i = \langle (b_i^{out})^\dagger b_i^{out} \rangle, \quad i = r, l, h, v, d, a \quad (3.26)$$

We shall use the Poincaré sphere to graphically represent light polarizations as vectors. The axes on the sphere represent the sets of orthogonal polarization bases: right and left  $\{r, l\}$  on the poles, and the pairs horizontal and vertical  $\{h, v\}$  with antidiagonal and diagonal  $\{a, d\}$  on the equator. Any vector  $\vec{\varepsilon}$  that characterizes light polarization starts in the centre of the sphere, and the point on the top is given by three coordinates

$$s_{ij} = \frac{I_i - I_j}{I_i + I_j} \quad (3.27)$$

for  $\{i, j\} = \{r, l\}, \{h, v\}$  and  $\{a, d\}$ :

$$\vec{\varepsilon} = (s_{rl}, s_{hv}, s_{ad})$$

The length of the vector corresponds to the degree of polarization, that is equal to  $|\vec{\varepsilon}| = \sqrt{s_{rl}^2 + s_{hv}^2 + s_{ad}^2}$  and describes the ability of differently polarized components of the light to interfere between each other. The value  $|\vec{\varepsilon}| = 1$  corresponds to maximally polarized light, while  $|\vec{\varepsilon}| = 0$  - to the non-polarized. The latter case can be illustrated with an example of two light fields of the same intensity, but with

different polarizations,  $r$  and  $l$ , and different frequencies: due to the absence of the spectral overlap they do not interfere, and thus can not form  $h$  or  $v$  light, as would be the case for two fields with the same frequency.

Experimentally, the polarization tomography technique can be used to represent the state of the scattered light polarization on the Poincaré sphere [122].

### 3.3.2 Quantum meter

To quantify the spin-dependent polarization rotation let us introduce the polarization vectors that correspond to the spin-up and spin-down states  $\vec{\varepsilon}_{\uparrow(\downarrow)}$  and the incident light polarization  $\vec{\varepsilon}_0$ . Symbolically we can rewrite the table (3.4) as

$$\begin{aligned} \vec{\varepsilon}_0 &\xrightarrow{\text{spin in } |\uparrow\rangle} \vec{\varepsilon}_{\uparrow} \\ \vec{\varepsilon}_0 &\xrightarrow{\text{spin in } |\downarrow\rangle} \vec{\varepsilon}_{\downarrow} \end{aligned} \quad (3.28)$$

In general case, these two polarizations are not orthogonal to each other. We also introduce the polarizations that are orthogonal to  $\vec{\varepsilon}_{\uparrow(\downarrow)}$  as  $\vec{\varepsilon}_{\uparrow(\downarrow)\perp}$ .

We also introduce the distinguishability  $D$  to quantify the ability to correctly identify the spin state from the measured polarization of the scattered light. It is constructed in such a way, that it reaches the minimal value of  $D = 0$  if the polarizations of scattered light for different spin states coincide,  $\vec{\varepsilon}_{\uparrow} \cdot \vec{\varepsilon}_{\downarrow} = 1$ , where  $\cdot$  is for scalar product of vectors. If the light is unpolarized,  $|\vec{\varepsilon}_{\uparrow(\downarrow)}| = 0$ , it is also impossible to conclude about the spin state, hence  $D = 0$ . The maximal value of  $D = 1$  is found when the angle between polarizations is maximal. The maximally reached angle on the Poincaré sphere is  $\pi$ , hence  $\vec{\varepsilon}_{\uparrow} \cdot \vec{\varepsilon}_{\downarrow} = \cos(\pi) = -1$ . The total expression for the distinguishability writes:

$$D = |\vec{\varepsilon}_{\uparrow}| |\vec{\varepsilon}_{\downarrow}| \frac{(1 - \vec{\varepsilon}_{\uparrow} \cdot \vec{\varepsilon}_{\downarrow})}{2} \quad (3.29)$$

In the following we are looking for the maximal value of  $D$  for various conditions, studying the influence of the parameters that describe the meter and the system, and aiming to find their optimal combination to maximize  $D$ .

We restrict ourselves to the stationary state, defined as

$$\frac{d}{dt}\rho = 0 \quad (3.30)$$

and reached after a period of evolution that is much longer than the characteristic times of the system.

As for the incident light polarization, we consider only the case when the incident light is polarized horizontally:  $|b_l^{in}|^2 = |b_r^{in}|^2 := |b^{in}|^2$ . This allows to acquire the maximal amount of information from polarization-resolving measurement<sup>1</sup>: as the

<sup>1</sup>This holds only if the detectors at the output can resolve scattered light polarization. If this is not the case, the most optimal choice of incident light polarization would be either  $r$  or  $l$  and instead of measurement of spin-dependent polarization rotation, we would be interested in the spin-dependent reflectivity [123].

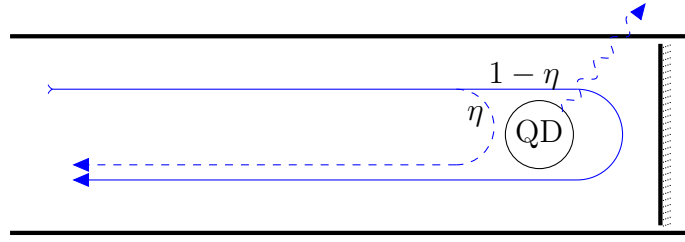


Figure 3.8: The fraction of light that interacts with the QD is  $\eta$ . This light is scattered with opposite phase or lost. The rest of the incident light is reflected from the mirror, keeping the initial phase. These two parts then interfere destructively.

spin-up states interact only with the  $r$  polarized light and the spin-down - with the  $l$  one, the polarization that has equal amount of both, probes both states of the spin. Any linear polarization fits this description. For the sake of simplicity we chose  $h$ .

### 3.3.3 Influence of the parameters

Let us first qualitatively consider the ideal case, where all the incident photons interact with the QD. It means perfect coupling between light and matter  $\eta = 1$  and the low incident light power  $|b^{in}|^2 \ll \gamma$ , so that the electron-trion transition is not saturated. If the spin is up, the  $r$  component of the pump is re-emitted with the phase of  $\pi$ , and the  $l$  component is reflected from the mirror without phase change. So, the polarization is changed from  $h$  to  $v$ . The similar situation happens, if the spin is down. Symbolically, we can write it as:

$$\begin{aligned} |h\rangle|\uparrow\rangle &\sim (|r\rangle + |l\rangle)|\uparrow\rangle \rightarrow (-|r\rangle + |l\rangle)|\uparrow\rangle \sim -|v\rangle|\uparrow\rangle \\ |h\rangle|\downarrow\rangle &\sim (|r\rangle + |l\rangle)|\downarrow\rangle \rightarrow (|r\rangle - |l\rangle)|\downarrow\rangle \sim |v\rangle|\downarrow\rangle \end{aligned} \quad (3.31)$$

These polarizations are not distinguishable with measurement of the scattered light intensities. Note also that the linear combination of these two equations demonstrates that  $h$  polarization is transformed into  $v$  independently on the spin state.

In general, we consider the possibility of  $\eta < 1$ , that means that not all the photons in the field interact with the QD, as in Fig. 3.8. In this case there will be a fraction of light  $1 - \eta$  that conserved its initial  $h$  polarization, and will interfere with the reflected light, polarized as  $\pm v$ . We also consider different power regimes.

Quantitatively this is described as follows. In the stationary state, the amplitudes and intensities of  $r$  and  $l$  light write

$$\langle b_i^{out} \rangle = b_i^{in} + \sqrt{\eta\gamma} \langle \sigma_i \rangle = b_i^{in} \left( 1 - \frac{2P_i\eta}{1 + \frac{8\eta}{\gamma}|b_i^{in}|^2} \right) \quad (3.32)$$

$$I_i = \langle (b_i^{out})^\dagger b_i^{out} \rangle = |b_i^{in}|^2 \left[ 1 - \frac{4(\eta - \eta^2)P_i}{1 + \frac{8\eta}{\gamma}|b_i^{in}|^2} \right], \quad i = r, l \quad (3.33)$$

And for the other polarizations:

$$I_h = 2|b^{in}|^2 \left[ 1 - \frac{\eta(2 - \eta)}{1 + \frac{8\eta}{\gamma}|b^{in}|^2} \right] \quad (3.34a)$$

$$I_v = 2|b^{in}|^2 \frac{\eta^2}{1 + \frac{8\eta}{\gamma}|b^{in}|^2} \quad (3.34b)$$

$$I_a = I_d = |b^{in}|^2 \left[ 1 - \frac{2\eta(1-\eta)}{1 + \frac{8\eta}{\gamma}|b^{in}|^2} \right] \quad (3.34c)$$

The intensities of light in circular polarizations  $I_r$  and  $I_l$  depend on the spin state, expressed through  $P_{r,l}$ :  $P_r = 1, P_l = 0$  for the spin-up case, and otherwise for the spin-down.

### The imperfections of light matter coupling

The Poincaré spheres with the polarizations of reflected light for different spin states  $\vec{\varepsilon}_{\uparrow(\downarrow)}$  are shown in Figs. 3.9 and 3.10 for different values of  $\eta$  and  $|b^{in}|^2$ . The incident light is  $h$ -polarized, and there is no magnetic field.

The case of the low pump power is considered in Fig. 3.9. The pump power is much lower than the saturation value, hence all input photons interact with the spin. Let us start with the ideal case of no losses:  $\eta = 1$ , Fig. 3.9a. It was described above with Eq. (3.31), and the polarizations of the scattered light are the same for both spin states. Hence,  $|\vec{\varepsilon}_{\uparrow} \cdot \vec{\varepsilon}_{\downarrow}|^2 = 1, D = 0$ , and there is no possibility to distinguish between the spin-up and spin-down states with only the light intensities measurement.

The limit case of  $\eta = 0$ , Fig. 3.9b, represents the absence of a spin. All the light is reflected from the mirror in the same polarization as the input one, so again  $D = 0$ .

The perfect case for the distinguishability is in between,  $\eta = 0.5$ , Fig. 3.9c. Half of the photons interact with the spin, transforming  $h$  polarization into  $\pm v$ , and half is reflected from the mirror, conserving  $h$ . As there are equal proportions of  $h$  and  $v$ , the spin-up (-down) state will transform horizontal light into the left-(right-)polarized one. The corresponding polarizations are orthogonal:  $D = 1$ , and the spin states perfectly distinguishable.

In the intermediate cases  $0 < \eta < 0.5$  and  $0.5 < \eta < 1$  (example of  $\eta = 0.75$  in Fig. 3.9d) the distinguishability has intermediate values  $0 < D < 1$ .

The value of  $\eta = 0.5$  as the optimal one seems to be contradictory with the first part of the chapter, where the effective dephasing had no special features for the value of  $\eta = 0.5$ . However, the effective dephasing exists because of the interaction of the spin with light, and it does not depend on the measured observable, choice of the basis etc. Maximum of  $D$  for  $\eta = 0.5$  is connected to the fact that in this section we restricted ourselves to the measurement of the light intensities. In this case we lose the information on the phase of the emitted light, and we can not resolve between  $v$  and  $-v$  - polarizations that correspond to  $\eta = 1$ , according to Eq. (3.31). If we would focus on the homodyne measurement instead,  $\eta = 1$  would be the optimal value.

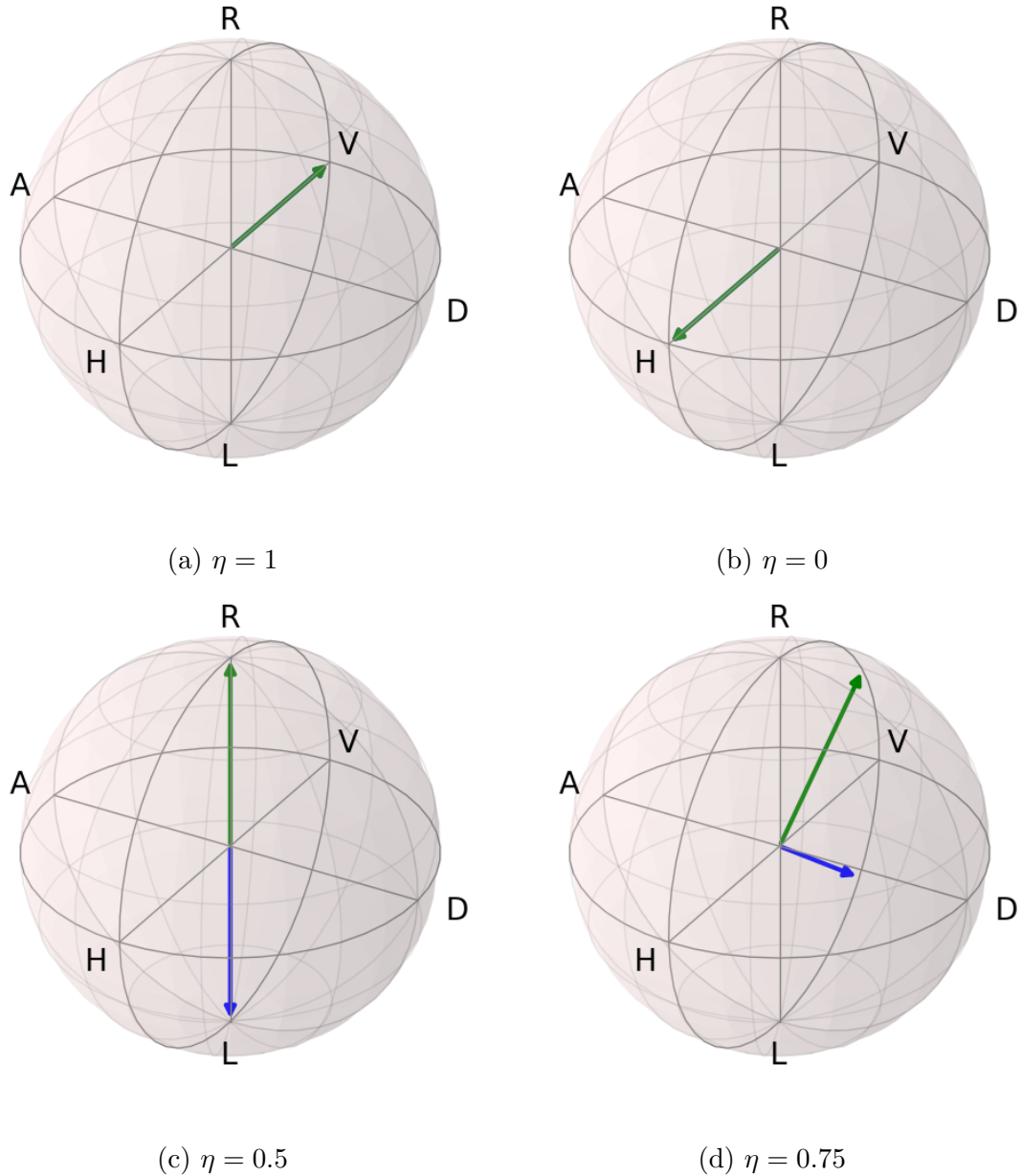


Figure 3.9: Polarizations of reflected light  $\vec{\varepsilon}_{\uparrow(\downarrow)}$  on the Poincaré sphere for different values of  $\eta$ , if the power of the horizontally polarized pump is low ( $|b^{in}|^2 = 10^{-6}\gamma$ ). The green vector corresponds to the spin-down state  $\vec{\varepsilon}_{\downarrow}$ , the blue vector corresponds to the spin-up state  $\vec{\varepsilon}_{\uparrow}$ .

### Laser power

The dependence on the pump power is illustrated in Fig. 3.10, for the most optimal case of  $\eta = 0.5$ . The low power, as in Fig. 3.10a, ensures that all the light interacts with the spin, hence maximal information is retrieved and  $D = 1$ .

With the increase of pump power, the trion levels gradually become more populated. As the saturation is reached, more photons are reflected from the mirror without interaction with the QD (Figs. 3.10b and 3.10c). Not only the angle between the states of light, that correspond to different spin states, decreases, but also

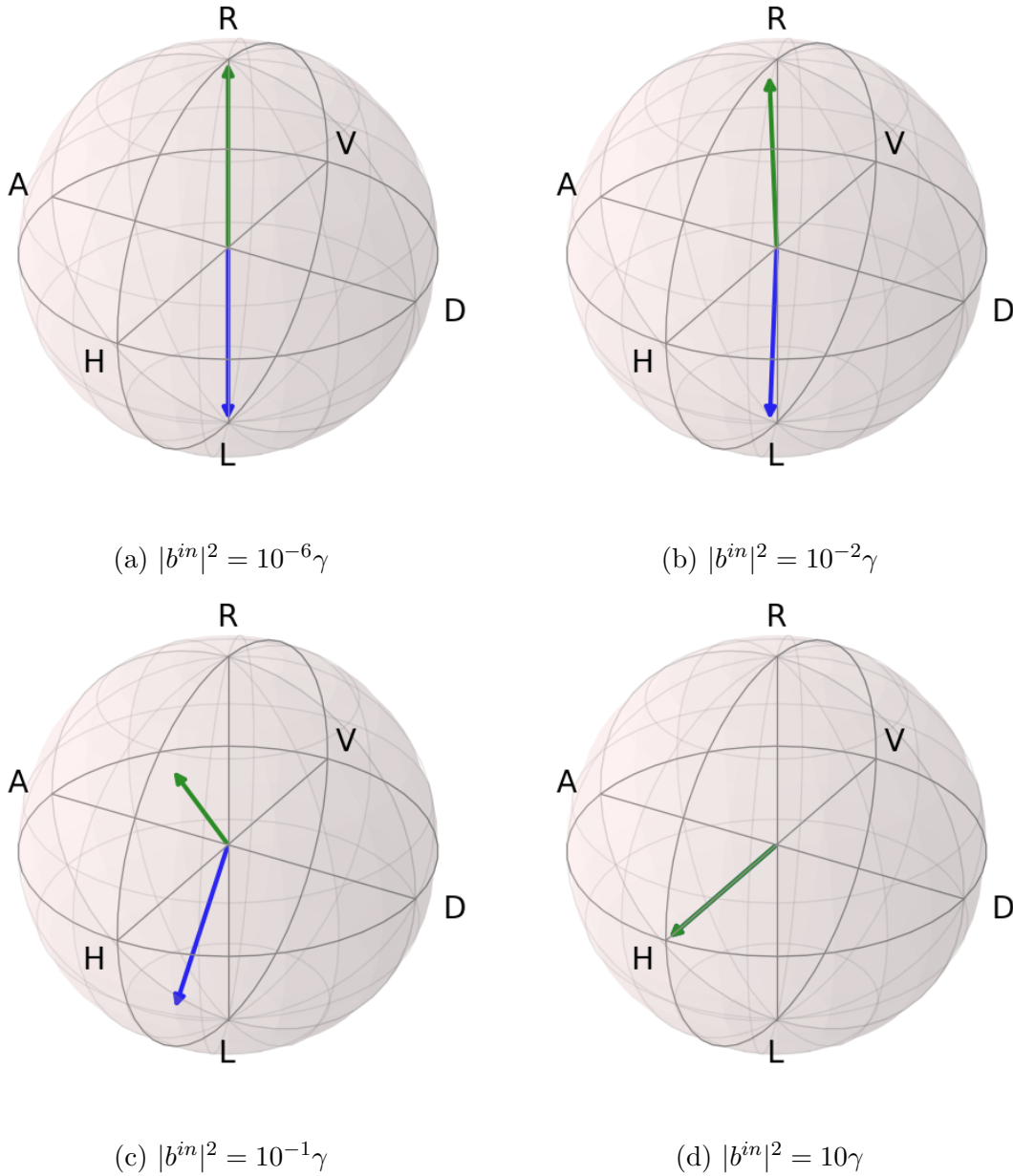


Figure 3.10: Polarizations of reflected light  $\vec{\varepsilon}_{\uparrow(\downarrow)}$  on the Poincaré sphere for different values of power of the horizontally polarized pump  $|b^{in}|^2$ , if  $\eta = 0.5$ . The green vector corresponds to the spin-down state  $\vec{\varepsilon}_{\downarrow}$ , the blue vector corresponds to the spin-up state  $\vec{\varepsilon}_{\uparrow}$ .

the degree of the polarization: note the arrows inside the sphere in Fig. 3.10c. This happens due to the power broadening: as the QD becomes saturated, its spectrum becomes more broad [124] and does not coincide with the spectrum of the reflected light. Due to the reduced overlap, the light loses the degree of polarization.

Finally, when saturation is reached, most photons do not interact with the spin, their polarization is not changed,  $D \approx 0$ , as for the case of Fig. 3.10d. However, there are always some of the photons that do interact with the spin. Hence, to be able to distinguish between the spin states, one needs to analyse the polarization of



large number of photons, and the higher is the incident power, the more photons should be detected to resolve the spin states. This point will be discussed more in the last section.

In this section we discussed the quality of the measurement of the spin polarization via the rotation of the polarization of the scattered light. We described the polarization rotation in terms of the vectors on the Poincaré sphere and demonstrated that the optimal measurement of the state of the spin can be performed with a weak pump if the value of  $\eta$  is 0.5. Deviations from this value lower the distinguishability of the spin states.

### 3.4 Quantum trajectories

In the previous sections we have investigated the dynamics of the spin including the impact of the interaction with the electromagnetic field. We also investigated the influence of the state of the spin on the light polarization, and the prospects to use it to measure the spin state. This was performed in the formalism of Master Equation and the input-output formalism that give description of the processes on average. In an experiment, this would correspond to averaging clicks in detectors over a large number of realizations.

We now turn to more detailed analysis of the measurement process, focusing on unique realizations, corresponding to the stochastic sequence of clicks. Such a realization, as was mentioned in the introduction to the chapter, is called quantum trajectory  $\gamma$ : a sequence of quantum states  $\{|\psi_\gamma(t_n)\rangle\}$  of the system  $\mathcal{S}$  at times  $\{t_n\}$ , that is defined by outcomes  $\{m_\mu^\gamma(t_n)\}$  of the measurements, performed over environment  $\mathcal{E}$  at these times, and unitary evolution between them. The time instants are chosen homogeneously:  $t_n = t_0 + n dt$ , where the interval  $dt$  is much longer than the correlation time of the environment  $\tau_e$ .

Each of the measurement outcomes can be represented by a Kraus operator  $M_\mu(dt)$  [57], that governs the stochastic evolution of the system between  $t_n$  and  $t_{n+1}$ . A measurement of the outcome  $m_\mu$ , obtained in this time span acts on the state of the system as

$$|\psi_\gamma(t_{n+1})\rangle = \frac{M_\mu(dt)|\psi_\gamma(t_n)\rangle}{\sqrt{P_\mu(t_n)}} \quad (3.35)$$

the probability of such an event being  $P_\mu(t_n) = \langle \psi_\gamma(t_n) | M_\mu^\dagger(dt) M_\mu(dt) | \psi_\gamma(t_n) \rangle$ . Conservation of probability implies the following condition:

$$\sum_\mu M_\mu^\dagger(dt) M_\mu(dt) = \mathbb{1} \quad (3.36)$$

In the case we are studying in the chapter, the system is the QD doped with a spin, and the electromagnetic field is the environment that acts as a quantum meter. The measured observables are the numbers of the photons detected in two orthogonal polarizations. If we assume the perfect efficiency of the detectors, one of the five events can happen between  $t_n$  and  $t_{n+1}$ :

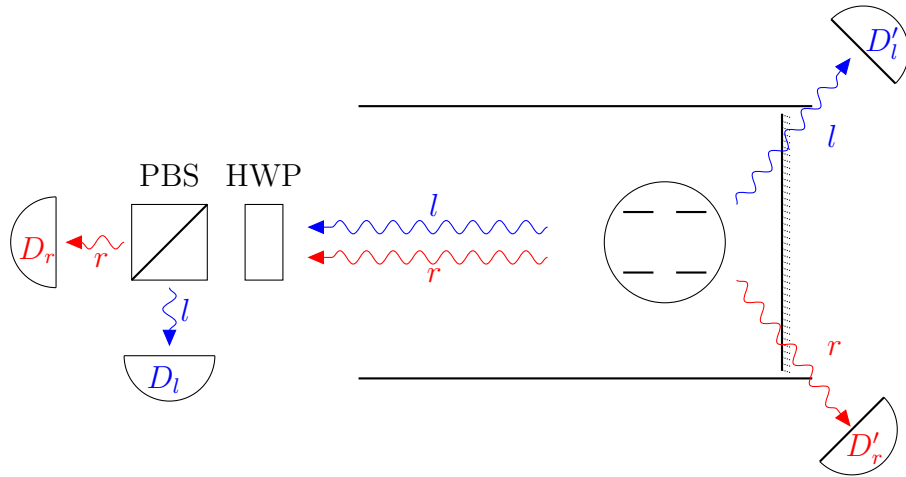


Figure 3.11: Scheme of a possible experiment. The curved lines represent possible photoemission options. Part of the emitted photons is directed to a half wave plate (HWP) and polarizing beam splitter (PBS) and then to ideal detectors, so that the  $l$ - and the  $r$ -polarized photons go to different detectors  $D_{r,l}$ . The part of the emitted photons, that is considered lost, is treated as the non-read measurements by the detectors  $D'_{r,l}$ .

- 0) no photon will be detected (no click),
- 1) a photon in  $r$  polarization will be detected after scattering on either the system or the mirror (click in  $D_r$ ),
- 2) a photon in  $l$  polarization will be detected after scattering on either the system or the mirror (click in  $D_l$ ),
- 3) a photon in  $r$  polarization will be emitted out of mode (click in  $D'_r$ ),
- 4) a photon in  $l$  polarization will be emitted out of mode (click in  $D'_l$ ).

These events are schematically shown in Fig. 3.11 with red and blue arrows, representing  $r$  and  $l$  polarizations respectively. The last two cases describe the losses; in the following sections they will be treated as unread measurements.

The exact expression of  $M_\mu$  depends on the way, how one measures the meter. In the situation under study, there are two main parameters: the detection polarization basis and the intensity of the incident light field.

The choice of a set of the Kraus operators is called unravelling. We focus on two types of unravelling, that represent two limit cases of low and high pump power:

- Quantum Jumps (QJ): corresponds to the low power limit. The QD electron-trion transition is not saturated, and every detected photon brings information on the spin state, causing strong back-action ( $M_\mu \propto \sigma_{r,l}$ ).
- Quantum State Diffusion (QSD): corresponds to the high power regime. Most of the incident photons are reflected from the mirror, carrying less information on the spin state and the back-action is weak ( $M_\mu \propto \mathbb{1}$ ).

In the set-up of the Fig. 3.11 it is possible to change the detection polarization basis by adding or removing HWP. In this section we assume that the measured

polarizations are  $r$  and  $l$ . We also assume that  $\eta = 0.5$  and that the incident light has horizontal polarization.

### 3.4.1 Quantum Jumps

In the QJ unravelling the set of the possible measurement results is discrete, and coincides with the five outcomes in the list in the previous section. As the incident power is low, the probability of emission of a photon is also low, and either none or only one of events 1)-4) can happen during  $dt$ . Thus the measurement outcome  $m_\mu^\gamma(t)$  is 0 or 1, with  $\sum_{\mu=0}^4 m_\mu^\gamma(t) = 1$ .

The outcomes 1)-2), when the scattered photon is detected, give rise to the following Kraus operators [58]:

$$M_{1(2)}(dt) = \sqrt{dt} L_{r(l)} \quad (3.37a)$$

$$L_j = \sqrt{\gamma\eta} \sigma_j + \mathbb{1} b_j^{in}, \quad j = r, l \quad (3.37b)$$

The two terms in Eq. (3.37b) represent the two different components of the scattered field. The first term represents the situation when the photon was initially absorbed by the system, and afterwards reemitted. The second one stands for the case when the field did not interact with the spin, but was just reflected from the mirror. It happens when the optical selection rules prohibit the interaction (e.g. the spin is up, and the light is left-polarized).

The outcomes 3)-4), when the photon is lost, are represented by

$$M_{3(4)}(dt) = \sqrt{dt} L_{r(l),loss} \quad (3.38a)$$

$$L_{j,loss} = \sqrt{\gamma(1-\eta)} \sigma_j, \quad j = r, l \quad (3.38b)$$

In the 0) case, the evolution is governed by the no-jump operator

$$\begin{aligned} M_0(dt) &= \mathbb{1} - iH_s dt - \frac{dt}{2} \sum_{\mu \neq 0} L_\mu^\dagger(dt) L_\mu(dt) = \\ &= \mathbb{1} - iH_s dt - \frac{dt}{2} \sum_{j=r,l} \left[ |b_j^{in}|^2 + \gamma \sigma_j^\dagger \sigma_j + \sqrt{\gamma\eta} \left( \sigma_j^\dagger b_j^{in} + \text{h.c.} \right) \right] \end{aligned} \quad (3.39)$$

where  $H_s$  is a part of the no-jump operator, that is responsible for unitary evolution. As the interaction of the QD with the pump is already partially accounted in  $M_0(dt)$  in the term in the square brackets, the unitary operator  $H_s$  writes [58]:

$$H_s = H + H_B - \frac{i}{2} \sum_{j=r,l} \sqrt{\eta\gamma} \left( (b_j^{in})^* \sigma_j - \sigma_j^\dagger b_j^{in} \right)$$

where

$$H = i\sqrt{\eta\gamma} \sum_{j=r,l} \left( (b_j^{in})^* \sigma_j - \sigma_j^\dagger b_j^{in} \right)$$

All the five possible outcomes can be summed up as a single evolution equation, that is called Stochastic Schrödinger equation [58]:

$$|d\psi(t)\rangle = \left[ -iH_s dt - \frac{1}{2} \sum_{\mu \neq 0} (L_\mu^\dagger L_\mu - \langle L_\mu^\dagger L_\mu \rangle) dt + \sum_{\mu \neq 0} dN_\mu(t) \left( \frac{L_\mu}{\sqrt{\langle L_\mu^\dagger L_\mu \rangle}} - \mathbb{1} \right) \right] |\psi_\gamma(t)\rangle$$

$$dN_\mu(t) = \{0, 1\}$$
(3.40)

where  $dN_\mu(t)$  is a set of random numbers that indicates, which of the five possible events occurred between  $t$  and  $t + dt$ . The emission and the detection or a loss of a photon in given polarization happens when for a corresponding  $\mu$ , the  $dN_\mu(t) = 1$ . If for certain  $t$ ,  $\forall \mu dN_\mu(t) = 0$ , it means that the event 0) happens, providing the no-jump evolution.  $dN_\mu(t)$  is distributed according to the Poissonian statistics with mean value  $E[dN_\mu(t)] = \langle L_\mu^\dagger L_\mu \rangle dt$ , and  $\langle L_\mu^\dagger L_\mu \rangle = \langle \psi_\gamma(t) | L_\mu^\dagger L_\mu | \psi_\gamma(t) \rangle$ .

A density matrix represents more general case than a state vector, and equation for the dynamics of the density matrix  $\rho_\gamma$  can be obtained from (3.40) keeping the first order in  $dt$ , according to the Ito rules [58].

$$d\rho_\gamma(t) = |d\psi(t)\rangle \langle \psi_\gamma(t)| + |\psi_\gamma(t)\rangle \langle d\psi(t)| + |d\psi(t)\rangle \langle d\psi(t)|$$
(3.41)

The Stochastic Master Equation writes:

$$d\rho_\gamma = -i[H_s, \rho_\gamma] dt - \frac{1}{2} \sum_{\mu \neq 0} (\{L_\mu^\dagger L_\mu, \rho_\gamma\} - 2\rho_\gamma \langle L_\mu^\dagger L_\mu \rangle) dt + \sum_{\mu \neq 0} dN_\mu(t) \left( \frac{L_\mu \rho_\gamma L_\mu^\dagger}{\langle L_\mu^\dagger L_\mu \rangle} - \rho_\gamma \right)$$
(3.42)

where the curved brackets mean an anticommutator:  $\{A, B\} = AB + BA$ .

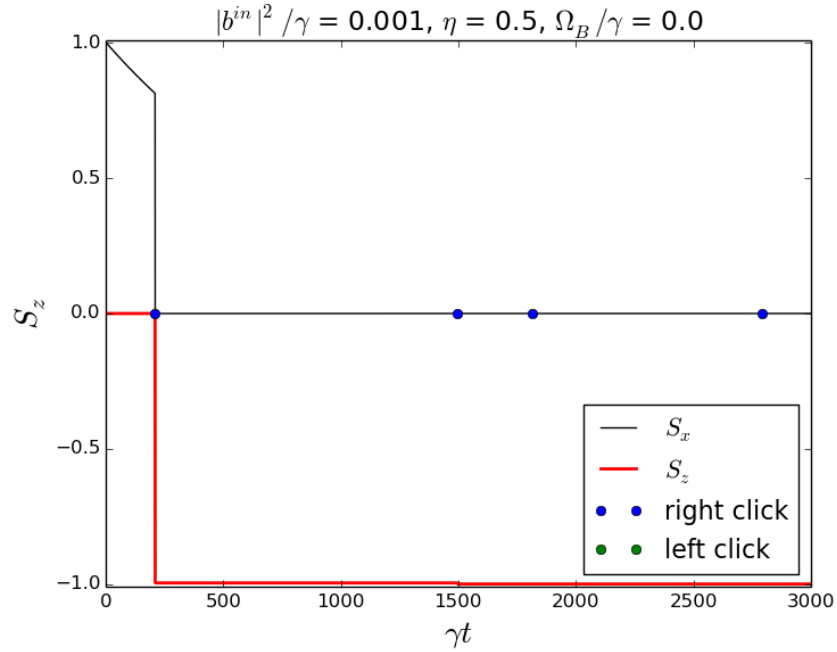
In practice the lost photons can not be tracked, and we can not know, when they were emitted, and in which polarization. It makes us average over  $dN_{j,loss}(dt)$ , treating the cases 3) and 4) as unread measurements. After averaging Eq. (3.42) over the losses, one obtains

$$d\rho_\gamma = -i[H_s, \rho_\gamma] dt - \frac{dt}{2} \sum_{j=r,l} \left( \left\{ L_{j,loss}^\dagger L_{j,loss}, \rho_\gamma \right\} - 2L_{j,loss} \rho_\gamma L_{j,loss}^\dagger \right) -$$

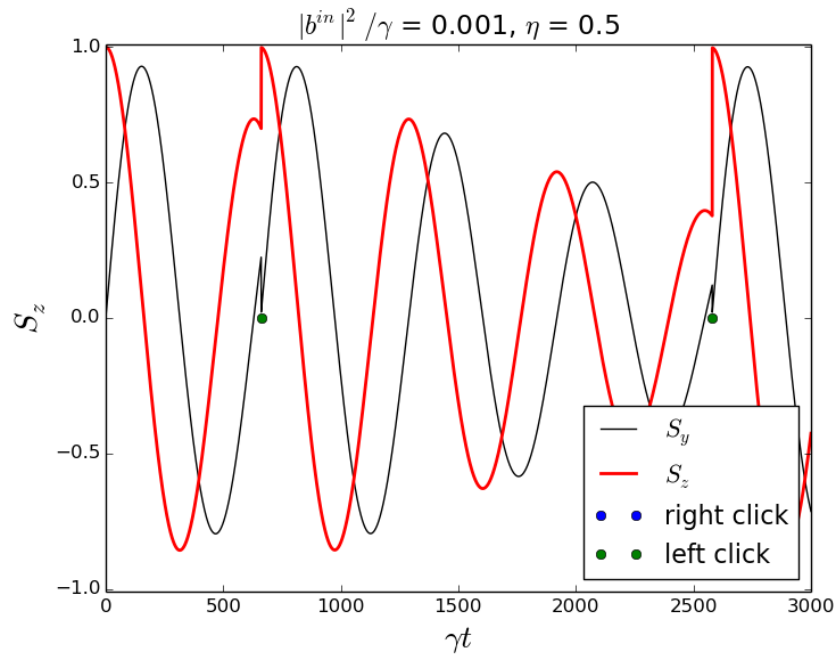
$$- \frac{dt}{2} \sum_{j=r,l} \left( \left\{ L_j^\dagger L_j, \rho_\gamma \right\} - 2\rho_\gamma \langle L_j^\dagger L_j \rangle \right) + \sum_{j=r,l} dN_j(t) \left( \frac{L_j \rho_\gamma L_j^\dagger}{\langle L_j^\dagger L_j \rangle} - \rho_\gamma \right)$$
(3.43)

The equation (3.43) allow us to track the evolution of the system during an individual realization of the experiment. This equation is solved numerically. For each  $t$  the values of  $dN_j(t)$  are randomly chosen and the state at the time  $t + dt$  is calculated as  $\rho_\gamma(t + dt) = \rho_\gamma(t) + d\rho_\gamma(t)$ , where the second term is calculated according to the Eq. (3.43)<sup>1</sup>. The average value over a number of such trajectories of the Eqs. (3.42) and (3.43) is the Master equation Eq. (3.13).

<sup>1</sup>There are more optimal ways for numerical solution of this equation, but this one is sufficient for our purposes.



(a) The initial state is  $(|\uparrow\rangle + |\downarrow\rangle)/\sqrt{2}$ . After some time a photodetection event occurs (at times, marked by circles in the middle). A detected  $r$  photon projects the spin onto a state close to  $|\downarrow\rangle$ , and then only  $r$  photons are detected.



(b) The initial state is  $|\uparrow\rangle$ . The spin oscillates in magnetic field, and the purity of the state decreases due to the possible undetected photons. After a click the system is re-initialized.

Figure 3.12: Typical trajectories under the optimal measurement conditions: low power:  $|b_j^{in}|^2 = 10^{-3}\gamma$ ,  $\eta = 0.5$ , the  $\{r, l\}$  measurement basis.

Some typical trajectories are shown in Fig. 3.12, where the red lines represent  $S_z$ , Eq. (3.10c), and the black lines - the coherences between them, according to the Eq. (3.11). The circles in central part of the plots indicate times, when a click is detected, with different colours for different polarizations.

The panel 3.12a represents the case without the magnetic field. The initial state of the spin is the superposition  $(|\uparrow\rangle + |\downarrow\rangle)/\sqrt{2}$ . Before the first photodetection there is loss of coherence between spin states because of the undetected photons. The first detected photon can be in either  $r$  or  $l$  polarization, with equal probability, as the probabilities to find the spin in up or down states are equal as well.

Let us remind the correspondence between the spin state and the detected photon polarization, explained in the previous section:

Spin state	$S_z$	Detected photon polarization
$ \uparrow\rangle$	1	$l$
$ \downarrow\rangle$	-1	$r$

In the figure, the first photon is detected with  $r$  polarization. After the click, the spin state is projected close to the spin-down state, with the after-click probability to find the spin in  $|\downarrow\rangle$  state is  $\rho_{\downarrow\downarrow} = 1 - \mathcal{O}(|b^{in}|^2/\gamma)$ . It is not a complete projection because there is finite, though infinitesimal, probability that the trion level was excited and the detected photon comes from the mirror, due to the second term in Eq. (3.37b). Note that a weak measurement of the spin is performed, evaluating the observable of the electromagnetic field, not of the spin itself, and yet the measurement is projective.

After the spin has been projected close to the down state, it almost stops to interact with  $r$  light, that is now reflected from the mirror. The  $l$  light continues to interact with the spin. Because of  $\eta = 0.5$ , half of it is reflected from the mirror without interaction with the spin, and half is scattered on the spin, inverting the phase. The scattered and the reflected light interfere destructively due to the opposite phases, and the probability to detect a  $l$  photon almost vanishes, that's why the second detected photon has much higher probability to have the same polarization, as the first one.

Similarly, the probability to detect a  $l$  photon, thus projecting the spin onto another state, is close to zero. The state of the spin becomes stable, and remains up.

If an ensemble of different trajectories of this kind is averaged, one retrieves the effective dephasing described in the previous sections. It appears because the moment of the photoemission and the polarization of the emitted photon are random. All detection events project the spin onto either  $|\uparrow\rangle$  or  $|\downarrow\rangle$  state, destroying the coherence between these states. Since these events take place at stochastic times, on average this effect corresponds to continuous damping of the spin coherences  $S_{x,y}$ .

The Fig. 3.12b presents a trajectory if the magnetic field is turned on. The oscillations represent the precession of the spin, and the relaxation happens because of the non-read measurements by the non-detected photons. After every detection

the state of the spin is projected onto  $|\uparrow\rangle$  or  $|\downarrow\rangle$  state, restoring the purity of the state. This corresponds to “resets” of the Larmor precession.

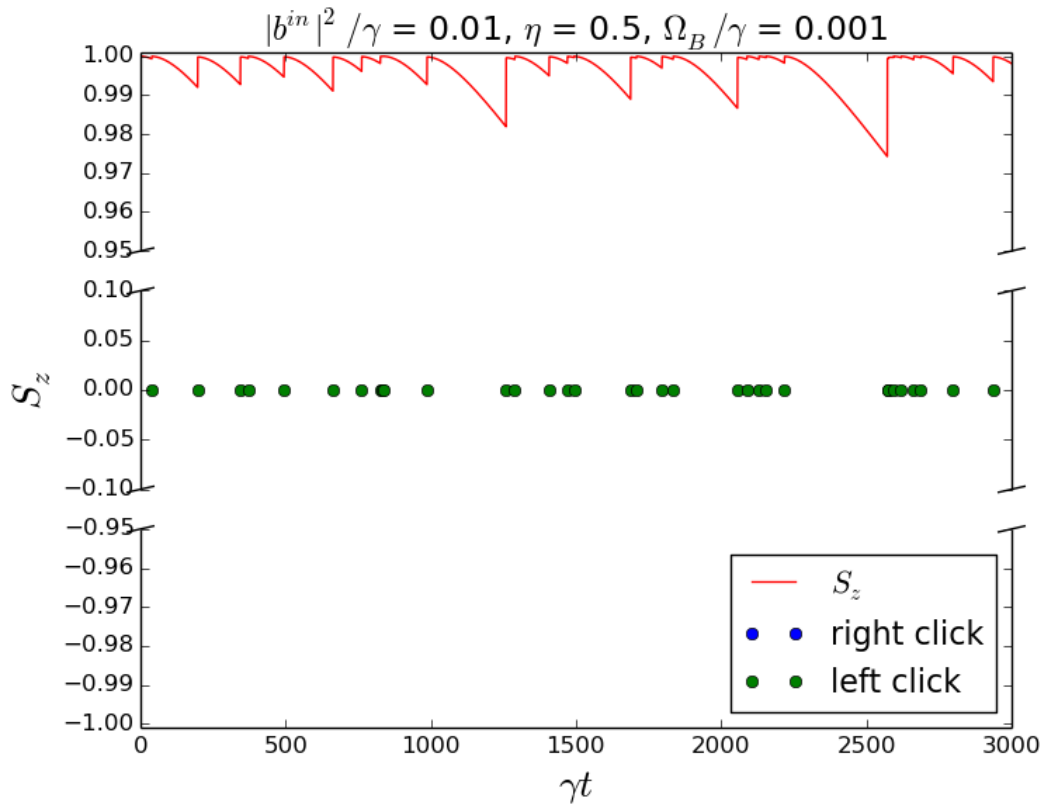


Figure 3.13: Zeno effect at a single trajectory level.

By adjusting the time scales one can observe particular features of the dynamics. If the values of the Larmor frequency, the laser power and the saturation power satisfy the condition

$$\Omega_B \ll 16\eta|b^{in}|^2 \ll \gamma$$

each jump, though it happens at random moment, projects the spin onto the same state, freezing the dynamics. It represents the case of Zeno regime, shown in Fig. 3.13.

This dynamics can be used to prepare the spin in any state. First, if the spin starts in some unknown mixed state, one waits for the click that indicates the projection. Then the laser is turned off and the magnetic field rotates the field to the target state.

### 3.4.2 Quantum state diffusion

If the pump power is high,  $|b^{in}|^2 \gg \gamma$ , multiple events of types 1)-4) can occur during the same  $dt$ . The measurement outcomes  $m_k^\gamma(t)$  are intensities in each polarization, and in the high-power regime they are continuous values. This situation corresponds to the QSD unravelling.

With the increase of the pump power, the information carried by a single click, decreases: there is higher probability that the trion transition is saturated, and that the photon that was detected, came from the input field  $b_i^{in}$ , reflected from the mirror, rather than from the QD emission. The second term of the jump operator Eq. (3.37b) dominates over the first one, and the back-action from a single click is negligible.

In the limit  $|b^{in}|^2 \gg \gamma$  the Stochastic Master Equation (3.43) writes [58]:

$$d\rho_\gamma = -i[H + H_B, \rho_\gamma] dt - \frac{dt}{2} \sum_{\mu=1}^4 \left( \left\{ \tilde{L}_\mu^\dagger \tilde{L}_\mu, \rho_\gamma \right\} - 2\tilde{L}_\mu \rho_\gamma \tilde{L}_\mu^\dagger \right) + \sum_{\mu=1}^2 dW_j(t) \left[ \left( \tilde{L}_j - \langle \tilde{L}_j \rangle \right) \rho_\gamma + \rho_\gamma \left( \tilde{L}_j^\dagger - \langle \tilde{L}_j^\dagger \rangle \right) \right] \quad (3.44)$$

where the Stochastic Wiener increments  $dW_{1,2}(t)$ , that represent deviation of a measured value from its average, have Gaussian distribution with mean  $E[dW_{1,2}(t)] = 0$  and  $[dW_{1,2}(t)]^2 = dt$ , and the new jump operators are

$$\tilde{L}_{1(2)} = \sqrt{\gamma\eta} \sigma_{r(l)}, \quad (3.45a)$$

$$\tilde{L}_{3(4)} = \sqrt{\gamma(1-\eta)} \sigma_{r(l)} \quad (3.45b)$$

The Figs. 3.14 and 3.15 show the typical trajectories if the pump power is above saturation. The vertical axes represent the spin polarization  $S_z$ . Multiple clicks happen each  $dt$ , and each of them has only a small impact over the dynamics. Thus, the information on the state of the spin is extracted in continuous manner, accumulating over time. If there is no magnetic field (Fig. 3.14), the spin state eventually becomes oriented along one of the two directions due to the measurement back action.

In Fig. 3.15 the magnetic field is taken into consideration, for three values of  $\Omega_B$ , that represent different orders of magnitude comparatively to  $\gamma_{eff}^* = \gamma/2$ , Eq. (3.20). The initial state is  $|\uparrow\rangle$ . If the precession is faster than the effective decoherence  $\Omega_B > \gamma_{eff}^*$  (the red curve), the magnetic field rotates the spin. If the precession is slower than the decoherence  $\Omega_B < \gamma_{eff}^*$  (black curve), there are still some deviations from the initial state, but they are much smaller. And for the field with very low Larmor frequency  $\Omega_B \ll \gamma_{eff}^*$ , the measurement freezes the spin precession.

In this section we considered the dynamics of the system in a single realization, focusing on the cases of the very low power with the QJ unravelling and very high power, corresponding to the QSD. The former case grants the best possibility to measure the state of the spin and induces the maximal back-action. We found that in this regime the state of the spin can be measured via detection of as many as one photon, and the dynamics of the spin in the presence of the magnetic field can be freezed. In the case of the high power excitation most of the incident photons do not interact with the spin, thus they bring little information about the spin state. This makes the measurement of the spin state via single photon detection impossible, and the measurement requires processing of a high number of scattered photons. Also,



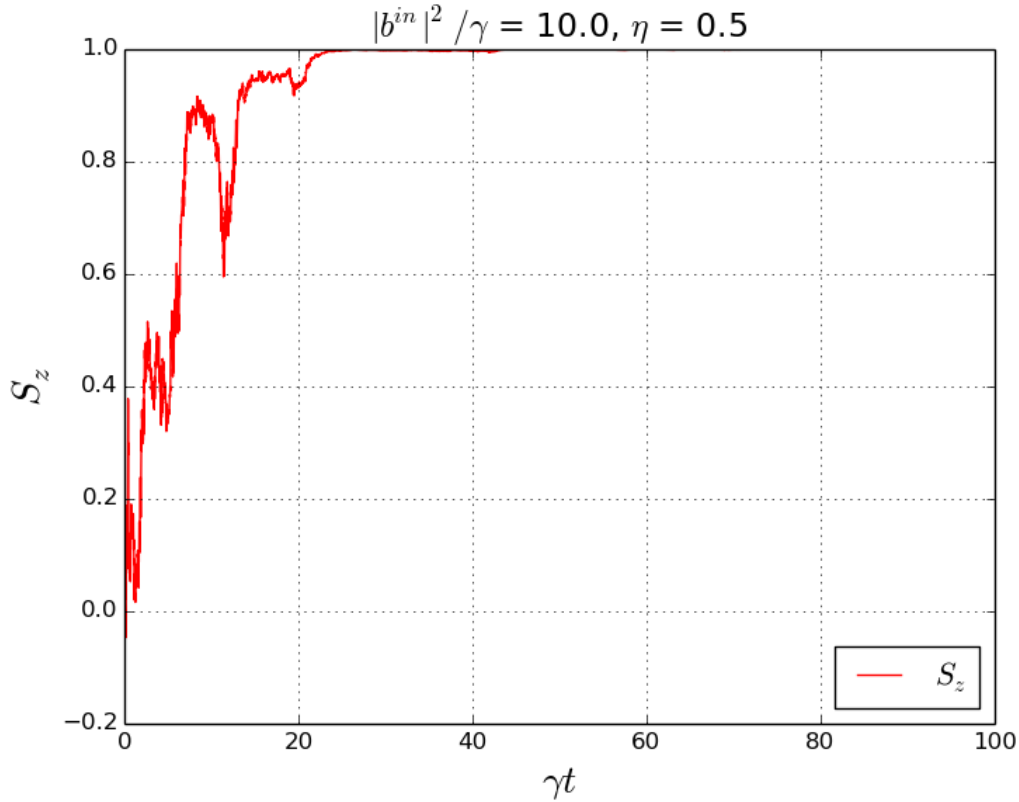


Figure 3.14: Trajectory with no magnetic field ( $\Omega_B = 0$ ). The pump power is  $|b_j^{in}|^2 = 10\gamma$ . The initial state is  $(|\uparrow\rangle + |\downarrow\rangle)/\sqrt{2}$ . After some time the spin is projected onto  $|\uparrow\rangle$ .

the trajectory approach allows us to see the origin of the aforementioned effective spin dephasing in the photodetection events that project the system onto one state, thus decreasing the coherences.

## 3.5 The measurement imperfections

In this section we would like to consider possible deviations from the optimal measurement conditions of the previous case, restricting ourselves to the QJ unravelling and low power limit.

### 3.5.1 Imperfect photodetectors

In the previous case we assumed that the detectors work with 100% efficiency, which is a very strong approximation. To account for imperfect detection, we extend the possible number of events, adding two more to the set, presented in Sect. 3.4:

- 5) a photon in  $r$  polarization will be scattered on either the system or the mirror towards  $D_r$ , but not detected
- 6) a photon in  $l$  polarization will be scattered on either the system or the mirror towards  $D_l$ , but not detected

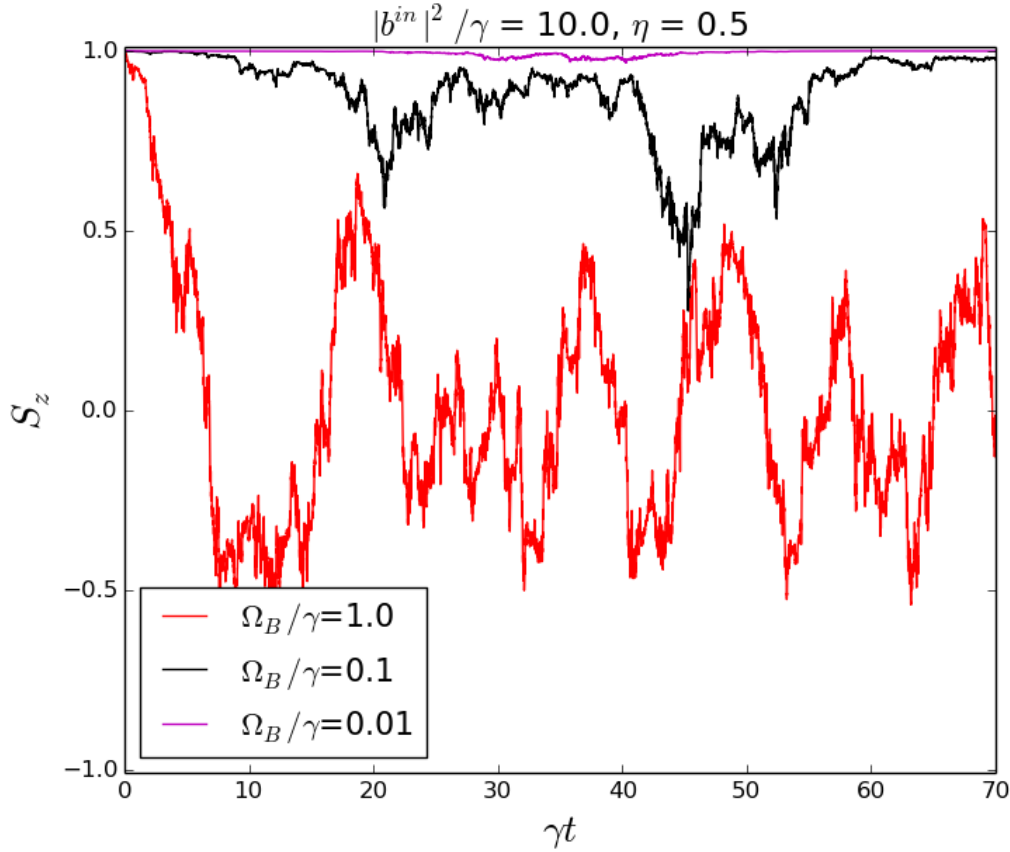


Figure 3.15: Trajectory in the magnetic field. The pump power is  $|b_j^{in}|^2 = 10\gamma$ . The initial state is  $|\uparrow\rangle$ .

If detection efficiency is  $\eta_{det}$ , the operators that correspond to 1),2),5),6) write

$$M_{1(2)}(dt) = \sqrt{\eta_{det}dt}L_{r(l)} \quad (3.46a)$$

$$M_{5(6)}(dt) = \sqrt{1 - \eta_{det}}\sqrt{dt}L_{r(l)} \quad (3.46b)$$

Scattering of the undetected photons can be treated as an unread measurement, and to get the evolution equation of the system in this conditions, we need to average over the cases 5)-6), as was done with 3)-4) in the previous section.

$$\begin{aligned} d\rho_\gamma = & -i[H_s, \rho_\gamma] dt - \\ & -\frac{dt}{2} \sum_{j=r,l} \left( \left\{ L_{j,loss}^\dagger L_{j,loss}, \rho_\gamma \right\} - 2L_{j,loss}\rho_\gamma L_{j,loss}^\dagger \right) - \\ & -\frac{dt}{2} \sum_{j=r,l} \left( \left\{ L_j^\dagger L_j, \rho_\gamma \right\} - \eta_{det}2\rho_\gamma \langle L_j^\dagger L_j \rangle - 2(1 - \eta_{det})L_j\rho_\gamma L_j^\dagger \right) + \\ & + \sum_{j=r,l} dN_j(t) \left( \frac{L_j\rho_\gamma L_j^\dagger}{\langle L_j^\dagger L_j \rangle} - \rho_\gamma \right) \end{aligned} \quad (3.47)$$

The average click rate is changed as well:  $E[dN_j(t)] = \eta_{det}\langle L_j^\dagger L_j \rangle dt$

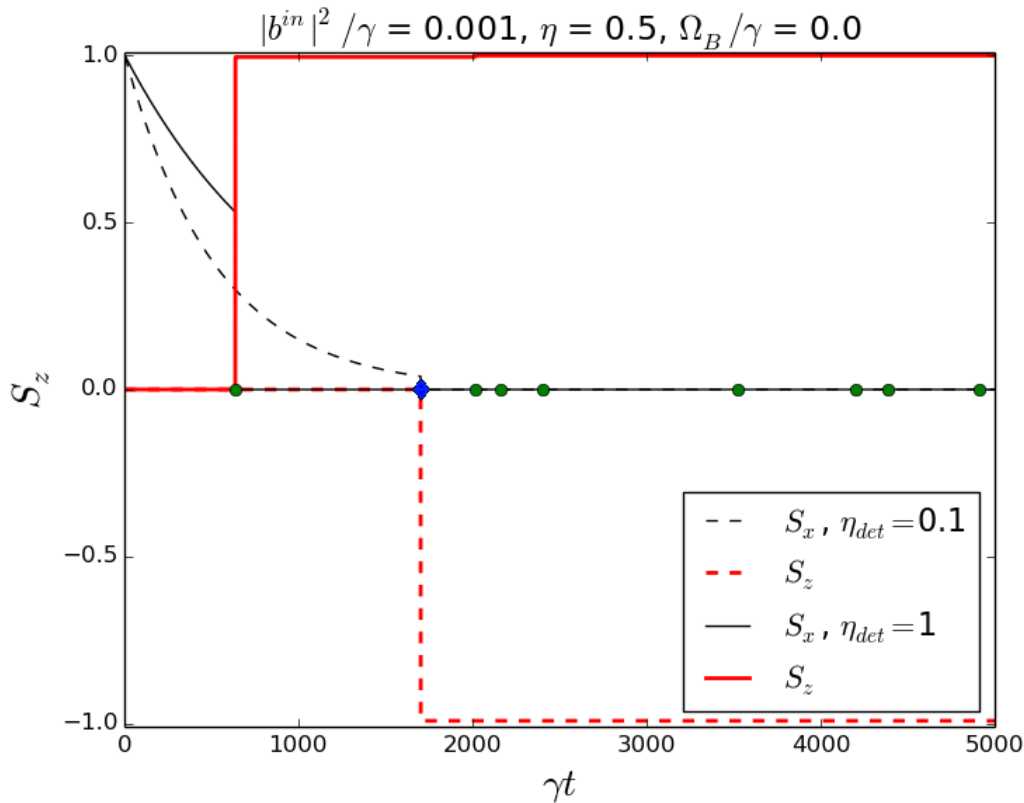


Figure 3.16: The typical trajectory for the same conditions as in Fig. 3.12a, but with different detection efficiency  $\eta_{det}$ . The solid lines and the circles represent the ideal case,  $\eta_{det} = 1$ . The dashed lines and the diamonds state for low efficiency  $\eta_{det} = 0.1$ . The red lines show the difference between the populations of spin states with different states, and essentially the dynamics is the same as in Fig. 3.12a for both high and low efficiency cases. The only obvious difference lies in much smaller number of photons, detected with bad detectors.

The magenta lines show spin coherence, and for the low detection efficiency it decreases much faster because of the information on the state, lost with undetected photons.

The Fig. 3.16 shows two trajectories. One is the case of perfect detectors  $\eta_{det} = 1$ , shown by solid lines and clicks marked with circles. Another trajectory on the plot corresponds to the case of imperfect detectors,  $\eta_{det} = 0.1$ , with dashed lines, and the only click marked with a diamond. The green (blue) colour of the points in the middle corresponds to the left-(right-) polarized photons.

The first noticeable difference lies in the number of clicks: obviously, the most efficient detector has more probability to register a photon. The populations of the electron spin up and spin down level, shown in blue and green, become very close to 1 and 0, correspondingly, after the click in a detector of left-polarized photons, independently on its efficiency.

The coherence between the spin states, shown in black, decreases due to the unread measurement by the undetected photons. In the ideal case, all the undetected

photons come from the QD emission out of the mode. With the low detectors efficiency the number of the unread measurements is increased due to the photons that were not registered by the detectors. As the number of the undetected photons is higher, so is the decay rate of the coherence between the two spin states.

Note, that on average, the effective dephasing rate will be the same for both cases, as the detected photons also contribute to the decay rate of averaged coherences. Mathematically, effective dephasing does not depend on the detectors efficiency, as the average evolution is governed by the Eq. (3.13), that does not include  $\eta_{tot}$ .

### 3.5.2 Non-optimal measurement basis

The other possible imperfection of the setup is a choice of the measurement basis that does not correspond to the maximally distinguishable states [116].

If the detectors measure in a set of orthogonal polarizations characterized by the angles  $\theta$  and  $\phi$ , the jump operators  $\{L_r, L_l\}$  are to be replaced by

$$L_+ = L_r \cos\left(\frac{\theta}{2} + \frac{\pi}{4}\right) + L_l e^{i\phi} \sin\left(\frac{\theta}{2} + \frac{\pi}{4}\right) \quad (3.48a)$$

$$L_- = -L_r \sin\left(\frac{\theta}{2} + \frac{\pi}{4}\right) + L_l e^{-i\phi} \cos\left(\frac{\theta}{2} + \frac{\pi}{4}\right) \quad (3.48b)$$

And a similar replacement should be made in the Kraus operators and in the  $dN_i(t)$ . The case of  $\theta = \pi/2$  corresponds to the situation of the previous section.

Like in a case of a perfect measurement  $L_j$  projects the spin state onto up or down electron states,  $L_{\pm}$  projects it onto their superposition. For the horizontal initial state polarization and  $S_z(0) = 0$ , the correspondence between the detected photons and the spin projections is

Detected polarization	Spin state after the click
+	$ \downarrow\rangle \cos\left(\frac{\theta}{2} + \frac{\pi}{4}\right) +  \uparrow\rangle e^{i\phi} \sin\left(\frac{\theta}{2} + \frac{\pi}{4}\right)$
-	$- \downarrow\rangle \sin\left(\frac{\theta}{2} + \frac{\pi}{4}\right) +  \uparrow\rangle e^{i\phi} \cos\left(\frac{\theta}{2} + \frac{\pi}{4}\right)$

Independently on the basis, the average equation of motion will be Eq. 3.13, so the effective dephasing, introduced before, will not change with the changes of the basis.

The possible trajectories are depicted in Figs. 3.17 and 3.18

If  $\theta = 0$  and  $\phi = 0$ , the jump operators (3.48) correspond to detection of  $h$  and  $v$  photons. Knowing that the  $|\uparrow\rangle$  ( $|\downarrow\rangle$ ) spin state transforms  $h$  polarization into  $l$  ( $r$ ), we can symbolically represent the state of the reflected light and spin in  $\{h, v\}$  basis as

$$C_{\uparrow}|l, \uparrow\rangle + C_{\downarrow}|r, \downarrow\rangle = \frac{|h\rangle (C_{\uparrow}|\uparrow\rangle + C_{\downarrow}|\downarrow\rangle) + i|v\rangle (C_{\uparrow}|\uparrow\rangle - C_{\downarrow}|\downarrow\rangle)}{\sqrt{2}}$$

The detection of a horizontal photon does not change the state of the spin: we don't get any information on the spin state or phase, and the phase is not flipped. The detection of a vertical photon flips the phase between the spin states, but still we have no information on the state, only on how it changed. An example of such a

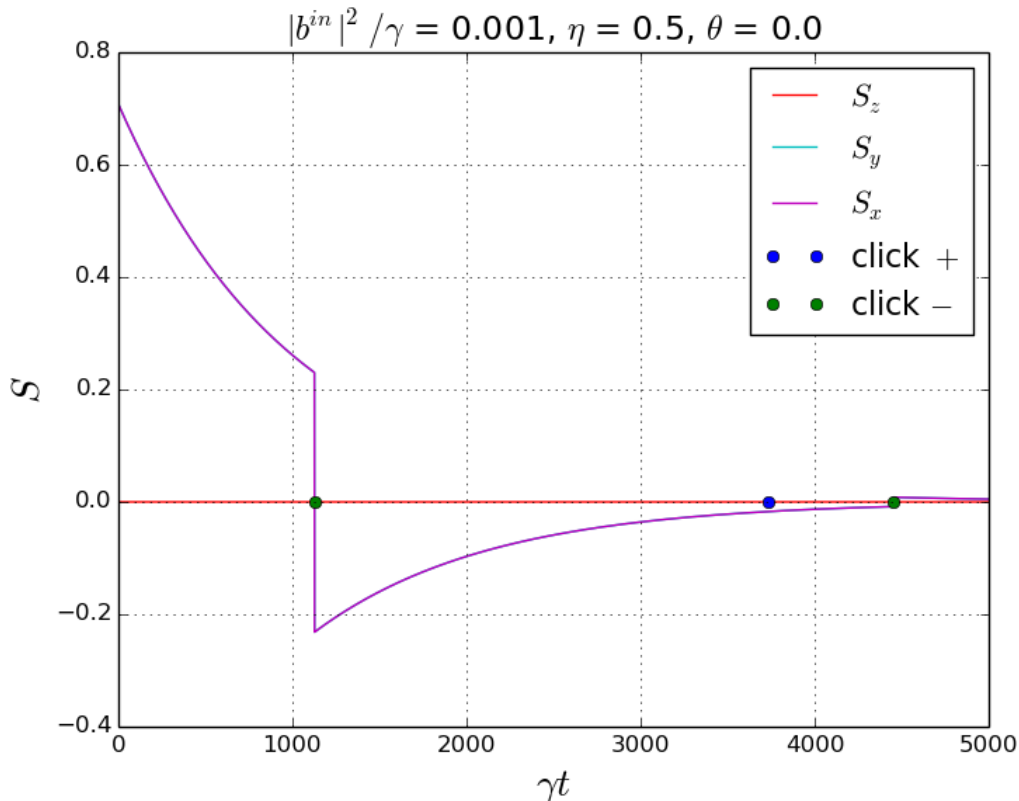


Figure 3.17: Typical trajectory with no magnetic field and rotated measurement bases.  $|b^{in}|^2/\gamma = 10^{-3}$ ,  $\eta = 0.5$ ,  $\phi = \theta = 0$ . Vertical (-) photons switch the phase while the horizontal (+) ones have no impact.

trajectory is shown in Fig. 3.17:  $S_z$  is a difference between the spin-up and spin-down populations,  $S_x$  and  $S_y$  are the real and the imaginary parts of the coherences between the electron spin-up and spin down states  $\rho_{\uparrow\downarrow}$ . The initial state is a coherent superposition  $(|\uparrow\rangle + |\downarrow\rangle)/\sqrt{2}$ , but in the beginning the  $S_x$  quickly decays because of the growth of the trion populations, so it seems that it does not start from 1. Later on it decays because of the undetected photons, and after a vertical photon is detected (time indicated by a green dot), it changes the sign, while after detection of the horizontal one (blue dot), nothing happens. The populations of the spin state, whose difference is plotted in red, do not change at all, as the probability to detect  $h$  and  $v$  polarized photons does not depend on the state of the spin, and one gets no information on the spin state by detection of a photon.

Fig. 3.18 shows trajectories on a Bloch-like sphere that corresponds to different electron spin states, where  $|\pm_{el}\rangle = (|\uparrow\rangle \pm |\downarrow\rangle)/\sqrt{2}$  and  $|\pm_{iel}\rangle = (|\uparrow\rangle \pm i|\downarrow\rangle)/\sqrt{2}$ .

In the case of  $\theta = 0$ ,  $\phi = \pi/2$  (Fig. 3.18a), when the probabilities to detect left and right polarized photon are equal, a photodetection changes not the state of the spin, but only the phase:  $L_+$  rotates the phase by  $\pi/2$  in one direction, and  $L_-$  - in another. Again, no information on the state of the spin is gained: we know how the phase between the spin states may have changed, but both the value of the phase and the populations of the spin states remain unknown.

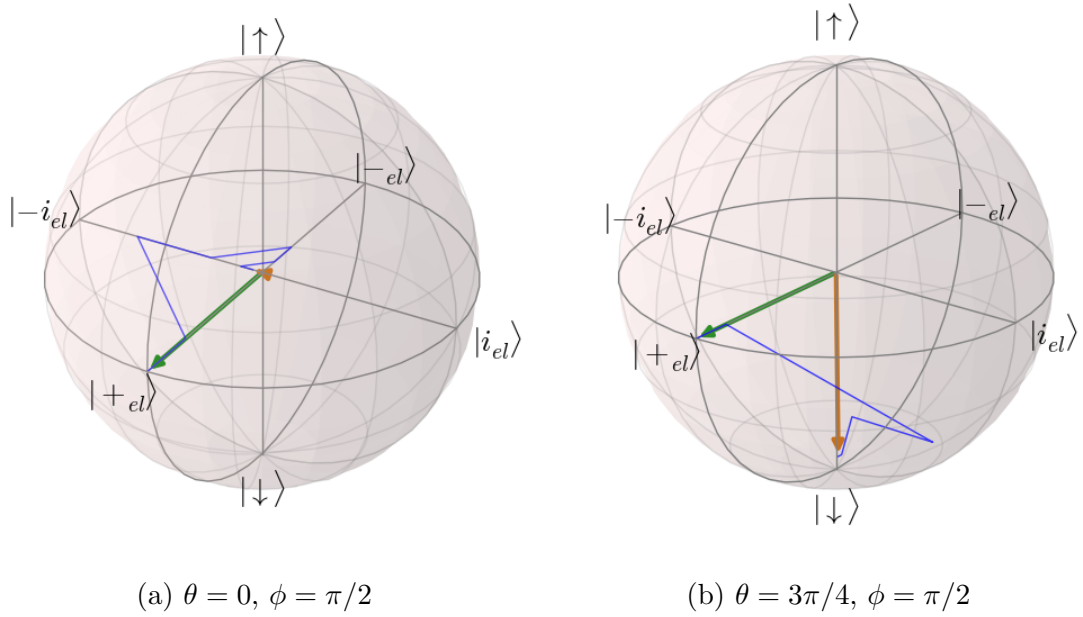


Figure 3.18: Typical trajectories with no magnetic field and rotated measurement bases.  $|b^{in}|^2/\gamma = 10^{-3}$ ,  $\eta = 0.5$ . The green and the yellow arrows show the initial and the final states respectively.

If  $\theta$  is different from  $0, \pi/2$  or  $\pi$ , a photodetection both changes the phase and the state, as in Fig. 3.18b, as some information is retrieved.

### 3.5.3 Partially distinguishable polarization states

Another imperfection in measurements corresponds to  $\eta \neq 0.5$ . As can be seen from Fig. 3.9, in this case the polarization states will not be orthogonal any more, and the detection of a photon in a certain polarization will bring ambiguous information about the spin state [116].

However, if the chosen set of the measurement polarizations includes one of the polarization states that correspond to the  $|\uparrow(\downarrow)\rangle$  state of the spin  $\vec{\varepsilon}_{\uparrow(\downarrow)}$ , the detection of a photon in a polarization, orthogonal to it  $\vec{\varepsilon}_{\uparrow(\downarrow)}^\perp$  will mean that the spin is oriented along the other direction  $|\downarrow(\uparrow)\rangle$ .

As one may recall from Fig. 3.9, in the limit case of  $\eta = 0$ , all the photons, that arrive to detector, come from the mirror, and there is no information about the spin state as well as no back-action. In another limit,  $\eta = 1$ , only vertically polarized photons are detected (if the basis is  $\{h, v\}$ ), and they cause the phase flip.

Several possible trajectories for an intermediate value of  $\eta = 0.75$  are shown in Fig. 3.19. The set of measurement polarizations consists of  $\vec{\varepsilon}_\downarrow$  and  $\vec{\varepsilon}_\downarrow^\perp$ . The polarization that corresponds to spin-up is not orthogonal to  $\vec{\varepsilon}_\downarrow^\perp$ , hence the click in the  $\vec{\varepsilon}_\downarrow$  polarization does not necessarily mean the the spin is down: it could have been the photon, scattered by the spin-up system, that with a non-zero probability went to the branch of the polarizing beam splitter that corresponds to  $\vec{\varepsilon}_\downarrow^\perp$ . However, the second detector measures light in the polarization  $\vec{\varepsilon}_\downarrow^\perp$  that is orthogonal to  $\vec{\varepsilon}_\downarrow$ . Hence, if the spin is down, no photons will be registered there, and if there is a click,

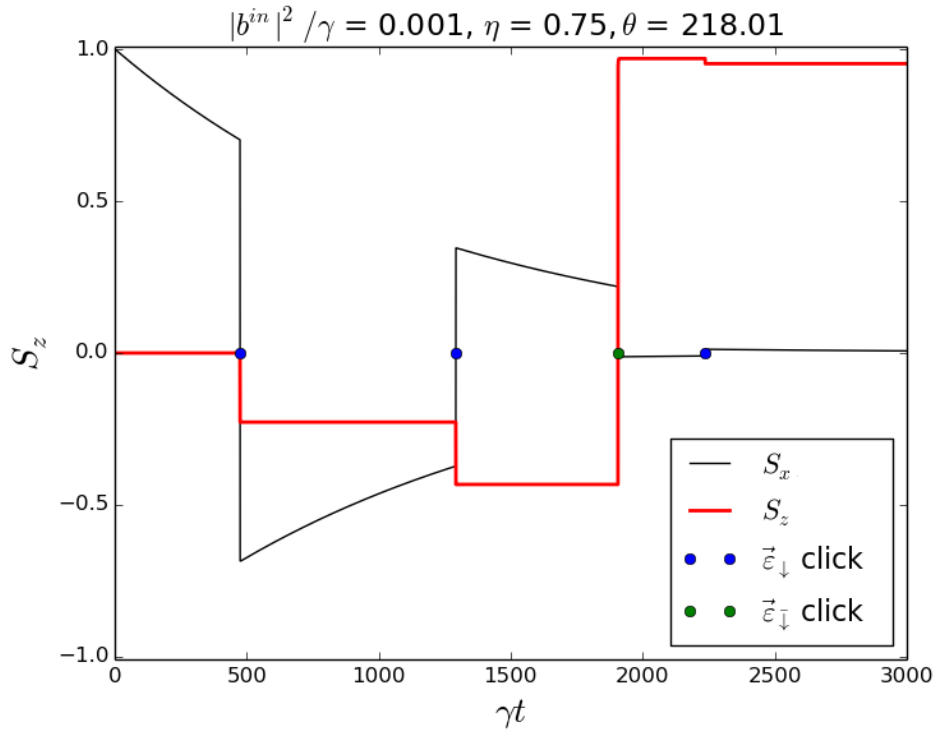


Figure 3.19: Typical trajectories with no magnetic field,  $\eta = 0.75$  and rotated measurement bases, that corresponds to this  $\eta$ .  $|b^{in}|^2/\gamma = 10^{-3}$ . The initial state is  $|+_{el}\rangle$ . The first two clicks are detected in the polarization, that corresponds to the spin-down state. As it is not orthogonal with the one that corresponds to the spin-up, the projection is not complete. The third click is detected in a polarization that is orthogonal to the polarization state, that corresponds to the spin-down, hence the state is projected onto the spin-up state. Note, that after the projection the click in other polarization is still possible.

it means that the photon is not oriented down, so it is in a spin-up state.

Detected polarization	Spin state after the click
$\vec{\epsilon}_{\downarrow}$	superposition of $ \uparrow\rangle$ and $ \downarrow\rangle$
$\vec{\epsilon}_{\uparrow}$	$ \uparrow\rangle$

The first two photons of the trajectory in Fig. 3.19 are detected in the  $\vec{\epsilon}_{\downarrow}$  polarization, hence each of them slightly increases the probability that the spin is indeed in a down state. Then one a photon is detected in the different polarization, and it projects the spin onto the up state. However, it does not prevent the detector to register a photon in a  $\vec{\epsilon}_{\downarrow}$  polarization: the photon, emitted in the polarization that corresponds to the spin-up state is not orthogonal to it, so it may pass in that branch of the PBS.

In this section we considered the possible features of the system that may decrease the information gained from measurement of a single photon. Imperfect detectors will make clicks appear less frequently, but the two spin states still can be distinguished after detection of only one photon. The non-optimal basis makes

also the phase change, and if the polarizations are rotated at  $45^\circ$  with respect to the optimal basis, no measurement is made. If the polarizations, that correspond to the different spin states, are not orthogonal, there still a way to perform a measurement by measuring in one of these polarizations and waiting for a photon in a polarization, orthogonal to it.

### 3.6 Summary

In this chapter we investigated the measurement of a spin state via polarization of the light, scattered on it, and its back-action on the system for a QD doped with an electron in a waveguide with a mirror: the system that can be experimentally realized as a QD weakly coupled to a micropillar cavity with high bottom mirror reflectivity.

In this system the spin-up and spin-down states evolve independently, unless coupled by magnetic field, that forms a good basis for performing a quantum non demolition measurement of the spin state. However, the measurement itself induces a decoherence, that depends on the pump power.

This system can exist in a different regimes, depending on the values of its parameters and the pump power. For the low power the interaction is coherent, hence the measurement-induced dephasing is proportional to the power. This regime is also the most optimal for the measurement of the spin state via reflected light, especially for the system, characterized by laser-system coupling  $\eta = 0.5$ . If the magnetic field is turned on, there is a possibility to freeze the spin precession, if  $\Omega_B \ll \eta|b^{in}|^2$  - it corresponds to Zeno regime. For the high power, the spin measurement is less efficient, than for the low one, as it requires processing of a large number of photons.

The measurement and the back-action were also studied in case of individual realizations of the experiment, in the way that accounts possible losses of the photons. It was shown that for the aforementioned conditions it is enough to detect one photon to measure the spin state, and it can be used to reach Zeno limit, or to prepare the spin in an arbitrary state.



# Chapter 4

## Conclusions and perspectives

The development of quantum technologies requires the ability to construct networks, consisting of stationary qubits, storing information, and flying qubits, transmitting it. A promising candidate to perform as such light-matter interface in an emitter embedded in a unidimensional electromagnetic environment, a 1D atom. Efficient quantum gates can be realized using the cavity quantum electrodynamics to describe the light-matter interaction, predicting and controlling the behaviour of the system.

As formulated by di Vincenzo, an efficient quantum network is required to be able to transmit the quantum state between the stationary and flying qubits. We studied this ability in the Chapter 1, exploring the possibility to control the state of a stationary qubit implemented as a two- or a three-level system in a cavity, with a light pulse of given parameters. Symmetrically, in the same chapter we studied the impact of such an implementation of a 1D atom acting as a stationary qubit on the state of light, scattered on it. This study was continued in the Chapter 2, with the focus on the purity of the scattered light, and its characterization.

Another of the di Vincenzo criteria demands the system to be used as a qubit has such coherence time that exceeds all the other characteristic times. This is fulfilled for systems consisting of a single spin in different media, including the spin of a donor charge in a semiconductor quantum dot, a system that can be modelled as a 1D atom. Thus, the research of the Chapter 3 was dedicated to the study of this system and a readout of its state. The formalism developed in this Chapter allows to suggest a protocol to initialize a single spin in a given state and to monitor its evolution in a continuous manner, by measuring the polarization of the output light field.

The research conducted in the first two chapters opens possibilities towards an implementation of a scalable quantum network composed of 1D atoms. Its implementation requires a study of an interaction between a group of such devices, both theoretical and experimental.

On the theoretical part, the continuation of the work of the Chapter 2 would be a development of a self-consistent model of the emission process, allowing a more complete description of a quantum state of the emitted light. For example, it is interesting to study the impact of the pure dephasing, acting on the emitter, on the purity of the emitted light. Such a study would allow to separate two contributions

into the purity reduction: from the influence of the distinguishability of the photons, and from the incoherent processes affecting the emitter.

The natural continuation of the study of the Chapter 3 would be to reproduce its conclusions experimentally, which is possible with current state of art. The Quantum Non Demolition measurement of the state of the spin with a single photon, as well as the high-fidelity spin-photon entanglement open major perspectives both for the research and for the quantum information processing. Entanglement between a single spin and a single photon represents an important step towards establishing an efficient connection of stationary qubits into a single network.

The next possible step of the theoretic research conducted in the last Chapter is to extend the study on the regime of the pulsed laser excitations, exploring the impact of the pulse characteristics on the measurement efficiency and on the fidelity of the entanglement between the spin and the electromagnetic field in the incident pulse.

Another possible direction is to investigate the potential of a spin-photon interface from the perspective of quantum thermodynamics. An ensemble of quantum trajectories, used in the chapter, can be exploited in thermodynamical framework, where heat and work are defined at a single trajectory level: heat corresponding to the stochastic element in spin dynamics, caused by the interaction with the electro-dynamics environment and the measurement, and work defined through the unitary interaction with the laser drive or the magnetic field. It allows to investigate the fluctuation theorems and the possibility of building quantum information engines, based on the single spin measurement.

# Bibliography

- [1] Max Planck. On an improvement of wien's equation for the spectrum. *Verh. Deut. Phys. Ges*, 2:202–204, 1900.
- [2] Max Planck. On the law of distribution of energy in the normal spectrum. *Annalen der physik*, 4(553):1, 1901.
- [3] Louis De Broglie. La mécanique ondulatoire et la structure atomique de la matière et du rayonnement. *J. Phys. Radium*, 8(5):225–241, 1927.
- [4] Albert Einstein. Zur quantentheorie der strahlung. *Phys. Z.*, 18:121–128, 1917.
- [5] Werner Heisenberg. Über den anschaulichen inhalt der quantentheoretischen kinematik und mechanik. In *Original Scientific Papers Wissenschaftliche Originalarbeiten*, pages 478–504. Springer, 1985.
- [6] Jonathan P Dowling and Gerard J Milburn. Quantum technology: the second quantum revolution. *Philosophical Transactions of the Royal Society of London A: Mathematical, Physical and Engineering Sciences*, 361(1809):1655–1674, 2003.
- [7] John Preskill. Quantum computing and the entanglement frontier. *arXiv preprint arXiv:1203.5813*, 2012.
- [8] I Manin Yu. *Vychislimoe i Nevychislimoe (Computable and Noncomputable)*. Moscow: Sov. Radio, 1980.
- [9] Richard P Feynman. Simulating physics with computers. *International journal of theoretical physics*, 21(6-7):467–488, 1982.
- [10] IM Georgescu, Sahel Ashhab, and Franco Nori. Quantum simulation. *Reviews of Modern Physics*, 86(1):153, 2014.
- [11] Thaddeus D Ladd, Fedor Jelezko, Raymond Laflamme, Yasunobu Nakamura, Christopher Monroe, and Jeremy Lloyd O'Brien. Quantum computers. *Nature*, 464(7285):45, 2010.
- [12] Nicolas Gisin and Rob Thew. Quantum communication. *Nature photonics*, 1(3):165, 2007.

- [13] Charles H Bennett and Gilles Brassard. Quantum cryptography: Public key distribution and coin tossing. *Theor. Comput. Sci.*, 560(P1):7–11, 2014.
- [14] Vittorio Giovannetti, Seth Lloyd, and Lorenzo Maccone. Quantum metrology. *Physical review letters*, 96(1):010401, 2006.
- [15] H. J. Kimble. The quantum internet. *Nature*, 453:1023, 2008.
- [16] David P DiVincenzo et al. The physical implementation of quantum computation. *arXiv preprint quant-ph/0002077*, 2000.
- [17] Nicolai Friis, Oliver Marty, Christine Maier, Cornelius Hempel, Milan Holzäpfel, Petar Jurcevic, Martin B Plenio, Marcus Huber, Christian Roos, Rainer Blatt, et al. Observation of entangled states of a fully controlled 20-qubit system. *Physical Review X*, 8(2):021012, 2018.
- [18] Yuanhao Wang, Ying Li, Zhang-qi Yin, and Bei Zeng. 16-qubit ibm universal quantum computer can be fully entangled. *npj Quantum Information*, 4(46), 2018.
- [19] Chao Chen, Chao-Yang Lu, and Jian-Wei Pan. Multi-photon quantum boson sampling on a semiconductor (conference presentation). In *Quantum Photonic Devices 2018*, volume 10733, page 1073307. International Society for Optics and Photonics, 2018.
- [20] Gershon Kurizki, Patrice Bertet, Yuimaru Kubo, Klaus Mølmer, David Petrosyan, Peter Rabl, and Jörg Schmiedmayer. Quantum technologies with hybrid systems. *Proceedings of the National Academy of Sciences*, page 201419326, 2015.
- [21] QA Turchette, RJ Thompson, and HJ Kimble. One-dimensional atoms. *Applied physics B-lasers and optics*, 60(2-3):S1–S10, 1995.
- [22] Quentin A Turchette, Christina J Hood, Wolfgang Lange, HJKH Mabuchi, and H Jerrey Kimble. Measurement of conditional phase shifts for quantum logic. *Physical Review Letters*, 75(25):4710, 1995.
- [23] Chi Huan Nguyen, Adrian Nugraha Utama, Nick Lewty, Kadir Durak, Gleb Maslennikov, Stanislav Straupe, Matthias Steiner, and Christian Kurtz. Single atoms coupled to a near-concentric cavity. *Physical Review A*, 96(3):031802, 2017.
- [24] Xiao-Liu Chu, Stephan Götzinger, and Vahid Sandoghdar. A single molecule as a high-fidelity photon gun for producing intensity-squeezed light. *Nature Photonics*, 11(1):58, 2017.
- [25] P. Campagne-Ibarcq, S. Jezouin, N. Cottet, P. Six, L. Bretheau, F. Mallet, A. Sarlette, P. Rouchon, and B. Huard. Using spontaneous emission of a qubit as a resource for feedback control. *Phys. Rev. Lett.*, 117:060502, Aug 2016.

- [26] Shingo Kono, Yuta Masuyama, Toyofumi Ishikawa, Yutaka Tabuchi, Rekishu Yamazaki, Koji Usami, Kazuki Koshino, and Yasunobu Nakamura. Nonclassical photon number distribution in a superconducting cavity under a squeezed drive. *Physical review letters*, 119(2):023602, 2017.
- [27] Peter Christian Maurer, Georg Kucsko, Christian Latta, Liang Jiang, Norman Ying Yao, Steven D Bennett, Fernando Pastawski, David Hunger, Nicholas Chisholm, Matthew Markham, et al. Room-temperature quantum bit memory exceeding one second. *Science*, 336(6086):1283–1286, 2012.
- [28] V Giesz, N Somaschi, G Hornecker, T Grange, B Reznichenko, L De Santis, J Demory, C Gomez, I Sagnes, A Lemaître, et al. Coherent manipulation of a solid-state artificial atom with few photons. *Nature communications*, 7:11986, 2016.
- [29] Kevin M Birnbaum, Andreea Boca, Russell Miller, Allen D Boozer, Tracy E Northup, and H Jeff Kimble. Photon blockade in an optical cavity with one trapped atom. *Nature*, 436(7047):87, 2005.
- [30] Luozhou Li, Tim Schröder, Edward H Chen, Michael Walsh, Igal Bayn, Jordan Goldstein, Ophir Gaathon, Matthew E Trusheim, Ming Lu, Jacob Mower, et al. Coherent spin control of a nanocavity-enhanced qubit in diamond. *Nature communications*, 6:6173, 2015.
- [31] O Gazzano, S Michaelis De Vasconcellos, C Arnold, A Nowak, E Galopin, I Sagnes, L Lanco, A Lemaître, and P Senellart. Bright solid-state sources of indistinguishable single photons. *Nature communications*, 4:1425, 2013.
- [32] Andreas Reiserer, Norbert Kalb, Gerhard Rempe, and Stephan Ritter. A quantum gate between a flying optical photon and a single trapped atom. *Nature*, 508(7495):237, 2014.
- [33] Julien Claudon, Joël Bleuse, Nitin Singh Malik, Maela Bazin, Périne Jaffrennou, Niels Gregersen, Christophe Sauvan, Philippe Lalanne, and Jean-Michel Gérard. A highly efficient single-photon source based on a quantum dot in a photonic nanowire. *Nature Photonics*, 4(3):174, 2010.
- [34] Marta Arcari, Immo Söllner, Alisa Javadi, S Lindskov Hansen, Sahand Mahmoodian, Jin Liu, Henri Thyrrestrup, Eun Hye Lee, Jin Dong Song, Søren Stobbe, et al. Near-unity coupling efficiency of a quantum emitter to a photonic crystal waveguide. *Physical review letters*, 113(9):093603, 2014.
- [35] Itay Shomroni, Serge Rosenblum, Yulia Lovsky, Orel Bechler, Gabriel Guedelman, and Barak Dayan. All-optical routing of single photons by a one-atom switch controlled by a single photon. *Science*, 345(6199):903–906, 2014.
- [36] LD Landau and EM Lifshiz. *Teoreticheskaya fizika. Tom 3, kvantovaya mekhanika*. Fizmatlit, 2002.

- [37] A Imamoglu, David D Awschalom, Guido Burkard, David P DiVincenzo, Daniel Loss, M Sherwin, A Small, et al. Quantum information processing using quantum dot spins and cavity qed. *Physical review letters*, 83(20):4204, 1999.
- [38] A Dousse, L Lanco, J Suffczyński, E Semenova, A Miard, A Lemaître, I Sagnes, C Roblin, Jacqueline Bloch, and P Senellart. Controlled light-matter coupling for a single quantum dot embedded in a pillar microcavity using far-field optical lithography. *Physical review letters*, 101(26):267404, 2008.
- [39] Jeremy L O'Brien, Geoffrey J Pryde, Andrew G White, Timothy C Ralph, and David Branning. Demonstration of an all-optical quantum controlled-not gate. *Nature*, 426(6964):264, 2003.
- [40] Lorenzo De Santis, Carlos Antón, Bogdan Reznichenko, Niccolo Somaschi, Guillaume Coppola, Jean Senellart, Carmen Gómez, Aristide Lemaître, Isabelle Sagnes, Andrew G White, et al. A solid-state single-photon filter. *Nature nanotechnology*, 12(7):663, 2017.
- [41] Emanuel Knill, Raymond Laflamme, and Gerald J Milburn. A scheme for efficient quantum computation with linear optics. *nature*, 409(6816):46, 2001.
- [42] Darrick E Chang, Vladan Vuletić, and Mikhail D Lukin. Quantum nonlinear optics - photon by photon. *Nature Photonics*, 8(9):685, 2014.
- [43] HA Nguyen, T Grange, B Reznichenko, I Yeo, P-L De Assis, D Tumanov, F Fratini, NS Malik, E Dupuy, Niels Gregersen, et al. Giant nonlinear interaction between two optical beams via a quantum dot embedded in a photonic wire. *Physical Review B*, 97(20):201106, 2018.
- [44] JD Franson, BC Jacobs, and TB Pittman. Quantum computing using single photons and the zeno effect. *Physical Review A*, 70(6):062302, 2004.
- [45] Kae Nemoto and William J Munro. Nearly deterministic linear optical controlled-not gate. *Physical review letters*, 93(25):250502, 2004.
- [46] Holger P Specht, Christian Nölleke, Andreas Reiserer, Manuel Uphoff, Eden Figueroa, Stephan Ritter, and Gerhard Rempe. A single-atom quantum memory. *Nature*, 473(7346):190, 2011.
- [47] Alexander I Lvovsky, Barry C Sanders, and Wolfgang Tittel. Optical quantum memory. *Nature photonics*, 3(12):706, 2009.
- [48] A Stute, B Casabone, B Brandstätter, K Friebe, TE Northup, and R Blatt. Quantum-state transfer from an ion to a photon. *Nature photonics*, 7(3):219, 2013.

- [49] Ranojoy Bose, Deepak Sridharan, Hyochul Kim, Glenn S Solomon, and Edo Waks. Low-photon-number optical switching with a single quantum dot coupled to a photonic crystal cavity. *Physical review letters*, 108(22):227402, 2012.
- [50] Dirk Englund, Arka Majumdar, Michal Bajcsy, Andrei Faraon, Pierre Petroff, and Jelena Vučković. Ultrafast photon-photon interaction in a strongly coupled quantum dot-cavity system. *Physical review letters*, 108(9):093604, 2012.
- [51] Lucio Robledo, Hannes Bernien, Ilse Van Weperen, and Ronald Hanson. Control and coherence of the optical transition of single nitrogen vacancy centers in diamond. *Physical review letters*, 105(17):177403, 2010.
- [52] Syed Abdullah Aljunid, Gleb Maslennikov, Yimin Wang, Hoang Lan Dao, Valerio Scarani, and Christian Kurtsiefer. Excitation of a single atom with exponentially rising light pulses. *Physical review letters*, 111(10):103001, 2013.
- [53] E. M. Purcell. Spontaneous emission probabilities at radio frequencies. *Physical review*, 62(11-12):674, 1946.
- [54] Daniel Kleppner. Inhibited spontaneous emission. *Physical Review Letters*, 47(4):233, 1981.
- [55] Ph Goy, JM Raimond, M Gross, and S Haroche. Observation of cavity-enhanced single-atom spontaneous emission. *Physical review letters*, 50(24):1903, 1983.
- [56] Randall G Hulet, Eric S Hilfer, and Daniel Kleppner. Inhibited spontaneous emission by a rydberg atom. *Physical review letters*, 55(20):2137, 1985.
- [57] S. Haroche and J.-M. Raimond. *Exploring the Quantum: Atoms, Cavities and Photons*. Oxford University Press, 2006.
- [58] Gardiner C.W. *Quantum noise*. Springer, 1991.
- [59] Howard J Carmichael. *Statistical methods in quantum optics 2: Non-classical fields*. Springer Science & Business Media, 2009.
- [60] Justin Demory. *Initialisation de spin et rotation de polarisation dans une boîte quantique en microcavité*. PhD thesis, Paris Saclay, 2016.
- [61] Alexia Auffèves, Dario Gerace, J-M Gérard, M França Santos, LC Andreani, and J-P Poizat. Controlling the dynamics of a coupled atom-cavity system by pure dephasing. *Physical Review B*, 81(24):245419, 2010.
- [62] Alexia Auffèves-Garnier, Christoph Simon, Jean-Michel Gérard, and Jean-Philippe Poizat. Giant optical nonlinearity induced by a single two-level system interacting with a cavity in the purcell regime. *Physical Review A*, 75(5):053823, 2007.

- [63] Alexey I Ekimov, Al L Efros, and Alexei A Onushchenko. Quantum size effect in semiconductor microcrystals. *Solid State Communications*, 56(11):921–924, 1985.
- [64] H Kamada, H Gotoh, J Temmyo, T Takagahara, and H Ando. Exciton rabi oscillation in a single quantum dot. *Physical Review Letters*, 87(24):246401, 2001.
- [65] Léonard Monniello, Catherine Tonin, Richard Hostein, Aristide Lemaitre, Anthony Martinez, Valia Voliotis, and Roger Grousson. Excitation-induced dephasing in a resonantly driven inas/gaas quantum dot. *Physical Review Letters*, 111(2):026403, 2013.
- [66] Catherine Tonin, Richard Hostein, Valia Voliotis, Roger Grousson, Aristide Lemaitre, and Anthony Martinez. Polarization properties of excitonic qubits in single self-assembled quantum dots. *Physical Review B*, 85(15):155303, 2012.
- [67] Lorenzo De Santis. *Single photon generation and manipulation with semiconductor quantum dot devices*. PhD thesis, Paris Saclay, 2018.
- [68] JR Johansson, PD Nation, and Franco Nori. Qutip: An open-source python framework for the dynamics of open quantum systems. *Computer Physics Communications*, 183(8):1760–1772, 2012.
- [69] AK Nowak, SL Portalupi, V Giesz, O Gazzano, C Dal Savio, P-F Braun, K Karrai, C Arnold, L Lanco, I Sagnes, et al. Deterministic and electrically tunable bright single-photon source. *Nature communications*, 5:3240, 2014.
- [70] Yimin Wang, Jiří Minář, Lana Sheridan, and Valerio Scarani. Efficient excitation of a two-level atom by a single photon in a propagating mode. *Physical Review A*, 83(6):063842, 2011.
- [71] Klaus M Gheri, Klaus Ellinger, Thomas Pellizzari, and Peter Zoller. Photon-wavepackets as flying quantum bits. *Fortschritte der Physik: Progress of Physics*, 46(4-5):401–415, 1998.
- [72] Hemlin Swaran Rag and Julio Gea-Banacloche. Two-level-atom excitation probability for single-and n-photon wave packets. *Physical Review A*, 96(3):033817, 2017.
- [73] Darrick E Chang, Anders S Sørensen, Eugene A Demler, and Mikhail D Lukin. A single-photon transistor using nanoscale surface plasmons. *Nature Physics*, 3(11):807, 2007.
- [74] R Bourgain, J Pellegrino, S Jennewein, Yvan RP Sortais, and Antoine Browaeys. Direct measurement of the wigner time delay for the scattering of light by a single atom. *Optics letters*, 38(11):1963–1965, 2013.



- [75] Elizabeth A Goldschmidt, Fabrizio Piacentini, Ivano Ruo Berchera, Sergey V Polyakov, Silke Peters, Stefan Kück, Giorgio Brida, Ivo P Degiovanni, Alan Migdall, and Marco Genovese. Mode reconstruction of a light field by multiphoton statistics. *Physical Review A*, 88(1):013822, 2013.
- [76] Serge Rosenblum, Scott Parkins, and Barak Dayan. Photon routing in cavity qed: Beyond the fundamental limit of photon blockade. *Physical Review A*, 84(3):033854, 2011.
- [77] CY Hu, WJ Munro, and JG Rarity. Deterministic photon entangler using a charged quantum dot inside a microcavity. *Physical Review B*, 78(12):125318, 2008.
- [78] Cristian Bonato, Florian Haupt, Sumant SR Oemrawsingh, Jan Gudat, Dapeng Ding, Martin P van Exter, and Dirk Bouwmeester. Cnot and bell-state analysis in the weak-coupling cavity qed regime. *Physical review letters*, 104(16):160503, 2010.
- [79] Valerio Scarani, Helle Bechmann-Pasquinucci, Nicolas J Cerf, Miloslav Dušek, Norbert Lütkenhaus, and Momtchil Peev. The security of practical quantum key distribution. *Reviews of modern physics*, 81(3):1301, 2009.
- [80] Darius Bunandar, Anthony Lentine, Catherine Lee, Hong Cai, Christopher M Long, Nicholas Boynton, Nicholas Martinez, Christopher DeRose, Changchen Chen, Matthew Grein, et al. Metropolitan quantum key distribution with silicon photonics. *Physical Review X*, 8(2):021009, 2018.
- [81] Raj B Patel, Joseph Ho, Franck Ferreyrol, Timothy C Ralph, and Geoff J Pryde. A quantum fredkin gate. *Science advances*, 2(3):e1501531, 2016.
- [82] Jeremy L O’Brien. Optical quantum computing. *Science*, 318(5856):1567–1570, 2007.
- [83] Erwan Bimbard, Nitin Jain, Andrew MacRae, and AI Lvovsky. Quantum-optical state engineering up to the two-photon level. *Nature Photonics*, 4(4):243, 2010.
- [84] Tim J Bartley, Gaia Donati, Justin B Spring, Xian-Min Jin, Marco Barbieri, Animesh Datta, Brian J Smith, and Ian A Walmsley. Multiphoton state engineering by heralded interference between single photons and coherent states. *Physical Review A*, 86(4):043820, 2012.
- [85] Max Hofheinz, H Wang, Markus Ansmann, Radoslaw C Bialczak, Erik Lucero, Matthew Neeley, AD O’connell, Daniel Sank, J Wenner, John M Martinis, et al. Synthesizing arbitrary quantum states in a superconducting resonator. *Nature*, 459(7246):546, 2009.

- [86] Kevin A Fischer, Lukas Hanschke, Jakob Wierzbowski, Tobias Simmet, Constantin Dory, Jonathan J Finley, Jelena Vučković, and Kai Müller. Signatures of two-photon pulses from a quantum two-level system. *Nature Physics*, 13(7):649, 2017.
- [87] Manuel Gschrey, Alexander Thoma, Peter Schnauber, Mark Seifried, Ronny Schmidt, Benjamin Wohlfeil, Luzy Krüger, J-H Schulze, Tobias Heindel, Sven Burger, et al. Highly indistinguishable photons from deterministic quantum-dot microlenses utilizing three-dimensional in situ electron-beam lithography. *Nature communications*, 6:7662, 2015.
- [88] Yu-Jia Wei, Yu-Ming He, Ming-Cheng Chen, Yi-Nan Hu, Yu He, Dian Wu, Christian Schneider, Martin Kamp, Sven Hofling, Chao-Yang Lu, et al. Deterministic and robust generation of single photons from a single quantum dot with 99.5% indistinguishability using adiabatic rapid passage. *Nano letters*, 14(11):6515–6519, 2014.
- [89] Niccolo Somaschi, Valerian Giesz, Lorenzo De Santis, JC Loredo, Marcelo P Almeida, Gaston Hornecker, Simone Luca Portalupi, Thomas Grange, Carlos Antón, Justin Demory, et al. Near-optimal single-photon sources in the solid state. *Nature Photonics*, 10(5):340, 2016.
- [90] Chong-Ki Hong, Zhe-Yu Ou, and Leonard Mandel. Measurement of subpicosecond time intervals between two photons by interference. *Physical review letters*, 59(18):2044, 1987.
- [91] Léonard Monniello, Antoine Reigue, Richard Hostein, Aristide Lemaitre, Anthony Martinez, Roger Grousseau, and Valia Voliotis. Indistinguishable single photons generated by a quantum dot under resonant excitation observable without postselection. *Physical Review B*, 90(4):041303, 2014.
- [92] V Giesz, SL Portalupi, T Grange, C Antón, L De Santis, J Demory, N Somaschi, I Sagnes, A Lemaître, L Lanco, et al. Cavity-enhanced two-photon interference using remote quantum dot sources. *Physical Review B*, 92(16):161302, 2015.
- [93] Charles Santori, David Fattal, Jelena Vučković, Glenn S Solomon, and Yoshihisa Yamamoto. Indistinguishable photons from a single-photon device. *Nature*, 419(6907):594, 2002.
- [94] Ludwig Zehnder. *Ein neuer interferenzrefraktor*. Springer, 1891.
- [95] Ludwig Mach. Ueber einen interferenzrefraktor. *Zeitschrift für Instrumentenkunde*, 12(3):89, 1892.
- [96] L De Santis, G Coppola, C Antón, N Somaschi, C Gómez, A Lemaître, I Sagnes, L Lanco, JC Loredo, O Krebs, et al. Overcomplete quantum tomography of a path-entangled two-photon state. *arXiv preprint arXiv:1707.07837*, 2017.

- [97] ZY Ou. Temporal distinguishability of an n-photon state and its characterization by quantum interference. *Physical Review A*, 74(6):063808, 2006.
- [98] C Lü, JL Cheng, and MW Wu. Hole spin relaxation in semiconductor quantum dots. *Physical Review B*, 71(7):075308, 2005.
- [99] S Laurent, B Eble, O Krebs, A Lemaître, B Urbaszek, X Marie, T Amand, and P Voisin. Electrical control of hole spin relaxation in charge tunable inas/gaas quantum dots. *Physical review letters*, 94(14):147401, 2005.
- [100] Miro Kroutvar, Yann Ducommun, Dominik Heiss, Max Bichler, Dieter Schuh, Gerhard Abstreiter, and Jonathan J Finley. Optically programmable electron spin memory using semiconductor quantum dots. *Nature*, 432(7013):81, 2004.
- [101] M Steger, K Saeedi, MLW Thewalt, JJJ Morton, H Riemann, NV Abrosimov, P Becker, and H-J Pohl. Quantum information storage for over 180 s using donor spins in a 28si semiconductor vacuum. *Science*, 336(6086):1280–1283, 2012.
- [102] Alban Lafuente-Sampietro, Hervé Boukari, and Lucien Besombes. Resonant photoluminescence and dynamics of a hybrid mn hole spin in a positively charged magnetic quantum dot. *Physical Review B*, 95(24):245308, 2017.
- [103] Rajib Rahman, Cameron J Wellard, Forrest R Bradbury, Marta Prada, Jared H Cole, Gerhard Klimeck, and Lloyd CL Hollenberg. High precision quantum control of single donor spins in silicon. *Physical review letters*, 99(3):036403, 2007.
- [104] David Press, Thaddeus D Ladd, Bingyang Zhang, and Yoshihisa Yamamoto. Complete quantum control of a single quantum dot spin using ultrafast optical pulses. *Nature*, 456(7219):218, 2008.
- [105] J Berezovsky, MH Mikkelsen, NG Stoltz, LA Coldren, and DD Awschalom. Picosecond coherent optical manipulation of a single electron spin in a quantum dot. *Science*, 320(5874):349–352, 2008.
- [106] Xiaodong Xu, Bo Sun, Paul R Berman, Duncan G Steel, Allan S Bracker, Dan Gammon, and LJ Sham. Coherent population trapping of an electron spin in a single negatively charged quantum dot. *Nature Physics*, 4(9):692, 2008.
- [107] Xiao Mi, Mónica Benito, Stefan Putz, David M Zajac, Jacob M Taylor, Guido Burkard, and Jason R Petta. A coherent spin–photon interface in silicon. *Nature*, 555(7698):599, 2018.
- [108] Aymeric Delteil, Zhe Sun, Stefan Fält, and Atac Imamoglu. Realization of a cascaded quantum system: heralded absorption of a single photon qubit by a single-electron charged quantum dot. *Physical review letters*, 118(17):177401, 2017.

- [109] Cyril Elouard. Thermodynamics of quantum open systems: Applications in quantum optics and optomechanics. *arXiv preprint arXiv:1709.02744*, 2017.
- [110] Max Born. Quantenmechanik der stoßvorgänge. *Zeitschrift für Physik*, 38(11-12):803–827, 1926.
- [111] Howard M Wiseman and Gerard J Milburn. *Quantum measurement and control*. Cambridge university press, 2009.
- [112] Philippe Grangier, Juan Ariel Levenson, and Jean-Philippe Poizat. Quantum non-demolition measurements in optics. *Nature*, 396(6711):537, 1998.
- [113] J Berezovsky, MH Mikkelsen, O Gywat, NG Stoltz, LA Coldren, and DD Awschalom. Nondestructive optical measurements of a single electron spin in a quantum dot. *Science*, 314(5807):1916–1920, 2006.
- [114] Mete Atatüre, Jan Dreiser, Antonio Badolato, and Atac Imamoglu. Observation of faraday rotation from a single confined spin. *Nature Physics*, 3(2):101, 2007.
- [115] MH Mikkelsen, J Berezovsky, NG Stoltz, LA Coldren, and DD Awschalom. Optically detected coherent spin dynamics of a single electron in a quantum dot. *Nature Physics*, 3(11):770, 2007.
- [116] Christophe Arnold, Justin Demory, Vivien Loo, Aristide Lemaître, Isabelle Sagnes, Mikhail Glazov, Olivier Krebs, Paul Voisin, Pascale Senellart, and Loïc Lanco. Macroscopic rotation of photon polarization induced by a single spin. *Nat Commun*, 6:6236, 02 2015.
- [117] Petros Androvitsaneas, Andrew B Young, Chritian Schneider, Sebastian Maier, Martin Kamp, Sven Höfling, Sebastian Knauer, Edmund Harbord, Cheng-Yong Hu, John G Rarity, et al. Charged quantum dot micropillar system for deterministic light-matter interactions. *Physical Review B*, 93(24):241409, 2016.
- [118] Petros Androvitsaneas, Andrew Young, Joseph Lennon, Christian Schneider, Sebastian Maier, Janna Hinchliff, George Atkinson, Edmund Harbord, Martin Kamp, Sven Hoefling, et al. Efficient deterministic giant photon phase shift from a single charged quantum dot. In *CLEO: QELS\_Fundamental Science*, pages FTu4E–4. Optical Society of America, 2017.
- [119] A Greilich, S Spatzek, IA Yugova, IA Akimov, DR Yakovlev, Al L Efros, D Reuter, AD Wieck, and M Bayer. Collective single-mode precession of electron spins in an ensemble of singly charged (in, ga) as/gaas quantum dots. *Physical Review B*, 79(20):201305, 2009.
- [120] C Emary, Xiaodong Xu, DG Steel, S Saikin, and LJ Sham. Fast initialization of the spin state of an electron in a quantum dot in the voigt configuration. *Physical review letters*, 98(4):047401, 2007.

- 
- [121] X Marie, T Amand, P Le Jeune, M Paillard, P Renucci, LE Golub, VD Dymnikov, and EL Ivchenko. Hole spin quantum beats in quantum-well structures. *Physical Review B*, 60(8):5811, 1999.
- [122] C Antón, CA Kessler, P Hilaire, J Demory, C Gómez, A Lemaître, I Sagnes, ND Lanzillotti-Kimura, O Krebs, N Somaschi, et al. Tomography of optical polarization rotation induced by a quantum dot-cavity device. *arXiv preprint arXiv:1703.04014*, 2017.
- [123] DS Smirnov, B Reznichenko, A Auffèves, and L Lanco. Measurement back action and spin noise spectroscopy in a charged cavity qed device in the strong coupling regime. *Physical Review B*, 96(16):165308, 2017.
- [124] Rodney Loudon. *The quantum theory of light*. OUP New York, 1983.